Micro-plasticity characterization of martensite, ferrite, and dual-phase steel

Chaowei Du

Micro-plasticity characterization of martensite, ferrite, and dual-phase steel

PROEFSCHRIFT

ter verkrijging van de graad van doctor aan de
Technische Universiteit Eindhoven, op gezag van de
rector magnificus prof.dr.ir. F.P.T. Baaijens, voor een
commissie aangewezen door het College voor
Promoties, in het openbaar te verdedigen
op maandag 28 november 2016 om 16:00 uur

door

Chaowei Du

geboren te Sichuan, China

Dit proefschrift is goedgekeurd door de promotoren en de samenstelling van de promotiecommissie is als volgt:

voorzitter:	prof.dr. L.P.H de Goey
promotor:	prof.dr.ir. M.G.D. Geers
copromotor:	dr.ir. J.M.P. Hoefnagels
leden:	prof.dr. P.M. Koenraad
	prof.dr. R. Petrov (Universiteit Gent)
	dr. C. Pinna, (University of Sheffield)
	PD dr.-ing S. Zaefferer (MPIE Düsseldorf)
adviseur:	dr.ir. C.H.L.J. ten Horn (Tata steel)

Het onderzoek of ontwerp dat in dit proefschrift wordt beschreven is uitgevoerd in overeenstemming met de TU/e Gedragscode Wetenschapsbeoefening.

Contents

Summary

Advanced high strength steels (AHSS) and dual phase (DP) steels in particular are increasingly employed in the automotive industry driven by the demanding criteria for carbon emission and vehicle safety. AHSS steels are mostly multiphase metals with complex microstructures, for which, detailed insight in the micro-mechanics is fundamental for the understanding of its behavior. The aim of this thesis is to unravel the governing mechanisms of micro-plasticity in the two most important phases of AHSS, ferrite and lath martensite, as well as their interaction and mutual relation in terms of damage initiation.

First, an automated approach was developed to identify the average phase distribution around damage sites. It is based on (deliberately) overexposed backscattered electron images that sharply mark the damage locations and simultaneously-recorded secondary electron images used to identify the material phases. It was demonstrated that this approach is applicable to a wide variety of multi-phase materials, enabling new insights in damage evolution processes. Application to DP steel revealed that a single topological feature is most sensitive to damage: regions surrounded by hard martensite islands in the loading direction and by soft ferrite on opposing sides.

Next, a novel methodology was developed to enable highly precise nano-force tensile testing on (single) constituents for (multiphase) metals. Key aspects include (i) selection of the locations from which to extract the specimens, based on detailed microstructural and crystallographic characterization, (ii) fabrication and easy handling of the micron-sized tensile specimens, (iii) precise specimen alignment and loading under well-controlled boundary conditions, and (iv) nano-scale force and displacement resolution combined with in-situ microscopic slip trace analysis. Examples have demonstrated how the rich and complete microscopic and mechanical data can unravel complex micro-mechanics.

The micro-tensile test setup was next applied to an interstitial free steel with large grains. For each grain, multiple micro-specimens were extracted and tested, which revealed reproducible crystallographic slips. Both {110}<111> and {112}<111> slip families exhibit equal activity, whereby the slip system(s) with the highest Schmid factor(s) always activate(s) first. The {123}<111> slip system is found to be not active. A similar critical resolved shear stress at room temperature was determined for both active slip systems, i.e. $CRSS_{\{110\}}=(1.0\pm0.1)CRSS_{\{112\}}$. All remaining slip traces could be identified as cross-slip and pencil-glide, therefore, non-Schmid effects were not needed to explain any of the observations.

The crystallography and the alloying elements distribution of lath martensite in DP steel were studied next. The laths in martensite islands in DP steel closely follow the Kurdjumov-Sachs orientation relationship with the prior austenite phase. The islands typically consist of a main packet and minor variants from the same prior austenite grain. This is distinct from fully martensitic (FM) steels, which usually contain all 24 K-S variants. The martensite bands around the center of the thickness of the rolled sheet are composed of continuous domains, most of which also contain a main packet with minor variants from the same prior austenite grain. The

phase transformation sequence causes larger early-formed laths with low dislocation density, and late-formed small laths with high dislocation density. In commercial DP steels, lath martensite undergoes strong carbon partitioning at the lath boundaries and dislocation cores during the coating process (at 450 °C for 300 s). The distribution of substitutional elements remains homogenous, and the effect of auto-tempering is limited.

The micro-plasticity of lath martensite was then studied by uni-axial tensile tests of micro-specimens with large substructures and straight substructure boundaries for different boundaries configurations from FM steels. Lath martensite only exhibits crystallographic slip from {110}<111> systems which comply with Schmid's law. For specimens with boundaries approximately parallel to the loading direction, the deformation is governed by crystallographic slip and a Hall-Petch like strengthening effect was found for both sub-block and block boundaries, the latter being slightly more effective. When substructure boundaries are tilted with respect to the loading, a different deformation mechanism, i.e. boundary sliding, becomes active, which mitigates the plasticity in lath martensite. All substructure (block/sub-block/lath) boundaries show the potential for sliding. The difference between the maximum Schmid factors of the slip systems in boundary planes and the slip systems which do not lie in the boundary planes determines the dominant one out of these two mechanisms. As a results, the two mechanisms are in close competition to carry the overall plasticity of lath martensite. Micro-tensile testing on DP specimens also revealed boundary sliding, explaining reports of high local plasticity in martensite in the literature. Therefore, it may be concluded that boundary sliding is an important plasticity mechanism in bulk FM steels, DP steels and AHSS in general.

Chapter 1. Introduction

1.1 Motivation

Transportation contributed to 31% of total CO_2 emissions in the US [1] and 23.2% in the EU [2] in the year 2014, which makes it one of the main sources of CO_2 emissions caused by human activity. Analysis suggests that a 10% reduction in vehicle weight leads to an 8% reduction of CO_2 emissions [3]. Driven by global emission regulations to reduce the CO_2 emissions, the automotive industry has been applying lighter materials in the production of automobile components. In particular, advanced high strength steels (AHSS) have been introduced in the production of vehicles to reduce their body weight without compromising vehicle safety [4], as indicated in Fig.1.1. The AHSS family includes single phase steels such as martensitic (MS) steels, hot-formed (HF) steels and multiphase steels such as dual phase (DP) steels, complex phase (CP)steels, ferritic-bainitic steels, transformation-induced plasticity (TRIP) steels, and Twinning-Induced Plasticity (TWIP) steels. As shown in Fig. 1.1, all these AHSS grades find their applications in different components of the vehicle body structure.
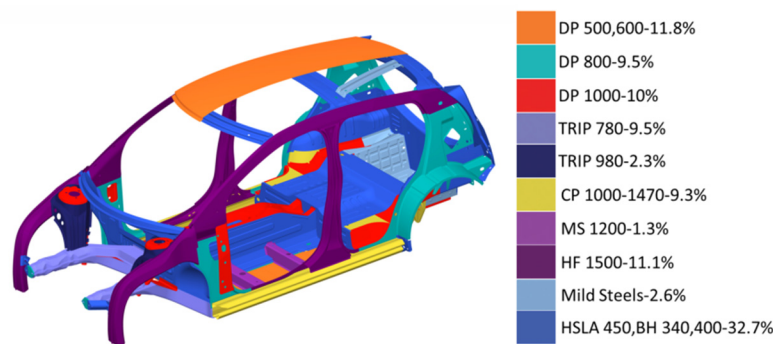
Figure 1.1. A battery electric vehicle (BEV) body structure in the FutureSteelVehicle (FSV) plan of WorldAutoSteel, with the applied steels marked in colors [5]. More than 60wt% of the body structure is made of AHSS.

These AHSS steels mostly have conflicting mechanical properties, e.g. strength versus ductility, where typical components require large deformation during the production that need to be strong during service. Traditionally, it is difficult to obtain this combination of properties with single-phase steels. Figure. 1.2 gives an overview of formability versus strength of traditional steels in comparison with AHSS. DP steel is currently the mostly used AHSS grade as shown in Fig. 1.1. The two components of DP steels, ferrite and lath martensite, are also constituents of most AHSS grades. For instance, lath martensite is present in almost all AHSS grades, including the third generation that is currently under development, as indicated by the red frames in Fig. 1.2.

However, many issues of AHSS require further research, such as chemical-related problems: chemical segregation [6,7], microstructural morphology heterogeneity [8], weldability [9]; and mechanics-related problems such as spring-back effect [10,11] and strain heterogeneity [12].

In addition, due to the complexity of AHSS, the well-established traditional relationships between the material microstructure and properties are not valid [13-17]. Moreover, the understanding of the individual phases of AHSS is far from complete, which is indispensable to solve the above-mentioned mechanics-related problems and to establish predictive relationship between the microstructure and mechanical properties of AHSS.
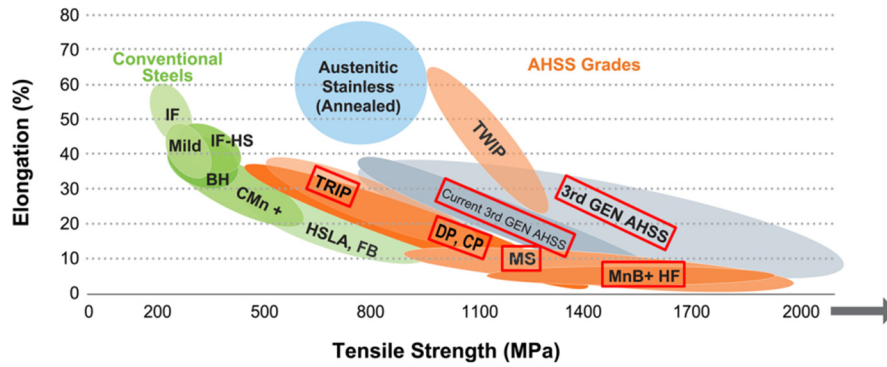
Figure 1.2. An overview of the strength and formability of AHSS and traditional steels. The steels marked with red frames contain lath martensite [5].

Beside the failure of fully martensitic (FM) steels, most failure events in multiphase AHSS are also related to local damage events in and around the lath martensite islands. For example, the failures of DP steels are grouped into three mechanisms based on the positions of the fracture: martensite fracture [18-22], interface decohesion [18-22] and ferrite fracture [21]. Among these three mechanisms, the former two are most frequent and both related to lath martensite, probably due to the stress concentration around it and its lower ductility compared to ferrite [23, 24]. An in-depth study of the micro-plasticity of lath martensite is therefore a necessity.

Lath martensite has a complex hierarchical microstructure, as shown in Fig. 1.3, which makes the analysis of its mechanical behavior a real challenge. As a result of the diffusionless martensitic phase transformation, a prior austenite transforms into a large number of martensite laths which have a well-defined orientation relationship (OR) with the parent austenite phase. For the Kurdjumov-Sachs OR ($\{111\}_\gamma//\{110\}_\alpha$, $<1\text{-}10>_\gamma//<1\text{-}11>_\alpha$), a prior austenite grain is grouped into four packets, laths in each of which share the same habit plane in the austenite-to-martensite phase transformation. Each packet is then subdivided into three blocks, each sharing a different dense-packed crystallographic direction that is parallel to one of the densely packed directions of the parent austenite in the same habit plane. Each block is composed of two sub-blocks that share the same Bain axis, which is the compression direction of prior austenite in the phenomenological theory of martensite transformation. Finally, sub-blocks are formed by parallel laths with close crystallographic orientations (misorientation of 2-5°) [25-27]. This complex microstructure leads to a large number of sub-structure boundaries and the interaction of dislocations with these boundaries makes the mechanical behavior of lath martensite more difficult than other simple steel phases such as ferrite or austenite.
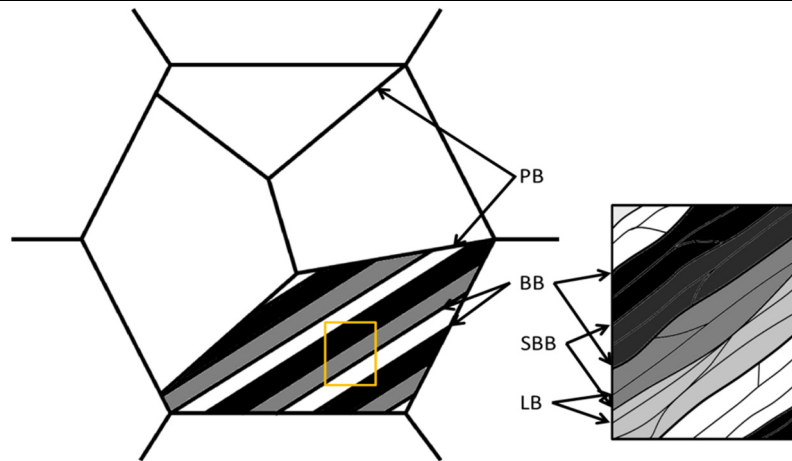
Figure 1.3. Schematic drawing of the hierarchical microstructures of lath martensite transformed from a prior austenite grain together with a zoom-in of the orange frame. The substructure boundaries are marked: packet boundaries (PB) block boundaries (BB) and sub-block boundaries (SBB) and lath boundaries (LB) [25-27].

Lath martensite is strong. When it is the single phase of a steel, lath martensite is among the strongest steels. As one of the phases in a multiphase steel, lath martensite is normally the phase that provides the strength to the steel. The research on the strengthening mechanism of lath martensite has revealed some causes of its high strength: (1) forest dislocation hardening [28,29], (2) solid solution hardening by alloying elements [30], (3) dispersion strengthening, e.g., by carbides [31], and most importantly (iv) substructure boundary strengthening [30-35]. The applied experimental methods in literature are generally macroscale mechanical tests, in which information on the micro-mechanisms was attained indirectly, e.g. by fitting macroscopic mechanical properties to the size of microstructural features [28-31]. Recently, micro-mechanical test methods have become available due to the improvement of micro-specimen fabrication methods and micro-testing techniques. These tests allow investigation of a single substructure unit such as single packets and blocks [32-35]. However, most of the micro-mechanical tests so far were conducted under poorly defined loading conditions. Moreover, direct measurements on sub-block boundaries are missing in the literature.

Regarding the performed research on lath martensite, conflicting observations were made in the literature stating that lath martensite may reveal unexpected ductility whereas it was always believed to be brittle. In FM steels, the overall plasticity can reach 20% with sandwiched specimens [36,37]. Local plasticity along the substructure boundaries was observed to be higher than other regions [36,37]. Large local strains in lath martensite in multiphase steel has also been reported, for example, strain over 80% in [21] and up to 120% in DP steel [22], and above 50% in TRIP steel [38,39]. Other observations, such as dimpled fracture surfaces also support the conclusion on the ductility of lath martensite [19,40,41]. Selected images from the literature clearly showing the potential ductility of lath martensite is given in Fig. 1.4. However, no systematic study on the physical origin of martensite ductility has been reported so far. An in-depth investigation on the underlying ductility mechanisms is therefore of need.
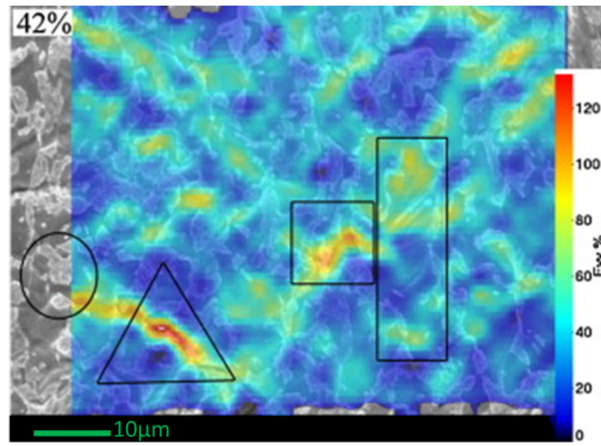
Figure 1.4. A strain map showing high local ductility in martensite (over 100%) close to the phase boundaries in a DP600 steel with an overall strain of 42%. Reproduced from Fig. 5(d) of Ref. [21].

Besides lath martensite, ferrite is another important phase of most steels. Even though its microstructure seems to be simple, the discussions on its plastic behavior is ongoing for more than half a century [42-44]. Because of its body centered cubic lattice structure, the dislocation movement of ferrite is intrinsically complex with many aspects of the anomalous crystallographic slip remaining to be elucidated. Most methods used in the literature again rely mostly on macro scale mechanical experiments, through which it is not straightforward to obtain a link between the local boundary constraints and the active slip systems [45]. The compression-tension asymmetry of body centered cubic metals, as reported in Ref. [46,47], requires more detailed investigations of ferrite under tension because micro-tension tests are much less available in the literature. Hence, it is recommended to examine ferrite with micro-tensile testing, in order to identify the boundary constraints and to acquire the relationship between the local boundary constraints and the active slip systems.

1.2 Objective

The aim of this study is (i) to unravel the micro-plasticity of lath martensite and to determine the contribution of the substructure boundaries to strengthening of the material and elucidate the mechanism of the unexpected ductility. (ii) to understand the relation between the anomalous crystallographic slip of ferrite and the applied boundary constraints of loading, and (iii) to obtain the average morphology around damage sites in a dual phase steel in a statistical way.

1.3 Structure of the thesis

First a statistical view of the distribution of different phases around damage sites in deformed DP steel is obtained by mathematical averaging of a large collection of scanning electron images in **Chapter 2**. An automatic phase correlation method including a novel imaging technique is developed. The results provide a new perspective on damages in multiphase materials.

To perform mechanical tests on individual micro-constituents, a micro-tensile testing method is developed in **Chapter 3**. Straightforward interpretations of results can only be achieved by

easy loading state, therefore, the specimen fabrication method and the specimen alignment are carefully considered to apply a reliable uniaxial loading. Moreover, the force and displacement measurements require a high accuracy due to the small dimensions of the specimens. Detailed tests assessing the reliability of the method are conducted.

With this new uni-axial micro-tensile test methodology, the plasticity in ferrite is studied first in **Chapter 4**. To this end, large ferritic grains are produced through heat treatment of interstitial free steels, allowing fabrication of multiple micro-tensile specimens from a single grain. On the one hand, this allows to examine the reproducibility of the test method and on the other hand, it enables to investigate the anomalous deformation behavior of ferrite as stated above. The mechanical behavior of ferrite single crystal specimens is analyzed in detail in combination with the measurement of the crystallographic orientations of the specimens along with the precise loading state.

Prior to mechanical testing of lath martensite, its crystallography and the distribution of the alloying elements are studied in **Chapter 5**. Since lath martensite in FM steels has already been investigated in the literature, focus is here put on the crystallography and chemistry of lath martensite in a DP steel. Micro-tensile tests on lath martensite of FM steels are performed next, first with two limit cases for the substructure boundary configuration. **Chapter 6** investigates samples with substructure boundaries that are approximately parallel to the loading direction, whereby the resolved stress on the boundary planes is minimal. In contrary, in **Chapter 7,** the opposite limit case is tested, for which the resolved shear stress on the boundary planes is maximal, using tilted boundary configuration to the loading direction. For both cases, heat treatments are conducted to obtain large and well-defined substructures of a FM steel. Micro-tensile specimens can then be made from single packets/blocks, enabling a straightforward analysis. It is quite likely that the plasticity mechanism is different for these two limit configurations. In **Chapter 8**, lath martensite micro-tensile specimens with more arbitrary boundary configurations (in-between the limit cases of Chapter 6 and Chapter 7) are tested. The deformation mechanism of lath martensite in multiphase steels is studied next using DP steel as a typical multiphase steel, given the extensive research on all its aspects in the literature. This allows to verify if the deformation mechanism observed in the FM steel are still active in multiphase steels. Finally, the effects of lath martensite deformation mechanisms in bulk materials is analyzed, exploiting the knowledge acquired from the micro-tensile tests.

References

[1] Inventory of U.S. greenhouse gas emissions and sinks: 1990-2014, U.S. Environmental Protection Agency (2016).

[2] Greenhouse gas emission statistics, European Environment Agency (2016).

[3] N. Lutsey, Review of technical literature and trends related to automobile mass-reduction technology, Report for California air resources board, University of California, (2010).

[4] O. Kwon, K.Y. Lee, G.S. Kim, K.G. Chin, New trends in advanced high strength steel developments for automotive application, Materials Science Forum, 638-642 (2010) 136-141.

[5] Overview report: Future steel vehicle, nature's way to mobility, WorldAutoSteel, (2011).

[6] P. Bowen, C.A. Hippsley, J.F. Knott, Effects of segregation on brittle fracture and fatigue crack growth in coarse-grained, martensitic A533B pressure vessel steel, Acta Metallurgica, 32 (1984) 637-647.

[7] H. Ghassemi-Armaki, R. Maaß, S.P. Bhat, S. Sriram, J.R. Greer, K.S. Kumar, Deformation response of ferrite and martensite in a dual phase steel, Acta Materialia, 62 (2014) 197-211.

[8] C.C. Tasan, J.P.M. Hoefnagels, M.G.D. Geers, Microstructural banding effects clarified through micrographic digital image correlation, Scripta Materialia, 62 (2010) 835–38.

[9] M. Shome, M. Tumuluru, Introduction to welding and joining of advanced high-strength steels (AHSS), Welding and Joining of Advanced High-Strength Steels (AHSS), (2015) 1-8.

[10] W. Gan, S.S. Babu, N. Kapustka, R.H. Wagoner, Microstructural effects on the springback of advanced high-strength steel, Metallurgical and Materials Transactions A, 37 (2006) 3221-3231.

[11] M.C. Theyssier, Manufacturing of advanced high-strength steels (AHSS), Welding and Joining of Advanced High-Strength Steels (AHSS), (2015) 29-53.

[12] C.C. Tasan, J.P.M. Hoefnagels, M. Diehl, D. Yan, F. Roters, D. Raabe, Strain localization and damage in dual phase steels investigated by coupled in-situ deformation experiments and crystal plasticity simulations. International Journal of Plasticity, 63 (2014) 198–210.

[13] R. Kuziak, R.Kawalla, S. Waengler, Advanced high strength steels for automotive industry, Archives of Civil and Mechanical Engineering, 3 (2008) 103-117.

[14] J. Rehrl, K. Mraczek, A. Pichlar, E. Werner, Mechanical properties and fracture behavior of hydrogen charged AHSS/UHSS grades at high- and low strain rate tests, Materials Science and Engineering A, 590 (2014) 360-367.

[15] J.H. Kim, J.H. Sung, K. Piao, R.H. Wagoner, The shear fracture of dual-phase steel, International Journal of Plasticity, 27 (2011) 1658-1676.

[16] N. den Uijl, F. Azakane, S. Kilic, V. Docter, Performance of tensile tested resistance spot and laser welded joints at various angles, Welding in the World, 11 (2012) 143-152.

[17] U. Liedl, S. Traint. E.A. Werner, An unexpected feature of the stress–strain diagram of dual-phase steel, Computational Materials Science, 1-2 (2002) 122-128.

[18] G. Avramovic-Cingara, C.A.R. Saleh, M.K. Jain, D.S. Wilkinson, Void nucleation and growth in dual-phase steel 600 during uniaxial tensile testing, Metallurgical and Materials Transactions A, 40A (2009) 3117-3127.

[19] C.C. Tasan, J.P.M. Hoefnagels, C.H.L.J. ten Horn, M.G.D. Geers, Experimental analysis of strain path dependent ductile damage mechanics and forming limits, Mechanics of Materials, 41 (2009) 1264-1276.

[20] E. Maire, O. Bouaziz, M. di Michiel, C. Verdu, Initiation and growth of damage in a dual-phase steel observed by X-ray microtomography, Acta Materialia, 56 (2008) 4954-4964.

[21] H. Ghadbeigia, C. Pinna, S. Cellotto, J.R. Yates, Local plastic strain evolution in a high strength

dual-phase steel, Materials Science and Engineering A, 527 (2010) 5026-5032.

[22] H. Ghadbeigi, C. Pinna, S. Cellotto, Failure mechanisms in DP600 steel: Initiation, evolution and fracture, Materials Science and Engineering A, 588 (2013) 420-431.

[23] J.P.M. Hoefnagels, C.C. Tasan, F. Maresca, F.J. Peters, V.G. Kouznetsova, Retardation of plastic instability via damage-enabled microstrain delocalization, Journal of Materials Science, 50 (2015) 6882-6897.

[24] T.W.J. de Geus, R.H.J. Peerlings, M.G.D. Geers, Microstructural topology effects on the onset of ductile failure in multi-phase materials-a systematic computational approach, International Journal of Solids and Structures, 67-68 (2015) 326-339.

[25] S. Morito, H. Tanaka, R. Konishi, T. Furuhara, T. Maki, The morphology and crystallography of lath martensite in Fe-C alloys, Acta Materialia, 51 (2003) 1789-1799.

[26] K. Iwashita, Y. Murata, Y. Tsukada, T. Koyama, Formation mechanism of the hierarchic structure in the lath martensite phase in steels, Philosophical Magazine, 91 (2011).

[27] L. Qi, A.G. Khachaturyan, J.W. Morris Jr., The microstructure of dislocated martensitic steel: theory, Acta Materialia, 76 (2014) 23-39.

[28] S. Takaki, K. Ngo-Huynh, N. Nakada, T. Tsuchiyama, Strengthening mechanism in ultra low carbon martensitic steel, ISIJ International, 52 (2012) 710-716.

[29] G. Krauss, Martensite in steel: strength and structure, Materials Science and Engineering A, 273-275 (1999) 40-57.

[30] T. Ohmura, T. Hara, K, Tsuzaki, Evaluation of temper softening behavior of Fe–C binary martensitic steels by nanoindentation, Scripta Materialia, 49 (2003) 1157-1162.

[31] S. Morito, H. Yoshida, T. Maki, X. Huang, Effect of block size on the strength of lath martensite in low carbon steels, Materials Science and Engineering A, 438-440 (2006) 237-240.

[32] T. Ohmura, T. Hara, K, Tsuzaki, Relationship between nanohardness and microstructures in high-purity Fe-C as-quenched and quench-tempered martensite, Journal of Materials Research, 18 (2003) 1465-1470.

[33] A. Shibata, T. Nagoshi, M. Sone, S. Morito, Y. Higo, Micromechanical characterization of deformation behavior in ferrous lath martensite, Journal of Alloys and Compounds, 577 (2013) 555-558.

[34] H. Ghassemi-Armaki, R. Maaß, S.P. Bhat, S. Sriram, J.R. Greer, K.S. Kumar, Deformation response of ferrite and martensite in a dual-phase steel, Acta Materialia, 62 (2014) 197-211.

[35] Y. Mine, K. Hirashita H. Takashima, M. Matsuda, K. Takashima, Micro-tension behavior of lath martensite structures of carbon steel, Materials Science and Engineering A, 560 (2013) 535-544.

[36] M. Michiuchi, S. Nambu, Y. Ishimoto, J. Inoue, T. Koseki, Relationship between local deformation behavior and crystallographic features of as-quenched lath martensite during uniaxial tensile deformation, Acta Materialia, 57 (2009) 5283-5291.

[37] S. Nambu, M. Michiuchi, Y. Ishimoto, K. Asakura, J. Inoue, T. Koseki, Transition in deformation behavior of martensitic steel during large deformation under uniaxial tensile loading, Scripta Materialia, 60 (2009) 221-224.

[38] X. Sun, A. Soulami, K.S. Choi, O. Guzman, W. Chen, Effects of sample geometry and loading rate on tensile ductility of TRIP800 steel, Materials Science and Engineering A, 541 (2012) 1-7.

[39] C. Wang, H. Ding, M. Cai, B. Rolfe, Characterization of microstructures and tensile properties of TRIP-aided steels with different matrix microstructure, Materials Science and Engineering A, 610 (2014) 65-75.

[40] J. Kadkhodapour, A. Butz, S. Ziaei Rad, Mechanisms of void formation during tensile testing in a commercial dual-phase steel, Acta Materialia, 59 (2011) 2575–2588.

[41] X.L. Cai, J. Feng, W.S. Owen, The Dependence of some tensile and fatigue properties of a dual-phase steel on its microstructure, Metallurgical Transactions. A, 16 (1985) 1405–1415.

[42] D. Rodney, J. Bonneville, Dislocations, Physical metallurgy, fifth edition, 2 (2014) 1591-1680.

[43] J.W. Christian, Some surprising features of the plastic deformation of Body-Centered Cubic metals and alloys, Metallurgical Transactions A, 14 (1983) 1237-1256.

[44] G. Taylor, Thermally-activated deformation of BCC metals and alloys, Progress in Materials Science, 36 (1992) 29-61.

[45] P. Franciosi, L.T. Le, G. Monnet, C. Kahloun, M.H. Chavanne, Investigation of slip system activity in iron at room temperature by SEM and AFM in-situ tensile and compression tests of iron single crystals, International Journal of Plasticity, 65 (2015) 226-249.

[46] D. Hull, J.F. Byron, F.W. Noble, Orientation dependence of yield in body-centered cubic metals, Canadian Journal of Physics, 45 (1967) 1091-1099.

[47] J.W. Christian, Some surprising features of the plastic deformation of body-centered cubic metals and alloys, Metallurgical Transactions A, 14 (1983) 1237-1256.

Chapter 2. Systematic and objective identification of the micro- structure around damage directly from images[1]

Abstract

An original experimental approach is presented to automatically determine the average phase distribution around damage sites in multi-phase materials. An objective measure is found to be the average intensity around damage sites, calculated using many images. This method has the following benefits: no phase identification or manual interventions are required, and statistical fluctuations and measurement noise are effectively averaged. The method is demonstrated for dual-phase steel, revealing subtle unexpected differences in the morphology surrounding damage in strongly and weakly banded microstructures.

2.1 Introduction

Multi-phase materials typically consist of multiple phases with distinct mechanical and physical properties. Their fracture behavior is only partially understood, as the morphology (often complex) plays a crucial role (e.g. in multi-phase metals [1], concrete [2], and geophysics [3]). Experimental approaches towards systematic characterization of the microstructural morphology in damaged regions are cumbersome, whereas a reliable methodology might yield new insights and more accurate input for (macroscopic) damage models [4-6].

Different statistical descriptors have been developed for arbitrary (microstructural) morphologies. Well known examples are the two-point probability or auto-correlation function and the lineal path function [7,8]. For an isolated inclusion phase (e.g. spherical particles) additional descriptors have been developed that convey more information, such as the two-point cluster function and the radial distribution function [9]. Almost all measures however require explicit knowledge of the spatial distribution of phases. This knowledge is difficult to obtain experimentally and requires extensive manual processing as the contrast between the phases is often low [10]. Furthermore, they are aimed at the quantification of the distribution and/or size of a single phase, while a conditional probability is needed to characterize the neighborhood of a phase (e.g. morphology around damage).

In a recent numerical study, de Geus et al. [11] characterized the spatial correlation between damage and phase distribution by calculating the average arrangement of phases around damage sites. Extending this analysis to an experimental setting faces the problem that [11] considered equi-sized grains in the model, corresponding to a finite set of discrete positions (distance measures) that coincide with the grains. In reality the position is continuous (finely discretized experimentally through digital images) and the grains are irregular in position and

shape. Furthermore, the interpretation in [11] made use of the explicit knowledge of the phases and damage as a function of the position, not available experimentally.

This letter presents a methodology to quantify the conditional spatial correlation between a uniquely identified feature (e.g. damage) and its surrounding morphology directly from a micrograph, without the need for an explicit description of the morphology. As a proof of principle the average arrangement of martensite and ferrite around damage in a dual-phase steel microstructure is characterized. It is well known that in commercial grades martensite often presents a banded structure, which has a strong influence on the damage [1]. Two different grades of steel are therefore compared that evidence strongly and weakly banded martensite. Tensile tests on these steel grades show that the weakly banded microstructure has a lower fracture strain, which is in disagreement with the common understanding. The proposed analysis provides novel insights into this topic.

2.2 Technique

The spatial correlation analysis is discussed in detail in this section, using an artificial example for which the average distribution of two phases around damage sites is quantified based on an image. Several aspects have to be carefully considered to obtain statistically meaningful results. To simplify notation, the analysis is based on fields that are discretized in space.

Consider the example in Fig. 2.1(a), which shows part of a periodic microstructure comprising two phases: circular inclusions (white) embedded in a matrix (gray) The inclusions have been numerically generated by randomly perturbing the size and position of an initially regular grid of equi-sized circles with diameter $2\overline{R}$. Damage (black) is mimicked by shifting each inclusion to the right, applying a position perturbation, and shrinking it by a factor two. These dimensions are indicated in the zoom next to Fig. 2.1(a). Two fields are used to describe this image: the image intensity I and the damage indicator D. For this example, $I(\vec{x}_i) = 1$ in the inclusion phase (white), $I(\vec{x}_i) = 1/2$ in the matrix (gray), and $I(\vec{x}_i) = 0$ in damage (black). The damage indicator $D(\vec{x}_i) = 1$ inside the damage (black) and is zero elsewhere. The position $\vec{x}_i$ denotes the position of a pixel, taken at the position (i, j) in the pixel matrix. The phase probability P around damage is calculated as the weighted average:

$$P(\Delta\vec{x}) = \frac{\sum_i W(\vec{x}_i)I(\vec{x}_i + \Delta\vec{x})}{\sum_i W(\vec{x}_i)I(\vec{x}_i + \Delta\vec{x})} \tag{1}$$

where the weight factor $W(\vec{x}_i) = D(\vec{x}_i)$ for this example. The spatial average is obtained by looping over all pixels i (optionally excluding a boundary region of half the dimensions of the region-of-interest). It thus corresponds to the normalized discrete convolution between W and I. The result is the expectation value of the intensity, P, at a certain position $\Delta\vec{x}$ relative to the damage site. It scales with the image contrast. In the limit case that I and W are separate fields that are both explicitly known (i.e. zero or one), P is the probability to find I at a certain position relative to W.

The analogy of P with a probability allows the interpretation of its value based on simple statistical arguments. If there is no correlation between I and W, then $P = \overline{I}$, with $\overline{I}$ the spatial

average of I. If at a position $\Delta\vec{x}$ relative to the damage site, more inclusion phase is found than its spatial average, then $P(\Delta\vec{x}) > \bar{I}$ and vice versa.
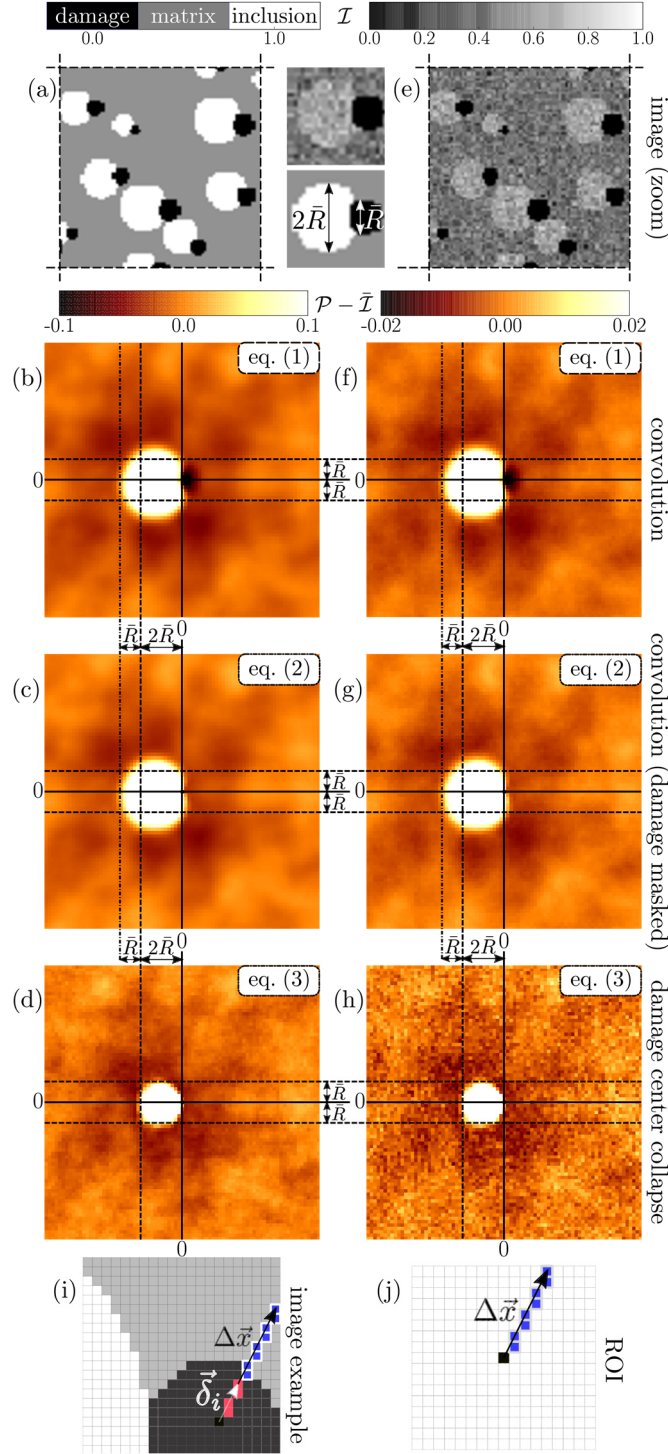
Figure 2.1 Virtual experiment in the ideal setting: no noise and high phase contrast (a–d), and the realistic setting: with noise and low phase contrast (e–h). From top to bottom: (a,e) the two-phase microstructure, (b–h) the average phase arrangement around a damage site calculated in three different ways. (i–j) An illustration of (3) (used in (d,h)).

For the example the result is shown in Fig. 2.1(b), where the color map recovers the extremes

(black and white) of the image. Directly to the left of the center (where the damage is) $P \gg \overline{I}$, i.e. the inclusion phase is identified there. Directly around the center, in all other directions, $P \approx 0$ which corresponds to damage (black in the image). At larger distance, $P < \overline{I}$ corresponding to predominantly matrix phase. Several lighter regions indicate a long-range correlation between damage and inclusion, an intrinsic property of the example for which the inclusion positions are not random but a random perturbation of an initially regular arrangement.

The most obvious artifact in this result is that directly around the damage in the center, damage is identified in a region that corresponds to the size of the damage sites, $\overline{R}$. As the goal is to identify the phase around damage, this cross-correlation of damage should be avoided. It is accounted for through a mask M, which is defined such that $I(\vec{x}_i)$ is ignored for all pixels where $M(\vec{x}_i) = 0$. To remove "damaged" pixels $M(\vec{x}_i) = 1 - D(\vec{x}_i)$. The average phase around damage is now:

$$P(\Delta\vec{x}) = \frac{\sum_i W(\vec{x}_i)[IM](\vec{x}_i + \Delta\vec{x})}{\sum_i W(\vec{x}_i)M(\vec{x}_i + \Delta\vec{x})} \tag{2}$$

where the mask in the numerator ensures that the contribution of I in the damaged areas is omitted, and the mask in the denominator corrects the normalization for the reduced number of data-points. The interpretation of P is therefore unaffected.

The result is shown in Fig. 2.1(c), where the cross-correlation between damage pixels is removed, i.e. the black central region in Fig. 2.1(b) is absent. Instead, matrix phase is identified there, as expected. Although this result is qualitatively correct, quantitatively the statistical properties of the microstructure have not been preserved. To visualize this, the typical dimensions of the damage and inclusions are indicated in Fig. 2.1(c) where the size of the region of elevated inclusion probability (directly to the left of damage) has a diameter of $3\overline{R}$, while, by statistical arguments, it should have a diameter of $2\overline{R}$. This results from equation (2), where every damage pixel is separately taken into account. Hence, the resulting phase distribution is smeared over an area equal to the average damage size, in this case $\overline{R}$.

To obtain a more accurate result, the damage site is collapsed to a single point by using the analogy to the pore-size probability density (the probability that a point lies at a certain distance of the closest pore-edge [12]). The basic idea is to quantify the average phase P at position $\Delta\vec{x}$ relative to the edge of the damage site. Therefore, equation (1) is modified to:

$$P(\Delta\vec{x}) = \frac{\sum_i W(\vec{x}_i)[IM](\vec{x}_i + \vec{\sigma}_i(\Delta\vec{x}) + \Delta\vec{x})}{\sum_i W(\vec{x}_i)M(\vec{x}_i + \vec{\sigma}_i(\Delta\vec{x}) + \Delta\vec{x})} \tag{3}$$

where the weight factor $W(\vec{x}_i)$ equals one only in the geometrical center of the individual damage sites and zero elsewhere, and $\vec{\sigma}_i$ is the distance between the damage site center and its edge, it therefore depends on the orientation of $\Delta\vec{x}$. This is illustrated in Fig. 2.1(i), wherein $\vec{\sigma}_i$ (red) is that part of the relative position vector inside the damage site, and $\Delta\vec{x}$ (blue) is the part outside the damage site. The resulting P, defined in the region-of-interest (ROI), depends on the distance $\Delta\vec{x}$ only, as shown in Fig. 2.1(j). A mask is again used to account for the fact that I is undefined in the (other) damage sites. Note that the same weight has been assigned to

each individual damage site, in different context other choices may be appropriate, straightforwardly applied to (1).

The result is shown in Fig. 2.1(d). As observed, the global pattern is the same as in the earlier results (Fig. 2.1(b,c)). The essential difference is that the size of the region of elevated inclusion probability directly left to damage now has diameter $2\overline{R}$, which coincides with the average inclusion diameter.

Because this method compares the information of all damage sites at once, it is insensitive to (a high degree of) measurement noise and a low intensity contrast between the phases. It only relies on an explicit knowledge of the damage (not of the phases). This is demonstrated by extending the example to a more realistic setting. In Fig. 2.1(e), matrix and inclusions are changed to an intensity close to each other and Gaussian noise is added to mimic image noise. The resulting contrast is low, whereby the noise is of the same amplitude as the intensity contrast between the two phases. The results are shown in Fig. 2.1(f–h). The orange color is again chosen as the average intensity $\overline{I}$. The results coincide with the results of Fig. 2.1(b–d). A limited amount of noise is still visible in Fig. 2.1(h) due to reduced number of data-points (one per damage site). The noise reduces with increasing field-of-view: the root-mean-square of the noise decreases by a factor $\sqrt{n}$, with n the number of damage sites. This dependency was verified using the example from this section (results not shown).

2.3 Proof of principle: the dual-phase steel case

As case study, the average arrangement of martensite and ferrite around damage in a dual-phase steel is characterized. Two grades are compared: one with strongly banded martensite (commercial DP600) and one which has been heat-treated to remove the martensite bands as much as possible. For both cases, a millimeter-sized tensile specimen is loaded to fracture. The microstructure is examined in the cross-section along the tensile direction, at least 50 μm away from the fracture surface. A series of grinding, polishing, and etching steps are applied to create a small height difference between martensite and ferrite, providing contrast in the secondary electron mode of the scanning electron microscope (e.g. Fig. 2.2(a,c) for the two grades). In the resulting images martensite is brighter than ferrite. Several damage sites are also visible in Fig. 2.2(a,c), however they cannot be uniquely identified based on intensity alone. To avoid user intervention, a back-scatter electron image is simultaneously acquired to identify the damage uniquely and automatically (see Fig. 2.2(b,d)), as the brightness is zero in the damage sites. This was verified by detailed examination of multiple damaged cross-sections (e.g. Fig. 2.2(f)). To establish a statistically representative set, a series of 16 and 11 images were captured of the two grades respectively, whereby all the scan settings were kept constant within each batch of images, resulting in a large field-of-view with high spatial resolution.

The different correlation measures (from Section 2.2) are compared for the strongly banded dual-phase steel in Fig. 2.3. Note that the color-scales are normalized with the standard deviation of the intensity, I_σ. All results show the same characteristics: damage occurs in a band of martensite aligned with the tensile direction (horizontal) with ferrite in the other directions (top and bottom). However, several correlation measures reveal artifacts for the considered

ensemble.
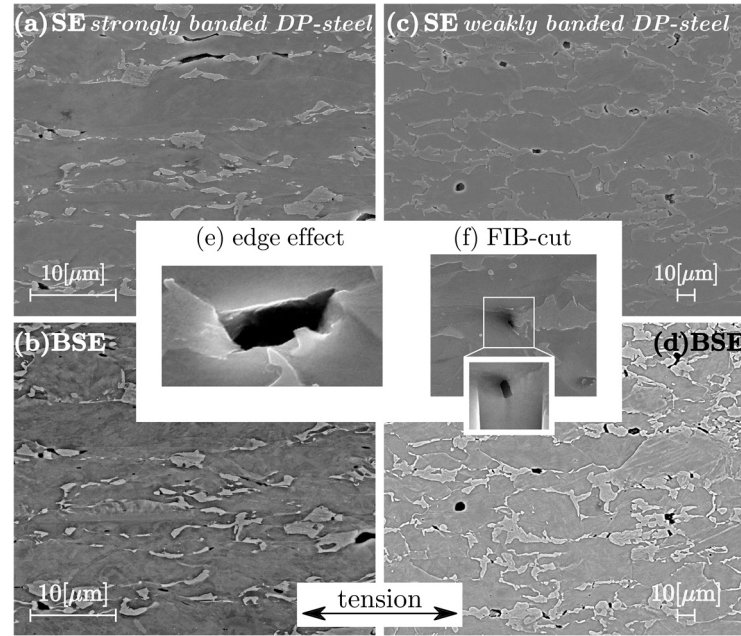
Figure 2.2 Simultaneously acquired secondary electron (top) and back-scatter electron (bottom) images for strongly (left) and weakly (right) banded dual-phase steel. Example of: (e) the edge-effect related to sharp edges, (f) a focused ion beam milled cross-section of a damage site.

In Fig. 2.3(a) equation is applied, showing a clear miss-correlation, with $P \gg \bar{I}$ in a ring of approximately 2 μm around the center. This ring corresponds to the edge-effect around damage (e.g. Fig. 2.3(e)), caused by the intrinsic artifact of electron microscopy imaging yielding a strong edge-effect at sharp edges especially in secondary electron mode. This bright ring can be misidentified as martensite and the smearing effect, discussed above, amplifies this artifact.

To resolve the edge-effect, the mask covering each damage site is expanded using standard image dilation. To minimize the loss of information, the number of dilation iterations varies from damage site to damage site and is equal to the square-root of the number of pixels in that damage site. The result is shown in Fig. 2.3(b), in which the artifact is almost completely removed. What results is the observation that damage occurs in-between regions of martensite that are aligned in the tensile direction with ferrite domains in all other directions.

The applied convolution (equation (2)) has two disadvantages: the result is smeared over a region which scales with the size of the damage, and by definition large damage sites contribute more to the result. In particular the latter may lead to misleading interpretations. To remove this artifact, equation (3) is applied to collapse the damage to a single point in Fig. 2.3(c,d). As explained, also with the edge-effect unmasked, its influence is substantially reduced as its size is no longer increased during the correlation. The final result, with edge effect masked, is shown in Fig. 2.3(d). It has the same characteristics as Fig. 2.3(b), however the regions of martensite are more closely comparable with their average size (estimated from the auto-correlation

function, not shown).

Finally, the two different grades, with strongly and weakly banded martensite, are compared. The average arrangement of phases around damage for the two grades is shown in Fig. 2.4, wherein different axes are used to correct for the different grain sizes of the grades. The results have the same overall pattern: damage occurs in-between martensite aligned with the tensile direction with ferrite in the other directions. For the strongly banded microstructure, the martensite appears in bands (Fig. 2.4(a)), whereas for the weakly banded microstructure the martensite confined in a relatively small region (Fig. 2.4(b)). This implies that even if the bands are not present, damage still occurs in-between martensite domains.
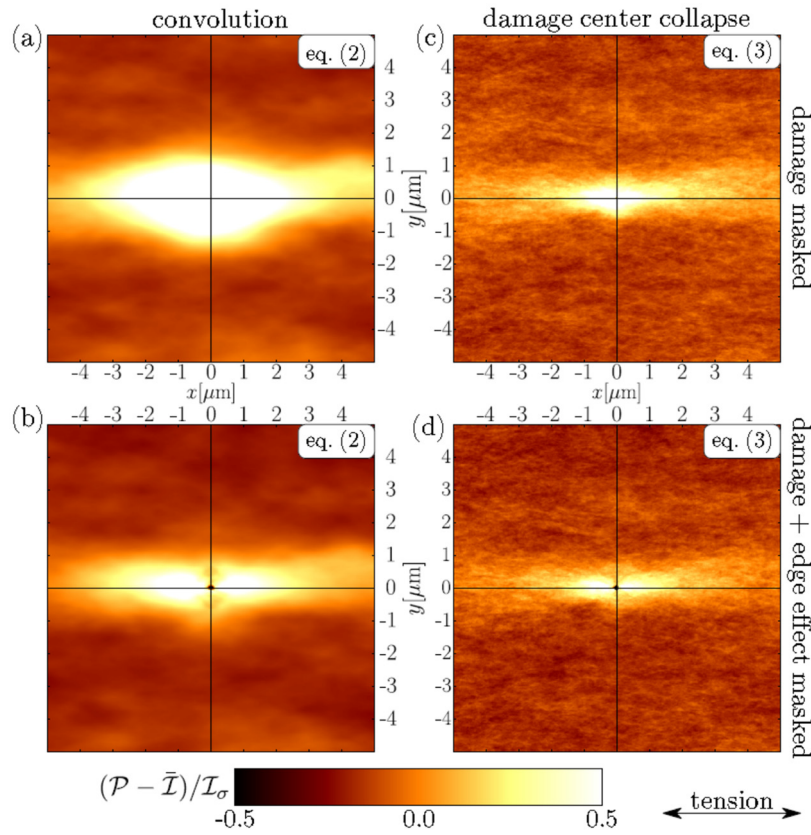
Figure 2.3 Expectation value of the intensity around damage sites in the strongly banded steel using different approaches (columns) and different masks (rows).

The two grades of steel are quantitatively compared to reveal a surprising difference. Whereby the scaling of expectation value, P, with the image contrast, I_σ, is employed to obtain a probability measure that is independent of the image contrast. For Fig. 2.4 this implies that the difference in color between the two results may be interpreted as a difference in martensite and ferrite probability around the damage sites. The darker regions above and below the damage sites in Fig. 2.4(b) compared with Fig. 2.4(a) indicate that the probability of ferrite is lower for the strongly banded microstructure, i.e. the martensite bands are located in clusters. This gives rise to a hypothesis: as the fracture strain is 6% higher for the strongly banded microstructure,

the presence of clusters of martensite above and below the damage may delay propagation. Revisiting the images, e.g. Fig. 2.2, confirms this observation. Although further analysis is needed, it is interesting to see how new insights and hypotheses can originate from the presented objective analysis.
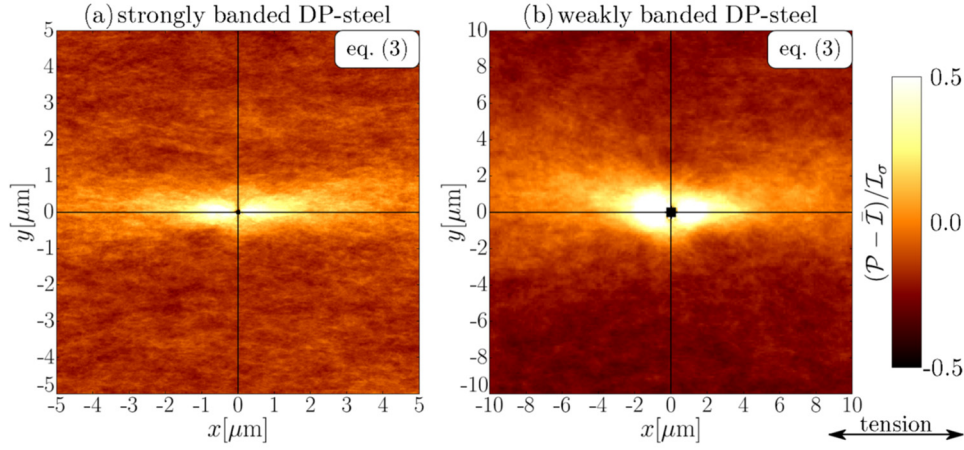
Figure 2.4 Expectation value of the intensity around damage sites in (a) the strongly and (b) weakly banded dual-phase steel.

2.4 Conclusions

A methodology has been presented to quantify the spatial arrangement of phases around damage sites directly using images. This technique is quite general: it may correlate different microstructural features such as phases, cavities, etc. in the fields of materials science, geophysics, medicine and many others. It requires no phase identification, no user interaction, and automatically averages out noise. The interpretation of the result is straightforward as it retains the properties of the original images. In the context of materials, this technique can readily be applied to three-dimensional tomographic or serial sectioning measurements, e.g. from [10, 13, 14], for which it is nearly impossible to perform systematic identifications without an automated analysis technique. Finally, the approach does not rely on a high contrast, which is usually hard to obtain experimentally.

A case study resulted in the average arrangement of martensite and ferrite around damage in the microstructure of a dual-phase steel. This has led to a surprising observation, easily overlooked otherwise. This is the key added value of this methodology.

The results also open up the possibility to use the identified average arrangement of phases as a predictive tool. Indeed, in a preliminary study, using the numerical results of [11], the fracture initiation sites have been identified accurately.

References

[1] C.C. Tasan, J.P.M. Hoefnagels, M.G.D. Geers, Microstructural banding effects clarified through micrographic digital image correlation, Scripta Materialia, 62 (2010) 835–838.

[2] H. Elaqra, N. Godin, G. Peix, M. R'Mili, G. Fantozzi, Damage evolution analysis in mortar, during compressive loading using acoustic emission and X-ray tomography: Effects of the sand/cement ratio, Cement and Concrete Research, 37 (2007) 703–713.

[3] A. Torabi, H. Fossen, B. Alaei, Application of spatial correlation functions in permeability estimation of deformation bands in porous rocks, Journal of Geophysical Research, Solid Earth, 113 (2008) 1–10.

[4] K. Siruguet, J.B. Leblond, Effect of void locking by inclusions upon the plastic behavior of porous ductile solids-I: theoretical modeling and numerical study of void growth, International Journal of Plasticity, 20 (2004) 225–254.

[5] C. Hu, J. Bai, S. Ghosh, Micromechanical and macroscopic models of ductile fracture in particle reinforced metallic materials, Modelling and Simulation in Materials Science and Engineering, 15 (2007) 377–392.

[6] E. Maire, O. Bouaziz, M. Di Michiel, C. Verdu, Initiation and growth of damage in a dual-phase steel observed by X-ray microtomography, Acta Materialia, 56 (2008) 4954–4964.

[7] S. Torquato, G. Stell, Microstructure of two-phase random media. III. The n-point matrix probability functions for fully penetrable spheres, Journal of Chemical Physics, 79 (1983) 1505.

[8] P. Louis, A. M. Gokhale, Application of Image Analysis for Characterization of Spatial Arrangements of Features in Microstructure, Metallurgical and Materials Transactions A, 26 (1995) 1449–1456.

[9] K.H. Hanish, D. Stoyan, Stereological estimation of the radial distribution function of centres of spheres, Journal of Microscopy, 122 (1981) 131–141.

[10] A. Borbély, F.F. Csikor, S. Zabler, P. Cloetens, H. Biermann, Three-dimensional characterization of the microstructure of a metal-matrix composite by holotomography, Materials Science and Engineering A, 367 (2004) 40–50.

[11] T.W.J. de Geus, R.H.J. Peerlings, M.G.D. Geers, Microstructural topology effects on the onset of ductile failure in multi-phase materials, A systematic computational approach, International Journal of Solids and Structures, 67-68 (2015) 326–339.

[12] A.E. Scheidegger, The physics of flow through porous media, Macmillan (1960).

[13] M. Li, S. Ghosh, O. Richmond, An experimental-computational approach to the investigation of damage evolution in discontinuously reinforced aluminum matrix composite, Acta Materialia, 47 (1999) 3515–3532.

[14] C. Landron, E. Maire, J. Adrien, H. Suhonen, P. Cloetens, O. Bouaziz, Non-destructive 3-D reconstruction of the martensitic phase in a dual-phase steel using synchrotron holo-tomography, Scripta Materialia, 66 (2012) 1077–1080.

Chapter 3. Uni-axial nano-force tensile test of individual constituents from bulk material[1]

Abstract

For both single-phase and multi-phase metallic materials, it is necessary to understand the mechanical behavior on the grain-size scale in detail to get information that is not obtainable from macro-scale mechanical characterizations. This paper presents a methodology for uniaxial tensile testing of micro-specimens isolated from a bulk material. The proposed concept of multiple parallel micro-tensile specimens at the tip of a macro-sized wedge reduces the alignment work and offers an easy way for specimen handling. The selection of site-specific specimens is based on detailed microstructural and crystallographic characterization. Three kinds of representative specimens are presented to illustrate the wide range of application of the methodology for a variety of materials. Highly accurate force and displacement measured is demonstrated, while accurate in-/out-of-plane alignment keeps specimen bending to a minimum. Combined with detailed material characterization on both sides of the micro-specimens, this method yields detailed insights into the micro-mechanics of bulk materials which is hard to obtain from traditional macro-mechanical tests.

3.1. Introduction

Multiphase materials are increasingly used in industry because the combination of different phases can yield a material with mechanical properties that exceed those of the individual phases, as typical for steels. Examples of multiphase steels include advanced high strength steels, such as dual-phase (DP) steel, transformation-induced plasticity steel and twinning induced plasticity steel, all consisting of more than one phases such as ferrite, martensite, bainite and possibly (retained) austenite. The presence of multiple phases improves the overall mechanical response of materials for applications where traditionally conflicting properties are required, for example, high strength combined with good formability. In order to understand the contribution of each phase, one would like to measure its mechanical properties with a method that is able to isolate the neighboring phases and interfaces. It is generally too difficult to obtain the three-dimensional stress state locally in individual phases from a macro-specimen, which prevents detailed micro-scale analyses. Furthermore, the phases often influence each other during the fabrication process or even during storage and usage for some materials, which makes that the micro-mechanical behavior of the constituents different from that of a bulk material made of a single phase. Let us consider DP steel as an example. The martensite and ferrite phases influence each other in terms of their element distribution, phase volume fraction, and their mechanical behaviors are coupled [1]. For instance, carbon in the super saturated

---

martensite diffuses towards the surrounding ferrite grains, which is one of the reasons why the ferrite grains close to martensite are stronger than those which do not share a boundary with martensite and thus have a lower carbon content. Therefore, the measured mechanical behavior of a macro-scale specimen of a single phase material does not directly apply to the corresponding phase in the composite, which prevents accurate model predictions of the composite's mechanics. It would therefore be highly desirable to be able to perform a well-defined mechanical test on an individual constituent that is directly extracted from its multiphase surrounding.

Also for single-phase materials, a uni-axial tensile test on single grains is desirable. As each grain has different crystal orientations, the mechanics of single grains and grain boundaries should be understood to predict the overall material behavior. Macro-sized single-crystal specimens can be fabricated by enlarging the grains using heat treatments, e.g. [2]. However, for engineering materials, the high alloy content typically prevents the growth of huge crystals at low cost. Moreover, even for a single-phase material it is often incorrect to directly apply the conclusions of a macro-scale single-crystal test to micron-sized grains in the associated engineering materials. Micro-sized grains show discrete mechanical behavior due to a limited number of dislocations, precipitates, etc. Moreover, so-called 'size effects' in mechanical behavior of single-phase materials have triggered intense research in the last decades [3, 4]. The extrinsic size effect, i.e. due to the specimen size, should not be neglected when projecting macro-scale tests to the micro-scale. For more complex single phase material like bainite and martensite, which has a fundamental structure unit, the so called lath, with the thickness of sub-micrometers, it is critical to understand the material behavior well at the 'lath scale'. The internal (packet-/block-/subblock-) boundaries, between groups of laths, as found in martensite and bainite, are critical ingredients to improve the mechanical properties of advanced high strength steels [5]. However, their roles on the mechanics have so far only been studied indirectly through macro-scale specimens [6, 7], or from micro-specimens subjected to a complex loading state (e.g. bending test [8, 9]). Therefore, mechanical tests with a simple stress state at the micron scale are essential to understand the complex mechanics of simple single-phase materials, complex single-phase materials (e.g., bainite and martensite) and their size effects, as well as composite and multi-phase materials.

As argued above, it is important to test the mechanical properties of individual phases or micro-sized grains. Therefore, a dedicated micro-mechanical test methodology is developed, which should satisfy the following requirements: (1) it should be with capacity to test individual phases; (2) the size of the micro-specimens should be smaller than the grains of individual phases; (3) specimen preparation methods should give a high shape accuracy of the specimens on the corresponding scale; (4) the handling of these micro-sized specimens, as an integral part of the methodology, should be relatively simple, since that transportation and mounting of the micro-sized specimens without pre-loading them is a well-known challenge; (5) it is important that the method allows for site-specific specimen fabrication based on detailed micro-structural characterization over a large material surface area (e.g. local crystal orientation/ chemical composition), which in turn will also assist the analysis of the mechanical behavior afterwards;

(6) the applied loading and deformation should be measured with high sensitivity and accuracy; (7) in-situ testing should be feasible in order to record the complete deformation process of the specimens.

Among the existing methods of micro-mechanical testing, static tests like micro-bending tests [8] and micro-torsion [10] as well as micro- and nano-indentation [11, 12] are often used. However, for these tests, the local stress state (in the gauge section) is hard to obtain due to the interaction of the (highly) inhomogeneous loading state with the microstructure which is also inhomogeneous at the same length scale. This makes it difficult to derive exact values of the mechanical properties. In contrast, similar to testing at the macro scale, uni-axial tension and compression at the micro-scale are mechanical tests with straight-forward loading conditions. The micro-pillar compression test is widely applied, for example, Jirkova et al. investigated the effect of retained austenite on micro- and macro-mechanical properties of quenching and partitioning steels [13], while Kheradman et al. studied the role of grain boundary in plastic deformation using micro-pillar compression test [14]. However, compression and tensile tests cannot replace each other, because the small-scale mechanics is never exactly the same, for instance: (1) the onset of localization and the initiation and evolution of damage and fracture is completely different, and (2) for BCC metals, the so-called non-Schmidt effect [15] causes the plastic behavior under tension and compression to be asymmetric. Therefore, a well-defined micro-tension test would be a welcome addition to the many micro-pillar compression tests in the literature and to yield deeper insight into the micro-mechanical mechanisms underlying the macroscopic behavior.

The aim of this study is to establish a highly-sensitive and reproducible methodology for uniaxial micro-tensile testing of single components extracted from multi-phase materials and testing of individual grains of single-phase materials. The paper discusses the details of the methodology designed for testing of micro-tensile specimens from bulk materials, which includes specimen preparation, specimen alignment and the procedures for uniaxial tensile testing. Tests on single-grain specimens made from interstitial free (IF) steel and micron-sized martensite specimens with a selected orientation relative to the loading direction will serve to demonstrate the capability for micro-tensile testing of single-phase materials. Tests on ferrite specimens from DP steel will demonstrate the capability for testing of a single phase extracted from a multi-phase material.

3.2 Experiments

3.2.1 Specimen fabrication

The design of the experiment needs careful considerations due to the miniature size of the specimens. Starting from the bulk material, first a wedge is prepared with a tip that ends in a straight knife edge. Next, a detailed analysis of the microstructure and crystallographic orientation is performed on both the front side and the backside of the wedge. Finally, micro tensile specimens are fabricated from the wedge tip in such a way that they remain attached to the wedge, making them easy to handle. Focused ion beam (FIB) is chosen to fabricate the micro-size tensile specimens because of its fabrication accuracy. Care should be taken that the

wedge tip is thin enough to enable FIB milling of the specimens, with a thickness that is smaller than the length scale of the microstructure, such that a double-side analysis of the wedge tip is representative for the final micro-tensile specimens to be fabricated from the wedge. For instance, when testing single grains, the double-side measurement ensures that each specimen consists of a single grain. For the specimens with internal boundaries, the double-side measurement gives detailed information of the number and position of boundaries, the boundary orientation (inclination) in 3D and crystallographic information of the grains.

Preparation of the wedge is realized by grinding a piece of bulk material under an angle into a wedge shape. The original bulk sheet material with thickness t is cut into small chip-sized windows with a dimension of 10×9×t in mm (t = 1.0 mm for all tests shown here). The back side of the piece is mechanically ground and polished. Subsequently, the front side is ground and polished under an angle, by gluing the bottom to a specimen holder of a semi-automatic grinding/polishing machine ('Target machine' from Struers), which allows the front side to be tilted at the desired angle with respect to the grinding/polishing disk. After both sides have been polished, a wedge has been produced with a razor sharp tip edge equal to the tilt angle on one side and an end thickness of roughly ½t on the other side. Even though the grinding and polishing is performed carefully with many fine polishing steps (ending with a 10-minute OPS polish with 40 nm silica particles), it is obvious that micron-scale mechanical deformation will always be introduced to the wedge tip, as can easily be seen from the waviness of the tip in Fig. 3.1(a). This means that the wedge tip material has undergone hardening and perhaps even damage. It is therefore essential to remove the deformation layer of the wedge with a method, which does not introduce (new) mechanical deformation. Therefore, electrochemical polishing is subsequently applied. A schematic illustration of the electrochemical polishing process is shown by the insert of Fig. 3.1(b). The voltage is 30V and the flow rate is 15-20 and the polishing time is ranged from 15s to 30s using the LectroPol 5 from Struers with Electrolyte A2. These parameters were carefully optimized to obtain a perfect finish, as shown for a DP steel wedge in Fig. 3.1(b). The wedge tip is straight and smooth, i.e. the waviness has been removed, which suggests that the deformed layer by grinding showed in Fig. 3.1 has been completely removed. Moreover, the phase/grain boundaries of this DP steel are continuous from one side to the opposite side, which means that there is only one grain in the thickness direction. Note that the electrochemical polishing process should not be too long, because it rounds off the tip angle, which leads to a (much) longer FIB time in the subsequent steps. To verify that after electrochemical polishing the wedge is sufficiently deformation free, an EBSD scan of both sides of the edge region of the wedge has been carried out. The resulting inverse pole figure map, image quality map, and kernel average misorientation map are shown in Fig. 3.2. The gauge parts of the future micro-tensile specimens are located between the white dashed lines, where it can be seen that the large (ferrite) grains, which easily reveal mechanical deformation due to grinding and polishing, have a common inverse pole figure color with a kernel average misorientation that remains below ~1°. This confirms that the specimen area is free from mechanical deformation.
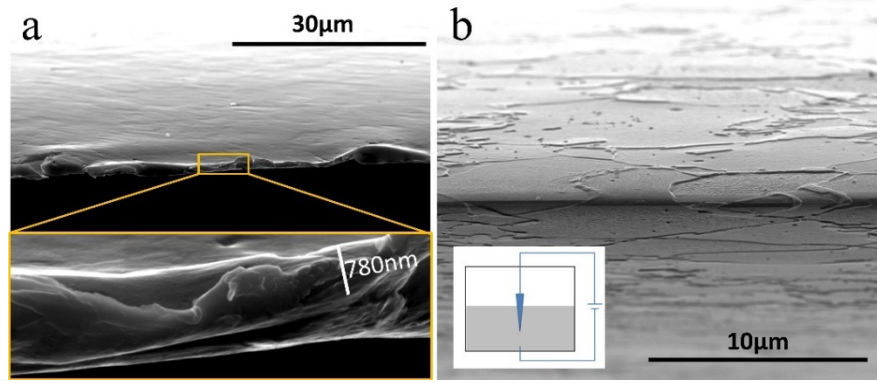
Figure 3.1 (a) Scanning electron microscope (SEM) secondary electron (SE) image of front view of the wedge tip after mechanical polishing, with obvious mechanical deformation at the edge tip. (b) SEM SE image of a DP steel wedge after electrochemical polishing, observed from the top of the wedge. The tip of the wedge is sharp in the center, across which clear grain/phase boundaries running from the front side to the back side are visible. The insert shows a schematic illustration of the adopted electrochemical polishing process with wedge tip dipped in electrolyte.

At the location of the gauge section of the specimens (dashed white line in Fig. 3.2) the wedge tip is thin enough, i.e. with a thickness of less than 10 μm, which allows to mill specimens by FIB. This concept of a thin macro-wedge from which multiple parallel micro-compression specimens are milled with FIB is similar to the method of micro-wedge used in [16], the 9 mm-long wedge tip allows to have many parallel micro-tensile specimens, which are free standing but are connected to the wedge at their base (as shown by the blue specimen contour in Fig. 3.2(a)). The difference to the method in [16] is that an extra electro-chemical polishing process is introduced to remove the deformation caused by mechanical grinding and polishing step. This macro-wedge permits easy transportation, mounting and demounting of the micro-tensile specimens since one only needs to handle the wedge, as opposed to stand-alone micro-tensile specimens that requires dedicated effort to assemble a micro-sized specimen into the grippers using micromanipulators [e.g. in 17]. In addition, compared to a single free-standing specimen fabricated on top of a needle specimen, where only one micro-tensile specimen can be fabricated [18], the current wedge method saves time for mounting and aligning of the specimens in the tensile stage since all micro-tensile specimens are parallel as they are milled with FIB in a single process.

If a specific region needs to be selected, the wedge concept is especially suited as it allows for high resolution microstructural characterization from both sides, e.g., with EBSD as shown in Fig. 3.2. The selection can be morphological (e.g. a certain phase, grain boundary regions, or inter-grain regions in a multi-phase material), or crystallographic (e.g. a certain region with a specific orientation or a certain type of grain boundary). In fact, due to the FIB procedure used, as discussed below, the backside of the micro-specimen is part of the backside of the wedge, i.e. it is not touched by FIB. Therefore, the morphology of the grains at this wedge side, revealed by the electrochemical polishing, can be imaged with SEM in SE mode. Hence, a millimeter-sized area can be scanned quickly for selecting interesting micro-specimen fabrication sites, e.g., with

a specific grain boundary orientation. Of course, additional EBSD analyses are needed if selection should occur on the basis of phase orientations. An example of this region selection for martensite with a preferred orientation based on EBSD measurements is shown below.
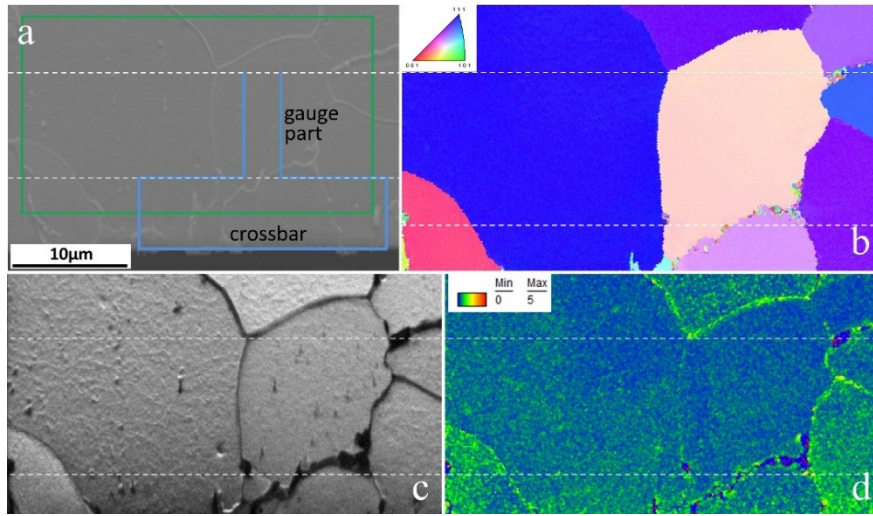
Figure 3.2 EBSD measurement of the wedge tip fabricated from a DP600 steel sheet as an example. (a) SEM SE picture of the edge part, with internal grain/phase boundaries. The green frame indicates the area that is measured with EBSD and shown in subplots (b-d). For reference, the blue frame represents the contour of a T-shaped micro-tensile specimen (consisting of a rectangular gauge section and crossbar for load application), while the area between the white dashed lines is the region where the gauge part of the micro-tensile specimens will be located, as also indicated in subplot (b-d). (b) An inverse pole figure map of the scanned area; the uniform color within each grain indicates a common orientation. (c) the EBSD image quality map of the same area, where the grain/phase boundaries are clearly visible. A high image quality is obtained in the ferrite grain; the black regions are martensite. (d) Kernel average misorientation map of the scanned area, which shows very small misorientation in the ferrite grains. This confirms that the wedge is free from mechanical deformation, since the large and relatively soft ferrite grains would be deformed first.

It is well known that FIB milling introduces some lattice defects in a thin surface layer due to gallium ion implanting [19], including dislocations and other defects that may change the mechanical property of the specimen [20]. In the past decades, considerable research on the FIB introduced material damage was carried out on Si [e.g. 21,22] since FIB is widely applied in the semi-conductor industry, while studies of the FIB induced damage on other material is limited [19, 23]. Generally, an amorphous layer is formed in the FIB milling process, of which the thickness was found to be related to the energy of the ion beam, the beam current and the landing angle of the beam on the material surface [23]. Therefore, the extent of FIB-induced damage can be minimized by lowering the beam energy, beam current, and landing angle.
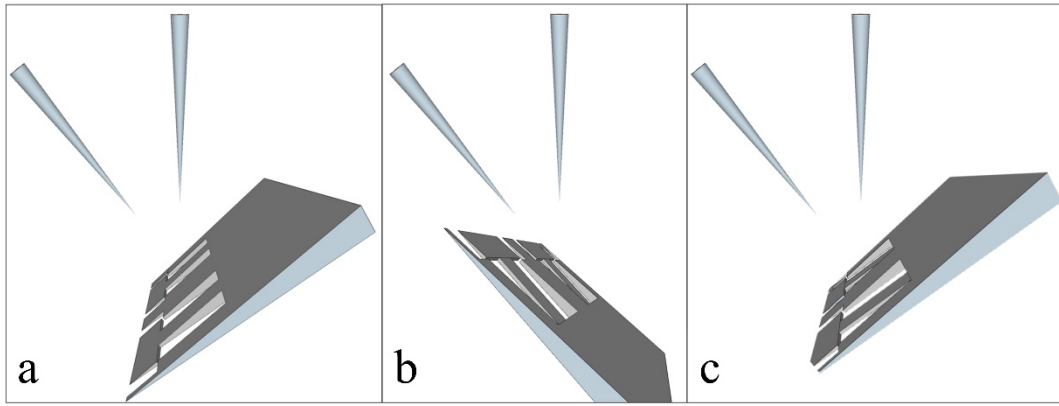
Figure 3.3 Schematic illustration of the FIB milling process of the tensile bars, combined with SEM images at each step. In the first step (a), the backside of the wedge is aligned to be perpendicular to the ion beam for a coarse milling of T-shaped specimens. Second (b), the wedge is aligned with the backside parallel to the ion beam axis, after which the top side of the micro-tensile specimens is milled under shallow angle to obtain a constant specimen thickness. Finally, in (c), the wedge is aligned again with the backside perpendicular to the ion beam for the fine milling of the specimen side which yields better surface finishing quality and higher shape accuracy.

Given the considerations above, the milling process is set up in order to minimize the influence of FIB to the specimens, as shown in Fig. 3.3 schematically. The micro-tensile bars are fabricated with a dual beam SEM-FIB (FEI Quanta 3D FEG), using an ion acceleration voltage of 30kV progressing from a larger beam current for coarse milling to a finer beam current for a final surface finish. First the specimen is placed such that the back plane of the wedge is perpendicular to the ion beam and a T-shaped micro-specimen is milled with a beam current of 3nA at the wedge tip. At this point the thickness of the gauge part of T-shaped micro-specimen still decreases towards the wedge tip. Secondly, the back plane of the wedge is aligned parallel to the ion beam, see Fig. 3.3(b), and using an ion beam current of 1nA a small layer is removed from the specimen top plane, thereby making the thickness of gauge section constant and removing the prior 3nA FIB-induced damage. Furthermore, a 0.3nA surface cleaning is applied to remove the 1nA FIB-induced damage and provide an accurate final shape. In the third step, the back plane is rotated perpendicular to the ion beam, as in step one. The side planes of the micro-specimens are cleaned with beam current 0.3nA to obtain a high shape accuracy and surface quality. Note that the backside has not been exposed to FIB at all. Special care is taken to ensure that the micro-tensile specimens on the same wedge have parallel axes. This means that during the fabrication of all specimens, no rotation of the wedge is made between micro-specimens during the first step and the third step. In the second step, the tilt angle of the wedge is also kept the same for all micro-tensile specimens.

3.2.2 Experimental setup

The tensile test is conducted with a recently built nano-tensile stage (NTS) that is equipped with accurate force and displacement measurement techniques and allows for precise specimen alignment. The NTS is composed of two modules, as is shown in Fig. 3.4(a). The specimen is

mounted on the left module indicated with 'wedge mounting and rotation' in the figure, which can be rotated in x-y plane about the z-axis in a range of ±0.7° and tilted in the x-z plane about the y-axis in a range of -1.9° to 0.5°. Due to the final electro-chemical polishing step of the wedge, the backside of the wedge shows a minor curvature over the first ~100 micrometers starting from the tip inwards, which causes the specimen back side to be the tilted a few degrees with respect to the wedge end. To tilt back all micro-specimens in a wedge correctly, a simple pre-tilted wedge holder (see insert in Fig. 3.4(b)) has been designed, using a pre-tilt angle that is measured separately for each wedge using surface profilometer. The wedge is fixed by a small screw onto this wedge holder, which is then mounted on the specimen-mounting module by a set of horizontal clamps, which push the holder slightly downwards against three stop pins, and a vertical clamp, as shown in Fig. 3.4(b). This ensures a stable specimen mounting throughout the testing process.
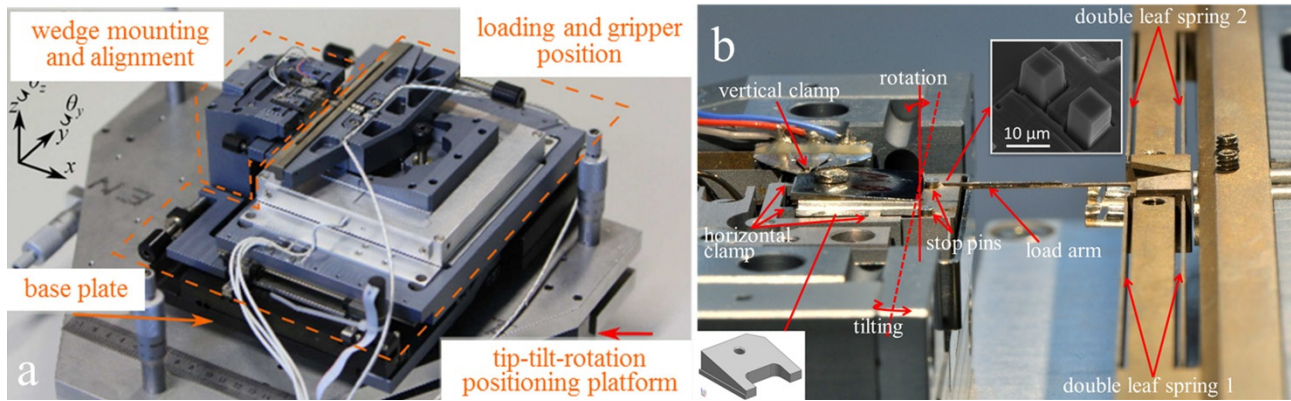
Figure 3.4 (a) the nano-tensile stage mounted on the top of a tilt-rotation positioning stage. (b) a closer view of the specimen mounting configuration and the double leaf spring load cell and double leaf spring reference cell. The top insert shows the two-teeth loading gripper and the bottom insert a sketch of the tapered wedge holder.

The main component of the right module is a piezo-block which can be positioned coarsely in x, y and z directions by manual screws, while a fine movement with 7 nm precision over a 200 μm range that is realized using the x,y,z piezo-block activation (MCL NanoT225). The left side of the piezo block contains a custom load cell, which consists of one double leaf spring mechanism that measures the force on the specimen and a second double leaf spring mechanism to correct for systematic (e.g. temperature) influences. The first double leaf spring mechanism holds a long free-standing loading arm. At the left end of the loading arm, a gripper is located, which has two micron-sized rectangular teeth milled with FIB pointing upwards, as shown in the top insert in Fig. 3.4(b). These two teeth are used to load a micro-specimen by pulling at its crossbar. The high accuracy of the force measurement will be validated below. The tensile test is carried out under a surface profilometer (Bruker NPFLEX) on a vibration-isolated table to minimize external vibrations. In addition, the tensile stage is also designed for *in-situ* testing inside a SEM. More design details of the NTS can be found in [24].

3.2.3 Specimen alignment and testing

After mounting the wedge on the nano-tensile stage, accurate specimen alignment with respect to the loading direction is required to avoid complex loading caused by bending [17, 24]. Following criteria by Bergers *et al.* [24], for example, for a micro-tensile specimen gauge dimension of 9×3×2.5 μm^3, the in-plane rotation misalignment between the specimen axis and the loading axis has to be smaller than 11mrad (0.68°), and the out-of-plane tilt misalignment may not exceed 10mrad (0.57°) to limit bending stress to 0.5% of the imposed uni-axial stress.

The specimen alignment involves two steps, the out-of-plane alignment (tilt) and the in-plane (rotation) alignment. The tilt alignment is shown in Fig. 3.5(a-c). The tilt angle of the load axis is measured by tracking the movement direction of the gripper using Digital Height Correlation (DHC) on measured surface height profiles [25]. Surface profiles of the loading arm are measured by optical profilometer at two positions that are ~200 μm displaced in the x direction (Fig. 3.5(a,b)). The three-dimensional displacement of the region in the white frame is tracked by DHC which corresponds to the three-dimensional loading direction. Using the optical profilometer, the tilt angle of the micro-specimen is obtained by directly fitting a plane through surface profile measurement of the specimen gauge part, as indicated by the white frame in Fig. 3.5(c). The tilt misalignment between the 3D loading direction and the specimen axis is then calculated and corrected by tilting the specimen mounting block toward the loading axis. The procedure is repeated until the misalignment is within the allowed range, typically, one or two iterations suffice.
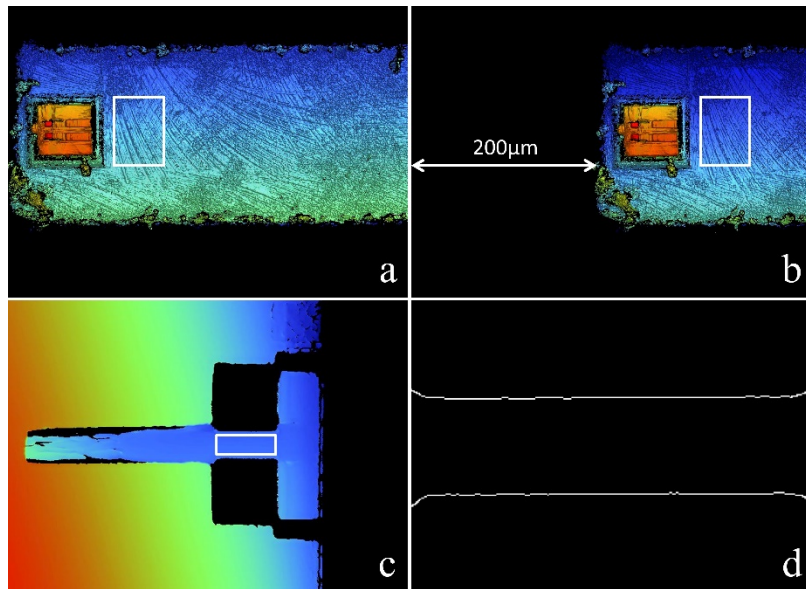
Figure 3.5 The specimen alignment procedure. (a,b) Loading axis out-of-plane (tilt) and in-plane (rotation) angle measurement by tracking the displacement of the white frame area in 3D.(c) Specimen loading axis out-of-plane (tilt) angle measurement by fitting the plane of the gauge part of the specimen in the white frame. (d) Specimen loading axis in-plane rotation angle measurement by edge detection. The length of the specimen gauge section is 9μm.

Similarly, for the rotation alignment, the in-plane difference between the specimen axis and the loading direction also needs to be corrected. The above-measured 3D loading direction is also used to correct this in-plane rotation with respect to the field of view. The specimen axis direction is obtained by detecting the edge of the specimen gauge via thresh holding of the pixel intensity, as shown in Fig. 3.5(d). The two horizontal lines in the gauge part of the specimen are two edges of the specimen front surface, which are parallel to the specimen length axis. The vector describing the axis direction of the specimen is obtained by averaging the directions of these two lines. The in-plane rotation misalignment between the loading axis and the specimen axis is then obtained and corrected by rotating the specimen axis towards the loading axis until the difference is within the allowed range.

The micro-tensile test can now be executed. The gripper is moved from the bottom toward the plane of the micro-specimen, as shown in top-view optical images in Fig. 3.6(a,b), after which the gripper is moved toward the crossbar of the specimen for loading (Fig.3.6(b,c)). The cross bar is now displaced to apply tension and Fig. 3.6(d) shows that two slip traces appear on the specimen surface.
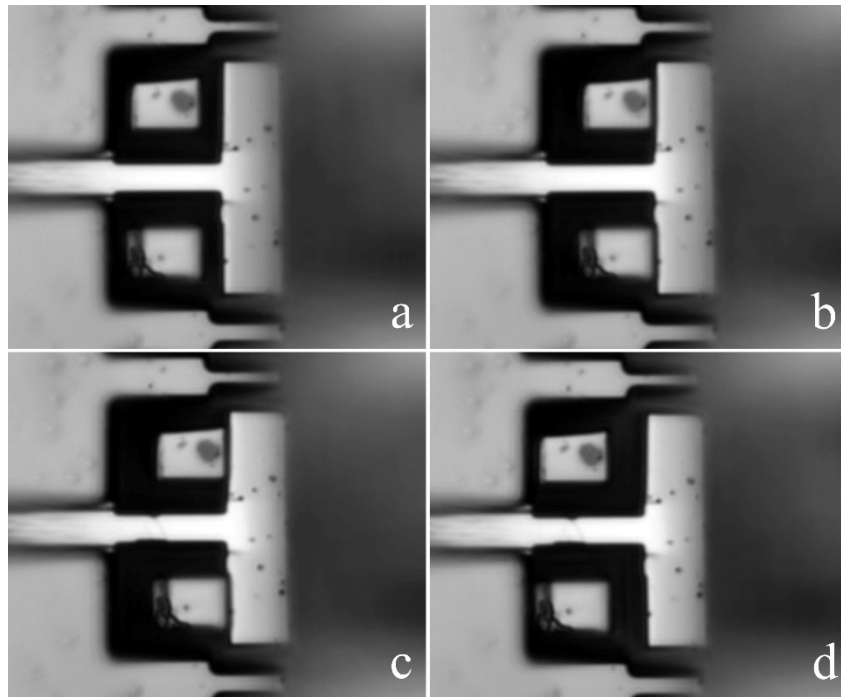
Figure 3.6 Top view optical image series of the gripping process and tensile test of a 9μm-long micro-tensile specimen. (a) The specimen is gripped from the bottom, where the blurred view of the gripper teeth indicates that the height of the teeth surface is lower than the specimen gauge surface at the start of gripping process. (b) The gripper is raised and moved toward the crossbar of the specimen at which the loading is started in (c) after the contact with the crossbar. (d) Slip traces appear on the surface of the specimen gauge part, after which the griper is reversed to interrupt loading, in order to avoid severe plastic deformation for a better identification of the slip systems. In case a complete stress-strain curve of the specimen is required, the loading continues until the specimen is fractured.

3.2.4 Force and displacement measurement and stress-strain curve

The small dimensions of the tensile specimens require an accurate force measurement. For a typical fracture stress of 600 MPa, the fracture force of the tensile specimen is 6 mN for a specimen cross section of 10 μm^2. Therefore, a load cell with the force range 0-25 mN is used with a precision of 10^{-4} of the full range, which is 2.5 μN.

As stated already, the gripper with its two teeth is fabricated at the tip of a (long) load arm, which is attached to a double-leaf spring mechanism, which constrains all degrees of freedom of the gripper motion except for the forward/backward motion, see Fig. 3.4. The force measurement is realized by measuring the deflection of the double-leaf spring under load with a capacitive sensor (Probe C5-D, driver CPL-190 from LionSensor), where the calibrated leaf spring stiffness is designed to yield the desired force range [24]. For such minute forces, the force measurement is highly sensitive to background influences caused by thermal fluctuations, environmental vibrations, and tilt-induced deflections of the leaf spring. Therefore, to measure these background influences, a second identical double-leaf spring is designed in a mirrored configuration as part of the same load cell. The corrected force measurement is obtained by subtraction of the specimen force by the background force with a sampling rate of 10Hz; more details are given in [25]. The effectiveness of this corrected measurement can be seen at the left of Fig. 3.8(a) below, as the corrected noise in the force is small compared to the applied load to the micro-tensile specimen. The two double-leaf spring mechanisms has been fabricated by wire electrical discharge machining (EDM) of a TiAlV alloy with a high yield strain (and thus large maximum elastic deflection) and good manufacturing properties. The load arm end with a cube size of 50^3 μm^3, which was produced by wire EDM from a 0.3mm-thick plate of TiAlV. Using FIB milling, the top of the cube has been further milled to shape the gripper with its two loading teeth, as shown in Fig. 3.4(b).

The displacement measurement is carried out using a dedicated digital image correlation (DIC) algorithm, see Fig. 3.7. Images are taken from the start of loading until the fracture of the specimen. The blue frames in Fig. 3.7 are correlated to obtain the rigid body motion during the test, caused by drift in the test setup. The red frame at the end of the specimen is tracked as well. The difference between the displacement of the red frame and the blue frames is the elongation of the specimen gauge part. In addition, the purple frames are the teeth of the grippers, they are traced to determine the touching point of the gripper to the specimen, which is the starting time of loading (Fig. 3.8(b)).

The micro-tensile test is initiated by pulling the crossbar to the micro-specimen with the gripper teeth, which leads to a steady increase of the force on the force-time curve (Fig. 3.8(a)). On the gripper displacement-time curve (Fig. 3.8(b)), the (initially high) slope of the curve reflects the displacement rate of the freely moving gripper which follows the applied displacement rate of the leaf spring mechanism. After the gripper makes contact with the specimen crossbar, the gripper displacement rate significantely decreases, which is accommodated by deflection of the leaf spring. This load initiation point is indicated by the arrows in Fig. 3.8(a,b). The force and displacement data can be accurately synchronized by

aligning the load initiation points in time, which are determined by fitting two lines to each curve. An example of the resulting stress-strain curve is shown in Fig. 3.8(c). The apparent irregularities in the plastic part of the stress-strain curve are caused by the inhomogeneous deformation in the gauge section of the micro-specimen.
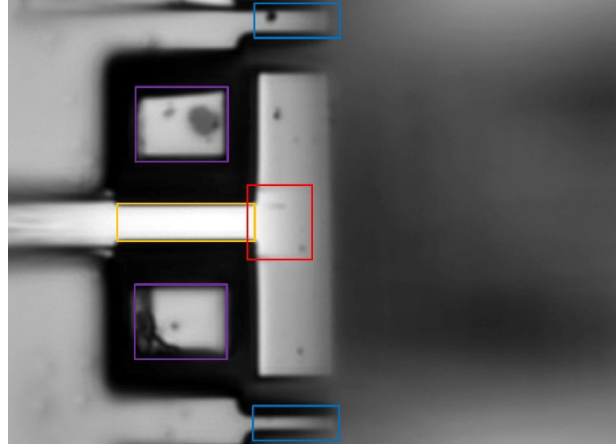
Figure 3.7 Displacement measurement using DIC. The total elongation of the specimen gauge (yellow frame) is obtained from the difference in rigid body displacement between the red and blue frame. The purple frames are used to track the displacement of the gripper teeth in order to determine the starting point of loading (Fig. 3.8(b)). FIB-assisted Pt-deposition has been used to create the dots that serve as DIC tracking pattern. Note that this is only needed when the specimens do not have a natural pattern. The length of the specimen gauge section is 9μm.
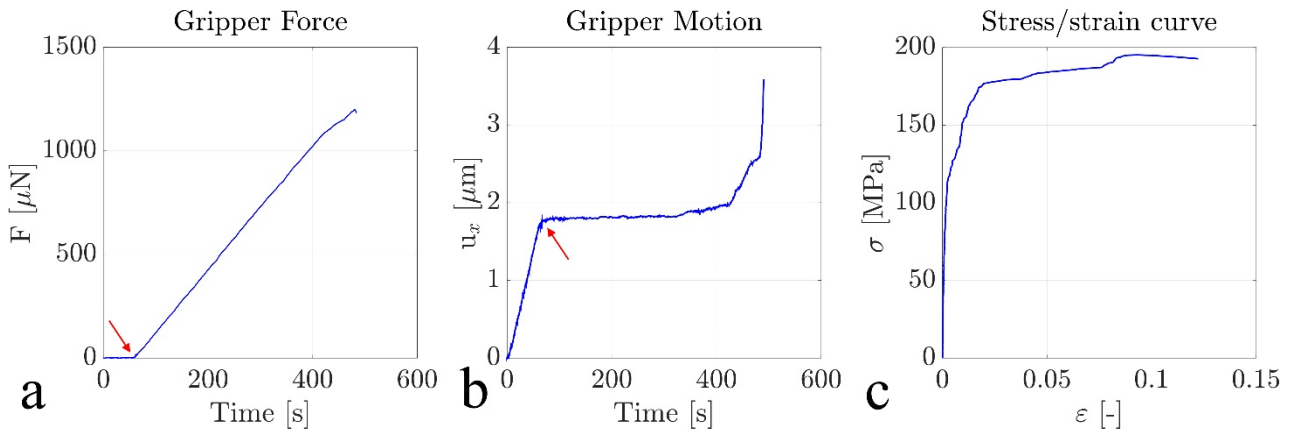
Figure 3.8 (a) Force-time curve and (b) displacement-time curve of the gripper. The points marked by arrows are the transition points in the curves, which indicates the starting moment of loading. (c) Stress-strain curve obtained by combining of (a, b). The noise level of the force measurement, corrected for background influences, is considerably smaller than the applied load in the micro-tensile specimens.

3.3. Proof of principle

3.3.1 Case 1: single phase specimens

As a proof of principle, a set of specimens is fabricated to verify the reliability and accuracy of the test methodology. Fig. 3.9(a) shows three tensile specimens from the same grain on a wedge produced from bulk IF steel. The material was heat treated to increase the grain size such that multiple micro-tensile specimens could be fabricated from a single grain. The high level of parallelism among the tensile specimens reduces the amount of alignment work to only align the first specimen in the series.

The flow curves of the ferrite specimens are shown in Fig. 3.9(b). It is well known from the literature that the variability in the flow curves can be large for micron-sized specimens (even much larger than shown here) [26, 27]. This variability between flow curves is due to large local fluctuations in the density of dislocations, alloying elements and nano-carbides at this small scale. The different plateaus in the flow curves can be due to the different hardening resulted from different interaction of slip systems. However, a detailed slip trace analysis is needed to investigate this further.
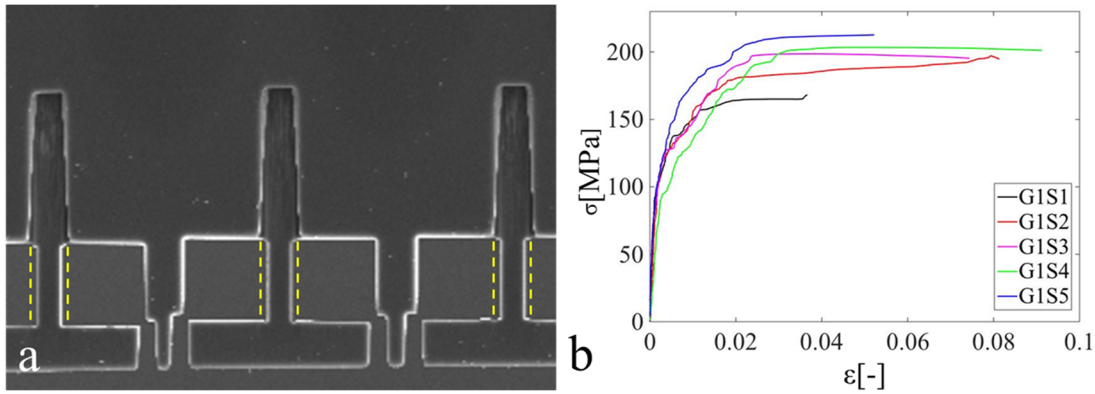

Figure 3.9 An example of 5 parallel micro-specimens from a single ferrite grain. (a) Zoom of 3 specimens, where yellow dashed lines mark the high level of parallelism between the micro-specimens. (b) Stress-strain curves of the 5 ferrite micro-specimens. The initial length of the specimen gauge sections is 9μm.

To this end, secondary electron and back scattered electron images of the specimens after deformation are shown in Fig. 3.10(a-e). The slip systems are marked and identified by the traces on the specimen surfaces. Note that the methodology allows for inspection of all sides of the specimen, as shown in Fig. 3.10(f), to enable a clear identification of slip planes, which is especially useful for cases where the surface traces of different slip systems overlap on the front surface of the specimens. All 5 specimens show the same active slip systems, which demonstrates the overall reproducibility of the methodology for the applied loading, specimen alignment, and micro-specimen geometry. The slip system activation mechanism influenced by the boundary constraint is revealed by this method, as detailed in [28]. This mechanism is hard to observe with macro-mechanical testing because the observed behavior of macro-specimens

is the averaged behavior of huge number of grains. It is also difficult to observe by other micro-mechanical testing methods which have more complicated stress-state of the specimens.
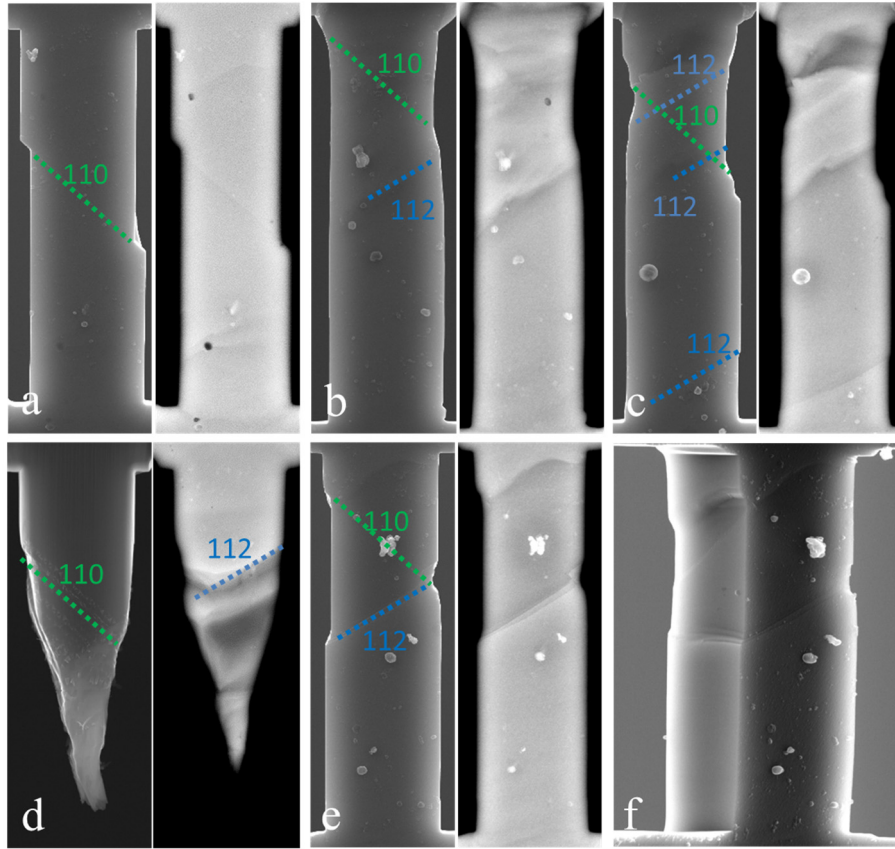
Figure 3.10 (a-e) SE and backscattered electron (BSE) SEM images of the front side of 5 micro-specimens taken from a single ferrite grain. The main slip traces from the {110} and {112} slip families are indicated in the SE images. (f) The methodology allows for inspection of all sides of the micro-specimens to enable a clean identification of slip planes, as demonstrated here by a tilted side view of specimen (e). The initial length of the specimen gauge sections is 9μm.

Of course, it is not a real challenge to isolate a single-crystal specimen from a large-grained bulk material. Yet, the small dimension of the wedge edge used in the current methodology allows for fabrication of single-crystal micro-specimens from multi-phase materials with a realistic microstructure. In Fig. 3.11(a), an example of a ferrite micro-specimen isolated from a dual phase steel sheet is shown, where the martensite islands are still visible, e.g. on the top left of the image. As shown by the inverse pole figure in Fig. 3.11(b), the front and back side shows the same inverse pole figure, which confirms that the specimen gauge part contains only a single ferrite grain, extracted from a multi-phase material.
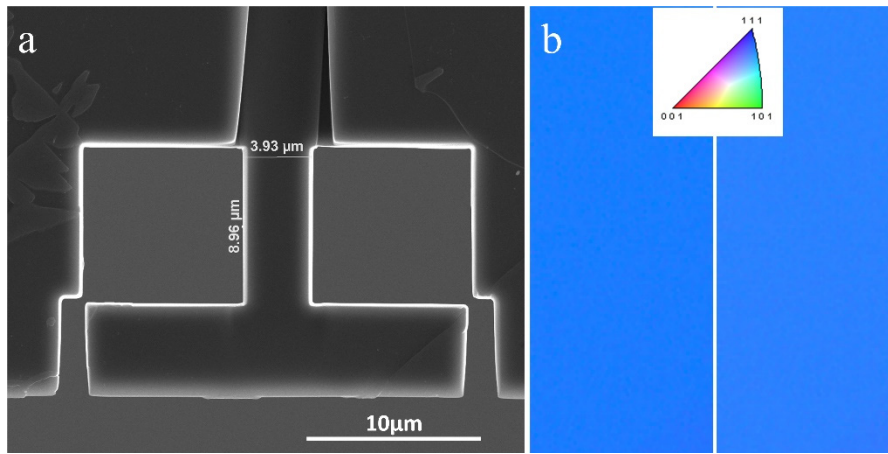
Figure 3.11 (a) SEM micrograph of a ferrite micro-specimen extracted from a DP steel. Martensite islands are visible outside the gauge section. (b) EBSD inverse pole figure map of the front side and backside of the specimen gauge part, which reveals its single crystal nature. The length of the specimen gauge section is 9μm.

3.3.2 Case 2: micro-specimens based on crystallographic orientation selection

This case illustrates lath martensite specimen preparation based on orientation selection. A so-called packet is composed of parallel stacks of laths, which is the fundamental structure unit of lath martensite. These laths can be grouped into sub-blocks and blocks which have a width of micrometers based on the misorientation between them. Therefore, the proposed methodology allows to reveal the effect of the sub-block and block boundaries on the strength of lath martensite.

To obtain the correct boundary configuration in the specimen gauge part, it is required to fabricate specimens from a site-specific region of martensite based on prior EBSD analysis. In the ideal case, a constant boundary through the thickness of the specimen gauge section is preferred, which means inclinations of boundaries in 3D within the specimen are demanded. The selection of the specimen fabrication sites can be based on (1) the pole figures obtained by the EBSD measurement (The martensite lath boundary is approximately parallel to the {110} planes of martensite. Therefore, the {110} pole figures can be used to judge if the boundary is perpendicular to the front plane of the specimen.) and (2) the evaluation of the EBSD inverse pole figure maps from the front and the back sides of the specimen gauge part.

Two configurations of boundary orientations are shown, where (1) the lath boundary is perpendicular to the surface of the specimen, and also parallel to the loading direction (Fig. 3.12(a)) and (2) the lath boundary is perpendicular to the surface of the specimen, but with an angle of 45° to the loading direction (Fig. 3.12(b)). The projection points marked in red circles on the periphery of the equatorial plane of the pole figures (Fig. 3.12(a5, b5)) indicate that the corresponding (110) plane is constant in the thickness direction of the specimen gauge part. A confirmation of this observation is given by the EBSD map of the backside of the specimens in Fig. 3.12(a3,b3). The SEM images of the two specimens before and after deformation are shown in Fig. 3.12(a1,4) and Fig. 3.12(b1,4) respectively.
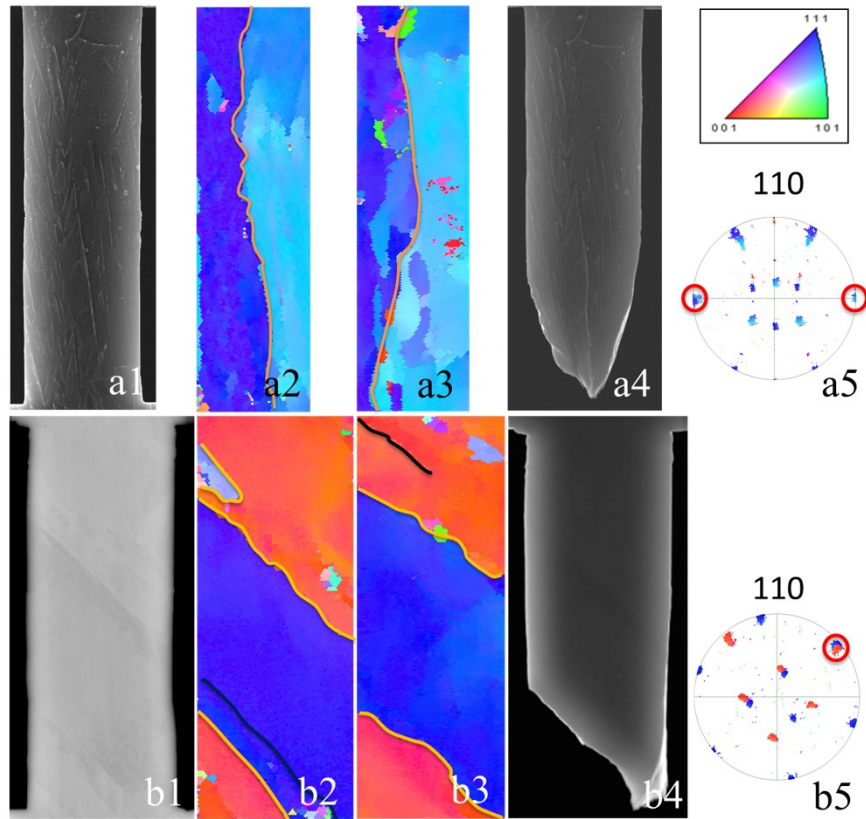
Figure 3.12 Examples of selection of micro-specimens based on orientations of the laths. The SEM images of the specimens before deformation (a1, b1) and after deformation (a4, b4) of the front side are presented. The lath boundary of specimen a is parallel to the loading direction, which is the vertical direction here, whereas the lath boundaries of specimen b is roughly 45◦ tilted with respect to the loading direction. Due to the fact that the boundaries are roughly parallel to the {110} planes of the lath, the projection points in the read circles at the periphery in the {110} pole figure (a5, b5) indicate that the boundary plane of the laths are perpendicular to the specimen surface. This can be confirmed by the EBSD map of the front side and backside of the gauge sections shown in (a2,a3) and (b2,b3). Note that the backside maps are flipped horizontally. The initial length of the specimen gauge section is 9μm.

Based on these micro-tensile tests, two new micro-mechanisms of lath martensite are demonstrated: (1) in contrast to earlier reports in the literature relying on indirect measurements, sub-block boundary strengthening is (almost) equally important as block boundary strengthening [29], and (2) under favorable orientation, all lath martensite sub-structure boundaries can exhibit boundary sliding, which competes with crystallographic slips as the primary deformation mechanism [30]. The identification of these micro-mechanisms is only possible because the used methodology allows for crystallographic orientation specimen selection, combined with front and backside EBSD mapping of the microstructure.

3.4 Conclusions

A reliable and reproducible micro-tensile test is proposed, designed and demonstrated with examples of single phase and multi-phase materials together with region selection based on

EBSD measurement. We have shown that:

(1) The wedge concept allows fabrication of multiple parallel micro-tensile specimens from a single wedge. With this concept, it is easy to handle micro-tensile specimens and the amount of alignment work is significantly reduced.

(2) A site-specific specimen fabrication method is established for micro-tensile specimen preparation from bulk materials, which is applicable to both single-phase materials and multiphase materials with possibility to select regions for specimens based on crystallographic orientations or morphologies.

(3) A setup for micro-tensile testing is constructed with accurate specimen alignment, force and displacement measurement. The setup is adapted for in-situ testing to obtain a clean observation of the specimen surfaces in the complete experiment.

(4) This testing setup is able to reveal mechanisms that are difficult to identify with macro-mechanical testing. Due to the simple loading condition, the analysis of observations is more straightforward compared to other micro-mechanical tests with more complex loading conditions.

References

[1] M.J. Santofimia, C. Kwakernaak, W.G. Sloof, L. Zhao, J. Sietsma, Experimental study of the distribution of alloying elements after the formation of epitaxial ferrite upon cooling in a low-carbon steel, Materials Characterization, 61 (2010) 937-942.

[2} P. Franciosi, L.T. Le, G. Monnet, C. Kahloun, M.H. Chavanne, Investigation of slip system activity in iron at room temperature by SEM and AFM in-situ tensile and compression tests of iron single crystals, International Journal of Plasticity, 65 (2015) 226-249.

[3] J.R. Greer. J.T.M. De Hosson, Plasticity in small-sized metallic systems: intrinsic versus extrinsic size effect, Progress in Materials Science, 56 (2011) 654-724.

[4] O.V. Kuzmin, Y.T. Pei, C.Q. Chen, J.T.M. De Hosson, Intrinsic and extrinsic size effects in the deformation of metallic glass nanopillars, Acta Materialia, 60 (2012) 889-898.

[5] G. Krauss, Martensite in steel: strength and structure, Materials Science and Engineering A, 273-275 (1999) 40-57.

[6] S. Morito, H. Yoshida, T. Maki, X. Huang, Effect of block size on the strength of lath martensite in low carbon steels, Materials Science and Engineering A, 438-440 (2006) 237-240.

[7] C. Zhang, Q. Wang, J. Ren, R. Li, M. Wang, F. Zhang, K. Sun, Effect of martensitic morphology on mechanical properties of an as-quenched and tempered 25CrMo48V steel, Materials Science and Engineering A, 534 (2012) 339-346.

[8] A. Shibata, T. Nagoshi, M. Sone, S. Morito, Y. Higo, Evaluation of the block boundary and sub-block boundary strengths of ferrous lath martensite using a micro-bending test, Materials Science and Engineering A, 527 (2010) 7538-7544.

[9] A. Shibata, T. Nagoshi, M. Sone, S. Morito, Y. Higo, Micromechanical characterization of deformation behavior in ferrous lath martensite, Journal of Alloys and Compounds, 577 (2013) 555-558.

[10] D. Liu, Y. He, X. Tang, H. Ding, P. Hu, P. Cao, Size effects in the torsion of microscale copper wires: experiment and analysis, Scripta Materialia, 66 (2012) 406-409.

[11] M. Delince, P.J. Jacques, T. Pardoen, Separation of size-dependent strengthening contributions in fine-grained Dual Phase steels by nanoindentation, Acta Materialia, 54 (2006) 3395-3404.

[12] C.C. Tasan, J.P.M. Hoefnagels, M.G.D. Geers, A critical assessment of indentation-based ductile damage quantification, Acta Materialia, 57 (2009) 4957-4966.

[13] H. Jirkova, B. Masek, M.F.X. Wagner, D. Langmajerova, L. Kucerova, R. Treml, P. Kiener, Influence of metastable retained austenite on macro and micromechanical properties of steel processed by the Q&P process, Journal of Alloys and Compounds, 615 (2014) 163-168.

[14] N. Kheradmand, H. Vehoff, A. Barnoush, An insight into the role of the grain boundary in plastic deformation by means of a bicrystalline pillar compression test and atomistic simulation, Acta Materialia, 61 (2013) 7454-7465.

[15] M.S. Duesbery, V. Vitek, Plastic anisotropy in BCC transition metals, Acta Materialia, 46 (1998) 1481-1492.

[16] O.V. Kuzmin, Y.T. Pei, J.T.M. De Hosson, Nanopillar fabrication with focused ion beam milling, Microscopy and Microanalysis, 20 (2014) 1581-1584.

[17] W. Kang, J.H. Han, M.T.A. Saif, A novel method for in situ uniaxial tests at micro/nanoscale-part 2: experiment, Journal of Microelectromechanical Systems, 19 (2010) 1322-1330.

[18] D. Kiener, W. Grosinger, G. Dehm, R. Pippan, A further step towards an understanding of size-dependent crystal plasticity: in situ tension experiments of miniaturized single-crystal

copper specimens, Acta Materialia, 56 (2008) 580-592.

[19] J. Yu, J. Liu, J. Zhang, J. Wu, TEM investigation of FIB induced damages in preparation of metal material TEM specimens by FIB, Materials Letters, 60 (2006) 206-209.

[20] M. Ando, H. Tanigawa, S. Jitsukawa, T. Sawai, Y. Katoh, A. Kohyama, K. Nakamura, H. Taheuchi, Evaluation of hardening behavior of ion irradiated reduced activation ferritic/ martensitic steel by an ultra-micro-indentation technique, Journal of Nuclear Materials, 307-311 (2002) 260-265.

[21] J.P. McCaffrey, M.W. Phaneuf, L.D. Madsen, Surface damage formation during ion-beam thinning of samples for transmission electron microscopy, Ultramicroscopy, 87 (2001) 97-104.

[22] Z. Wang, T. Kato, T. Hirayama, N. Kato, K. Sasaki, H. Saka, Surface damage induced by focused-ion-beam milling in a Si/Si p-n junction cross-sectional specimen, Applied Surface Science, 241 (2005) 80-86.

[23] D. Kiener, C. Motz, M. Rester, M. Jenko, G. Dehm, FIB damage of Cu and possible consequences for miniaturized mechanical tests, Materials Science and Engineering A, 459 (2007) 262-272.

[24] L.I.J.C. Bergers, J.P.M. Hoefnagels, M.G.D. Geers, On-wafer time-dependent nano-tensile testing, Journal of Physics D: Applied Physics, (2014) 47.

[25] L.I.J.C. Bergers, J.P.M. Hoefnagels, M.G.D. Geers, Characterization of time-dependent anelastic microbeam bending mechanics, Journal of Physics D: Applied Physics, 47 (2014) 355306.

[26] J.R. Greer, W.C. Oliver, W.D. Nix, Size dependence of mechanical properties of gold at the micron scale in the absence of strain gradients, Acta Materialia, 53 (2005) 1821-1830.

[27] H. Ghassemi-Armaki, R. Maass, S.P. Bhat, S. Sriram, J.R. Greer, K.S. Kumar, Deformation response of ferrite and martensite in a dual-phase steel, Acta Materialia, 62 (2014) 197-211.

[28] C. Du, J.P.M. Hoefnagels, M.G.D. Geers, Ferrite slip system activation investigated by uniaxial micro-tensile tests, in preparation (2016).

[29] C. Du, J.P.M. Hoefnagels, M.G.D. Geers, Block and sub-block boundary strengthening in lath martensite, Scripta Materialia, 116 (2016) 117-121.

[30] C. Du, J.P.M. Hoefnagels, M.G.D. Geers, Plasticity of lath martensite by sliding of substructure boundaries, Scripta Materialia, 120 (2016) 37-40.

Chapter 4. Ferrite slip system activation investigated by uniaxial micro-tensile tests[1]

Abstract

Well-defined uniaxial micro-tensile tests are performed on single-crystal ferrite specimens with three different orientations. All specimens reveal a highly reproducible plastic behavior. The {110}<111> and {112}<111> slip systems equally contribute to the deformation, while all other (complex) slip traces can be identified as cross-slip and 'pencil glide'. No {123}<111> slip system traces were observed. The critical resolved shear stresses of the two active slip systems are close to each other, i.e. $CRSS_{\{110\}} = (1.0\pm0.1)\times CRSS_{\{112\}}$. In all the tested specimens, the activation of the primary slip systems (e.g. systems that activate first) follows the conventional Schmid's law. At first glance, the activation of secondary slip systems does not seem to comply with the highest Schmid factor. However, detailed investigation reveals that the boundary constraints acting on the primary slip system triggers an increase of the Schmid factors of the activated secondary slip systems, i.e. Schmid's law correctly justified all observed slip traces.

4.1 Introduction

The plasticity of ferrite, iron with Body-Centered-Cubic (BCC) structure, is considerably more complex than plasticity in its Face-Centered-Cubic (FCC) counterpart austenite. As in most BCC transition metals, ferrite plasticity is governed by glide of screw dislocations, which are not confined to a well-defined glide plane. Moreover, due the non-close packed nature of the BCC lattice, there is more than one candidate slip family. As a consequence, plastic deformation results in wavy and curved slip traces, which make the identification of the exact slip systems challenging [1,2].

The identification of active slip systems in ferrite remains an important topic which governs the fundamental role of ferrite in providing ductility to many technologically relevant high strength steels. Let us consider a number of investigations in the literature of iron and ferrite plasticity that were conducted at room temperature, since this is most relevant from an application point of view. Since the 1950's, single crystal silicon iron (with ~3wt% Si) has been extensively studied, however, seemingly contradictory results on slip system activity were reported: cases were found where only the {110}<111> family is active [3,4], or where only {112}<111> slip system activity was observed [5], or where slip occurred for both the {110}<111> and {112}<111> family [6,7]. Contradictory results were also reported for single crystal iron, as simultaneous activation of all three families ({110}, {112} and {123}) was observed in torsion fatigue tests [8], whereas tensile tests did not show activation of the {123}<111> slip systems [9,10]. Activation of the {110}<111> and {112}<111> slip systems was also reported for tensile

---

tests on 0.16%Ti ferrite [11]. Besides the identification of operative slip systems, efforts were carried out to quantify the critical resolved shear stress (CRSS). For 3% silicon iron, a 5% higher CRSS for {112}<111> slip on the anti-twinning direction was reported compared to the twinning direction [6]. For pure iron, it was reported that the CRSS of {110}<111> and {112}<111> are similar for slip in the twinning direction but the CRSS for {112}<111> slip in the anti-twinning direction is higher [10]. These reports, however, contradict literature stating that the CRSS of {112}<111> is lower than that of the {110}<111> family [5,7].

All these investigations above were carried out on macro-scale sized specimens and thus based on the overall response of a huge amount of dislocation movements, dislocation interactions, and/or cross-slip events. Unlike the conventional tests, micro-scale testing has the advantage of isolating the influence of complex, multiple cross-slip phenomena providing stress-strain curves that describe dislocation glide on a small number of slip planes only. For example, in micro-pillar compression testing of ferrite, a clean stress state can result in multiple parallel surface traces of the slip systems [12-15]. Yet, while some micro-compression tests revealed slip system activity in all three ({110}, {112} and {123}) families [12,13], other tests only showed activity of the {110}<111> family [14,15], whereas in-situ TEM analysis suggested that the observed {112}<111> traces are in fact composed of alternating short {110}<111> segments [16]. Therefore, uncertainties regarding slip system activation in ferrite persist. Compared to micro-pillar compression, micro-tensile testing may have the advantage of providing a better-defined uni-axial loading state, potentially providing more insights in the relation between surface slip traces and plasticity activation. Moreover, due to the compression-tension asymmetry of BCC materials, the use of tensile loading is indispensable to obtain a complete understanding of ferrite's slip system activation.

The many contradictions in the literature regarding the role of the three slip families in ferrite may be caused by the following physical phenomena: 1) non-unique dislocation glide planes; 2) temperature-dependent and alloying elements-sensitive deformation; 3) tension-compression asymmetry and 4) break-down of Schmid's law [1,17,18]. In general, for FCC metals and Hexagonal Close Packed (HCP) metals, slip system activation is determined by Schmid's law, e.g. the slip system with the highest resolved shear stress is the first one to activate. BCC metals, however, do not always follow Schmid's law, which was found soon after the law was proposed [19] and reviews of cases of violation can be found in [20-22]. Theoretical calculations showed a dependency of the CRSS of the three BCC slip families on the crystal orientation to the loading direction [7]. Atomistic simulations helped to understand other aspects of the anomalous plastic behavior of BCC metals. It was argued that the sensitivity of the Peierls stress to non-glide components of the applied stress is due to a small fraction of edge components in the screw dislocation core [22]. Moreover, it was shown that the glide of 1/2[111] screw dislocations in BCC metals does not only depend on the shear stress in the slip plane but also on the shear stress in the other planes of the same family that share the same [111] zone [23]. In all, the mechanical tests of single crystal BCC metals, covering a wide range of BCC metals and different ways of mechanical testing [21, 24-27], have contributed greatly to the understanding of the abnormal slip activity in BCC metals. Micro-tensile tests on single crystal

ferrite should form a valuable addition to this body of literature.

In this study, we perform a series of uniaxial micro-scale tensile tests on single crystal ferrite micro-specimens by employing a highly accurate nano-force tensile tester to quantify the slip activity at the micro scale, while simultaneously acquiring the specimen's stress-strain response. Crystal plasticity simulations of the tested micro-specimens are used to study the influence of the experimental boundary conditions. The focus will be on the identification of the active slip systems and the investigation of the order in which different slip systems are being activated and the role of boundary constraints therein. It will be shown that the activation of slip systems, either from the {110}<111> or {112}<111> family, is controlled by the interaction between slip system directions and active boundary constraints.

4.2 Material and experiments

A heat-treated IF steel (C0.002-Si0.003-Ti0.03-Nb0.008-Al0.015-Mn0.09 in wt%, N28ppm) is used in this study to obtain large grains by homogenizing at 1000 °C for 7 hours in a vacuum furnace, which allows fabrication of multiple micro-scale specimens extracted from the same grain.

The material is cut into pieces of 11×9×1 mm^3, which are grinded and polished into wedges. Electro-chemical polishing is applied to remove the deformed layers of the wedge resulting from the previous grinding and polishing steps. Previous work has shown that this procedure yields a deformation-free wedge [28]. Figure 4.1(a) is an example of an electron backscattered diffraction (EBSD) measurement of the tip region of a wedge from IF steel with large grains after heat treatment. The thickness at the edge of this wedge is thin enough to allow milling of micro-sized tensile specimens by Focused Ion Beam (FIB). In the finishing steps of all the faces of the specimens, a low beam current (0.3nA) is used with the beam parallel to the finishing surfaces to minimize FIB-induced defects of the micro-tensile specimens. The gauge part of a specimen is 9 μm in length with a cross section of 3×2 μm^2. Because of the large grain size, multiple parallel micro-tensile specimens are produced from a single grain of IF steel. Figure. 4.1(b) shows 3 parallel micro-tensile specimens on the wedge edge.

The crystallographic orientations of the specimens are measured by a EBSD system (EDAX) equipped on a Sirion scanning electron microscope (SEM) from FEI. In this study, single crystal ferrite specimens from three differently oriented grains are tested, the loading direction with respect to the crystal coordinate is marked in the {100} inverse pole figure in Fig. 4.1(c).

The micro-tensile test is conducted with a dedicated nano-force uniaxial tensile tester, which is characterized by a high accuracy in specimen alignment (<0.1 mrad angular alignment and near-perfect co-linearity), force (from 0.07 μN to 250 mN), and displacement (<6 nm reproducibility) measurement [29]. The force measurement is based on the elastic deflection of a calibrated TiAlV leaf spring. The deformation of the specimen is measured with Digital Image Correlation (DIC). Figure 4.2 shows the principle of the tensile testing together with the micro-tensile test machine. The details about the tensile test machine, specimen fabrication, specimen alignment, force and displacement measurement and the tensile test procedure are reported in

[28,29]. The tensile stage is placed under an optical microscope, which records images of the specimens during the deformation. The strain rate of the tensile test is approximately 10^{-4} s-1. In this study, the loading is interrupted immediately after appearance of slip bands on the specimen surface, i.e. before severe deformation occurs. This enables a clear analysis of surface traces of slip systems and therefore a more straightforward identification.
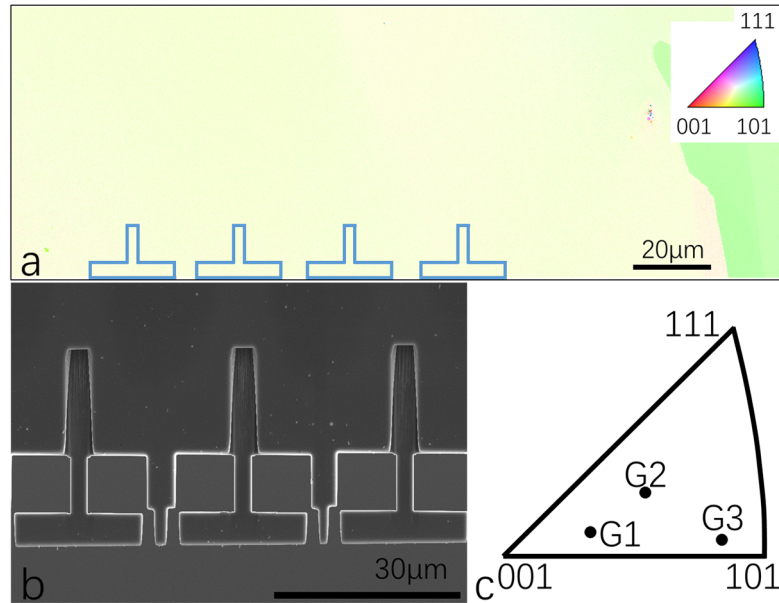
Figure 4.1 (a) EBSD measurement of a wedge of heat-treated IF steel with large grains. One grain boundary is visible on the right. The sketch on top indicates the location of a group of micro-tensile specimens in the wedge. (b) SEM image from 3 parallel micro-tensile specimens fabricated from the same ferrite grain. (c) {100} inverse pole figure showing the loading direction relative to the crystallographic orientation. In this study, single ferrite specimens from three grains with different orientations are tested, which are marked with G1, G2 and G3 respectively.

4.3 Results and discussion

In total 12 specimens, extracted from 3 distinct ferrite grains, are tested. The results of the tensile tests are presented with the stress-strain curves for each of the grains in Fig. 4.3. The specimens taken from the same grains are ordered with increasing tensile strength. The SEM images of the deformed specimens are shown in Fig. 4.4. The dashed lines marked in color in the secondary electron (SE) images indicate the observed slip traces on the surface, while the backscattered electron (BSE) images are left blank for better visibility of the corresponding traces. Red lines mark the primary slip system(s) that activate(s) first, orange lines mark the secondary slip system(s). Black lines represent the trace of a slip plane that does not belong to the {110} or {112} planes. The white curved trace is believed to be the 'pencil glide' phenomenon. The first observation from Fig. 4.4 is that specimens extracted from the same grains show a reproducible slip activity, with the main active slip systems always being the same. This demonstrates a high accuracy and reproducibility of the micro-tensile test methodology,

including specimen fabrication, alignment, load application, etc.
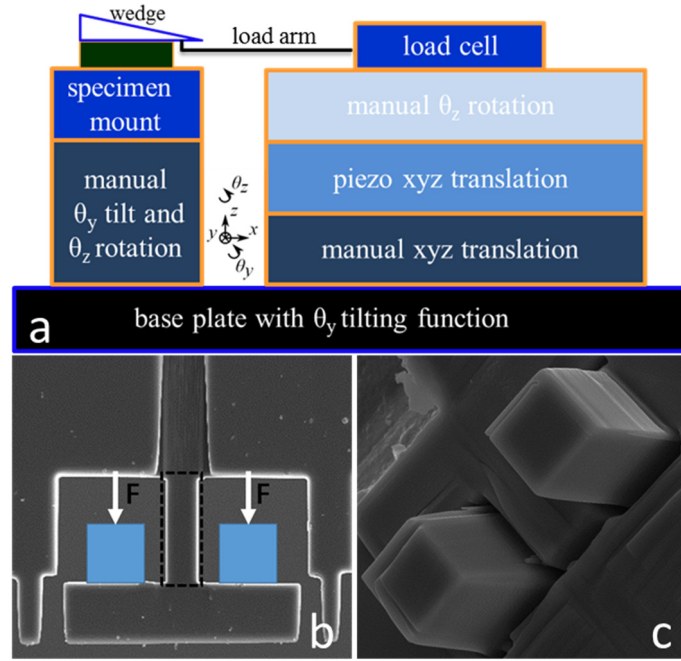
Figure 4.2 Nano-force uniaxial tensile stage and the applied loading of the specimens. (a) Schematic drawing of the tensile stage. The left module of the tensile stage is for specimen mounting, on top of which a wedge is mounted. The micro-tensile specimens, located at the tip of the wedge, are loaded by a loading arm that is connected to the load cell on the right module of the tensile stage. (b) SEM picture of the micro-tensile specimen. The two blue blocks represent the loading pins of the gripper, which are shown in (c). The (9×3×2 μm³) gauge part of the specimen is indicated by the black dashed frame.
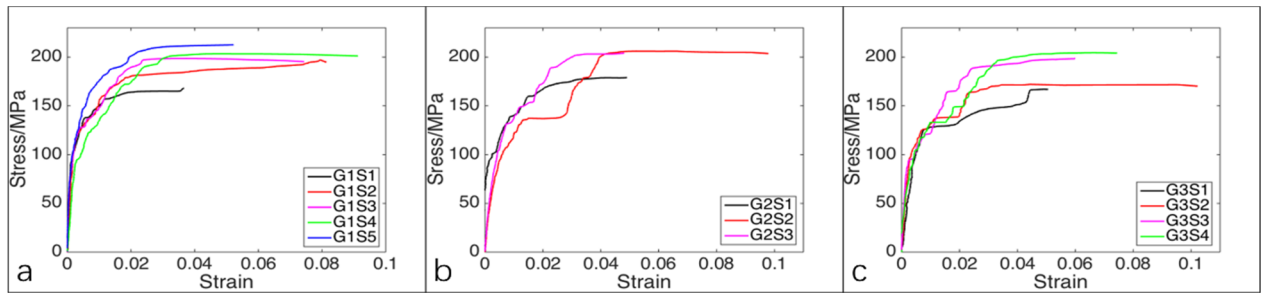
Figure 4.3 (a-c) Engineering stress-strain curves of the micro-tensile specimens extracted from grains 1-3, respectively. The micro-specimens in each grain are ordered with increasing strength. G1S1 refers to Specimen 1 from Grain 1.

Before considering the specific slip activity of each specimen, it should be noted that all tests can be divided in two groups based on whether the cross bar was constrained in the horizontal direction or not, as can be seen from the vertical white dash-dotted lines next to the SE image of each specimen (Fig. 4.4). These two cases correspond to an unconstrained (UB) and constrained (CB) boundary condition. The difference in boundary condition, even though each

experimental test was executed exactly the same, is attributed to (horizontal) slip between the two load pins of the gripper and the specimen crossbar. Which of the two boundary conditions becomes effective in a test appears to be quite unpredictable, but it has a clear impact on the activated slip systems. As can be seen in Fig. 4.4, for the UB specimens (G1S1, G2S1, G3S1, and G3S2) only one or two primary slip systems (red lines) are activated, which not only elongates the specimen in the vertical loading direction but also shears it in the horizontal direction. The slip systems of CB samples (the remaining specimens) are more complicated in the sense that, in additional to one or two primary slip system(s), one or two secondary slip systems (orange lines) are activated, which consistently shear the gauge section in opposite horizontal direction than the primary slip system(s) to comply to the constraint vertical motion of the crossbar.

4.3.1 Strength of the specimens

It is well known that a precise yield point is difficult to determine in small-scale testing due to the large influence of a random distribution in initial dislocations, alloy elements, nano-precipitates, etc. [31]. Here, the average yield stress of all 12 tests of the three grains is estimated to be (110±40) MPa while the tensile strength of the specimens lies between 150 and 220 MPa. The micro-pillar tests in Refs. [12,13] revealed a higher tensile strength, which is largely due to the lower alloying elements content in the IF steel compared to the dual phase steel ferrite in Ref. [12] and the duplex steel ferrite in Ref. [13]. The measured range of yield and tensile strength values in the present analysis correspond to those of the pure iron macro-sized samples in Ref. [10]. In Fig.4.3, no clear difference can be observed for the degree of hardening of the 3 grains due to their different crystal orientation (Fig. 4.1(c)). In contrast, in Ref. [10] the hardening clearly changes for different crystal orientations. This is attributed to the larger sample size ($11 \times 2 \times 2$ mm^3) whereby plasticity in macro-sized specimens entails a huge amount of dislocations, triggering intensive interactions between slip systems.

The strength of the individual specimens is closely related to the activation of (one or more) secondary slip systems. The UB specimens (G1S1, G2S1, G3S1, G3S2), which deform by dislocation glide on primary slip system(s) only, exhibit the weakest stress-strain response(s) for each grain, with a maximum tensile strength of 180 MPa. In these samples, all glide planes are (roughly) aligned, resulting in little or no dislocation interaction, which also holds for the UB specimens of Grain 3 with two primary slip systems. The CB specimens with a straight deformed gauge section accommodated by slip on secondary slip system(s), reveal a stronger stress-strain response, with a minimum tensile strength of 200 MPa. The secondary slip system(s) have to shear the specimen in horizontal direction that is opposite to the primary slip system(s), and hence the primary and secondary slip planes have to cross each other. The resulting dislocation interactions explain the higher tensile strength. Interactions of primary and secondary slip planes, specifically disruptions in the primary slip plane due to subsequent slip on a secondary slip plane, are clearly visible in G1S5, G2S3, and G3S4, exhibiting the highest tensile strength for each grain. This hardening difference between single and multiple slip agrees with observations in Ref. [32] that single slip micro-pillars are weaker than multiple slip ones. It will be shown below that this boundary constraint also plays an important role in the

activation of the slip systems.
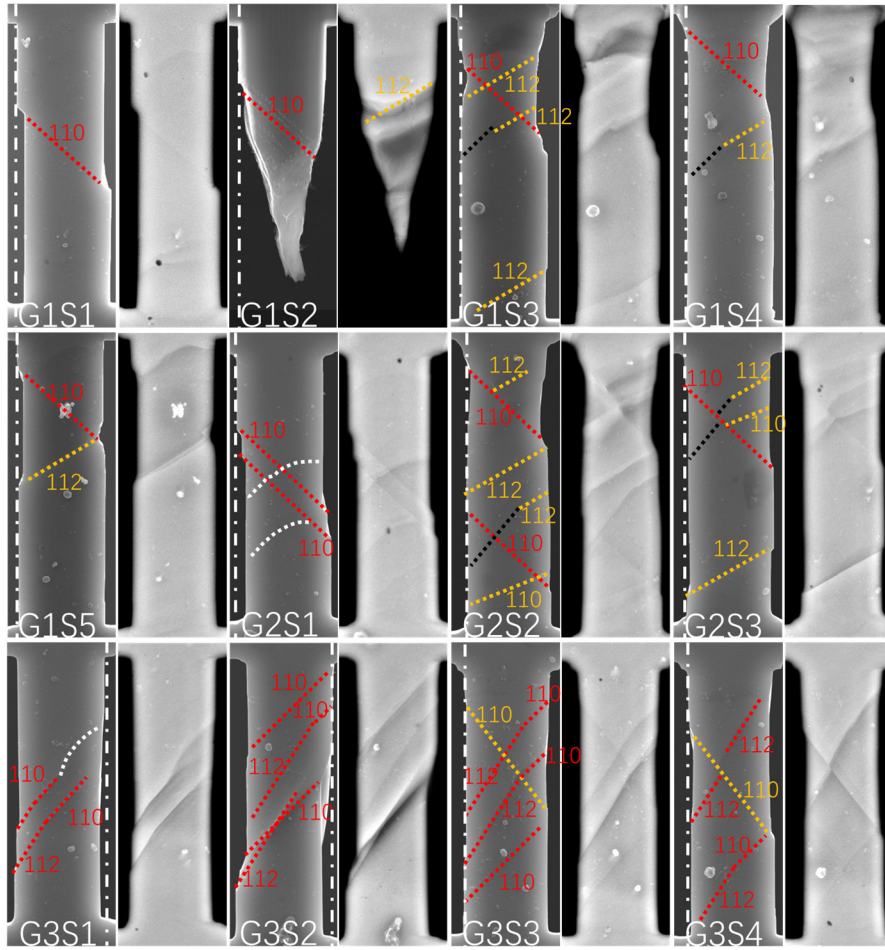
Figure 4.4 Front side SE and BSE images of deformed specimen gauge section. G1S1 refers to Specimen 1 from Grain 1. The slip traces are marked with colors: red represents the primary slip system(s) which is/are activated first, orange the secondary slip system(s). Black lines represent the trace of a slip plane that does not belong to the {110}<111> or {112<111>} families. The white curved trace is believed to be the 'pencil glide' phenomenon [19,30]. The vertical dash-dotted lines at either the left or right edge of each SE image help to visualize the shape of the deformed specimens: 'sheared' or 'straight', which corresponds to an unconstrained (UB) and constrained (CB) boundary condition. Note that there are two secondary systems in Grain 2 and two primary systems in Grain 3, both of which are only slightly misoriented relative to each other. G1S2 is the only specimen loaded to fracture for which the left SE image shows the backside, for which the {110}<111> slip trace is more clearly visible.

The initial state of the specimen, defining the local statistical and spatial variation in dislocation and nano-precipitates density constitutes an intrinsic reason for the fact that specimens from the same grain show a different plastic behavior. Figure 4.5 is a bright field TEM image of the heat-treated ferrite material in the undeformed state, which shows the 'clean' state of the ferrite crystals, with a sharp grain boundary and a relatively low number of defects. The distribution of these defects, i.e. dislocations and nano-precipitates, show a strong spatial variability, with

large regions of more and less defects. The averaged nano-particle density is $\sim$30 μm^{-3} with an average size of $\sim$40 nm, yielding an average distance between nano-particles of $\sim$300 nm. The dislocation density of the initial material is measured to be $\sim$7$\times$10^{11} m^{-2}. Even when considering the escape of dislocations from a TEM sample and the invisibility of some dislocations in TEM bright field imaging [33], the total number of dislocations per micro-specimen is expected to be less than 100. For a typical specimen elongation of 0.5 μm, however, approximately 3000 dislocations are required. Therefore, most dislocations must have been generated during the deformation process. Considering that the micro-specimens do not contain grain or phase boundaries, the nucleation of dislocations is most logically attributed to Frank-Read dislocation sources that are pinned to the nano-precipitates. Based on the calculation of the Frank-Read dislocation source model [34], and using the measured yield stress of $\sim$110 MPa, the distance between the pinning points of a typical dislocation line is calculated to be $\sim$1 μm. This distance is relatively large compared to the micro-specimen dimensions. Moreover, the chance of finding two nano-precipitates on the same glide plane of a slip system with a high Schmid factor is rather small. This scarcity of dislocation sources can explain why, for the micro-specimens in Fig. 4.4, slip activity is concentrated to only 1 or 2 parallel glide planes of the active slip system (e.g. G1S1 or G2S1), which suggests that only these planes from the corresponding set of parallel glide planes contain a dislocation source. A consequence of the variability in nano-precipitate density would be a corresponding distribution in Frank-Read source length and hence in the critical dislocation nucleation stress, which may explain the differences in yielding and hardening behavior in Fig. 4.3.

4.3.2 Identification of the active slip systems

The theoretical angle between slip traces and the loading direction on the surface of the specimens are calculated using the Euler angles obtained from EBSD measurements. The observed slip traces are compared with potential dislocation traces for all three slip planes ({110}, {112}, and {123}) to identify the specific slip system. In each of the 3 grains in Fig. 4.4, activity in the {110}<111> and {112}<111> slip systems are observed and the measured slip trace angles adequately match the calculated angles (within the EBSD measurement accuracy in the crystal rotation, $\sim$2 degrees). No active {123}<111> systems can be observed. At room temperature, the CRSS of the {123}<111> family is expected to be (much) higher than that of the {110}<111> and {112}<111> families. In addition, because both the {110}<111> and {112}<111> family are activated as primary slip system in Grain 3, the CRSS of the two active families must be relatively close to each other. Grain 2 shows that both {110}<111> and {112}<111> can also be activated as the secondary slip system, which supports the conclusion that the CRSS of these two slip systems are nearly equal.

The slip systems of the two active families and their Schmid factors in all three grains are listed in Table 4.1. The primary system(s) have the highest Schmid factor of the family, whereas the secondary slip systems, either of the {110}<111> or {112}<111> family, have a much lower Schmid factor in the family. This indicates that activation of secondary slip systems cannot be predicted through a conventional Schmid factor analysis, which is based on the initial specimen

geometry and applied load. In order to analyze the influence of the boundary constraints on the activation of the slip systems with low Schmid factors, the {111} pole figures of the three grains are presented in Fig. 4.6, where each projection point (data point) in the pole figure represents the direction of the corresponding 3D slip vector of (the bottom part of) the specimen gauge section. There are only 4 possible slip direction vectors, because each slip direction is shared by 3 of the 12 {110}<111> systems and 3 of the 12 {112}<111> systems. Note that slip systems with the same slip direction vector can still be uniquely identified from the observed slip traces, i.e. the intersections between the slip plane and the specimen top, bottom, and side surfaces. The arrows between the center of the pole figure and the projection point show the observed in-plane slip direction of the bottom part of the specimen gauge section. The arrows are always pointing downwards towards the positive vertical (A1) direction, which is the direction of loading.
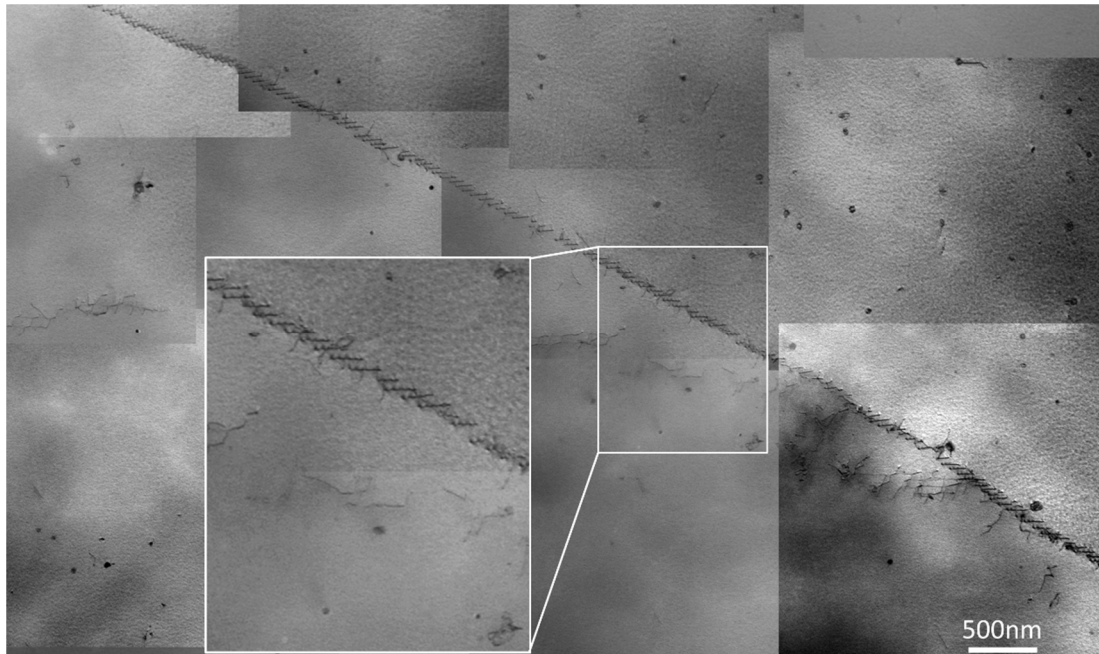
Figure 4.5 TEM bright field image of the undeformed material. A spatial variability in the dislocation and nano-precipitates distribution is observed, triggering the observed spread in the plasticity of the specimens.

For specimens G1S2 – G1S5 of Grain 1, the horizontal displacement introduced by the primary slip system, {110}<111>, is compensated by a second slip system that moves the gauge part in the opposite horizontal direction in order to accommodate the imposed overall deformation of the gauge part. The horizontal movement triggered by primary slip systems induces an opposing elastic shear strain through the imposed horizontal boundary constraints from the clamps, which increases the resolved shear stress of the secondary slip systems that have an horizontal (A2) component with opposite sign compared to the primary slip system, and vice versa. This first criterion rules out the secondary systems with a projection point in the same quadrant in the pole figure as the primary system (marked in red). In addition, the larger the

horizontal component of the secondary slip system the larger the resolved shear stress increase induced by the opposing elastic shear strain and the more efficient will be the secondary slip systems to compensate the horizontal displacement. This also explains why slip systems with a small horizontal component close to the vertical (A1) axis, for example the slip systems with a slip direction marked in blue in Fig. 4.6(a) are not active, although it has a high initial Schmid factor of 0.47. Therefore, the most likely vector is marked in orange in Fig. 4.6(a), which is shared by 3 slip systems from the {112}<111> family and 3 slip systems from the {110}<111> family. Among these slip systems, the one with the highest Schmid factor should be the one that is activated first, which is indeed the active {112}<111> system observed in Grain 1. This is confirmed by Table 4.1, which shows that the active slip system is always the one with the highest Schmid factor among the 6 systems that share the same slip direction. Therefore, the slip system activity in all specimens of Grain 1 is reproducible and predictable.

Table 4.1 The Schmid factors of the {110}<111> and {112}<111> families of the three grains, for the initial specimen geometry and initial loading conditions. The slip systems are grouped by the slip directions, which are separated by thick lines in the table. The active slip systems are in bold and color. The systems marked in red and orange correspond to dislocation traces of, respectively, the primary and secondary slip system(s), marked with the same color in Fig. 4.4 and Fig .4.6. High Schmid factor systems that have not been activated but are discussed in the text are marked in blue.

{110}<111>				{112}<111>			
Slip System	Schmid factor			Slip System	Schmid factor		
	G1	G2	G3		G1	G2	G3
(1-10)[111]	0.26	0.13	0.06	(1-21)[111]	0.12	0.06	0.01
(01-1)[111]	0.05	0.03	0.04	(11-2)[111]	0.21	0.11	0.08
(10-1)[111]	0.31	0.16	0.10	(-211)[111]	0.33	0.17	0.09
(1-10)[11-1]	**0.49**	**0.49**	**0.47**	(-121)[11-1]	0.38	0.45	**0.47**
(011)[11-1]	0.16	0.28	0.35	(2-11)[11-1]	0.47	0.41	0.34
(101)[11-1]	0.33	0.22	0.12	(112)[11-1]	0.09	0.03	0.14
(110)[-111]	**0.47**	0.44	**0.45**	(1-12)[-111]	0.15	0.07	0.12
(01-1)[-111]	0.10	0.15	0.33	(12-1)[-111]	0.33	0.34	0.45
(101)[-111]	0.37	0.28	0.12	(211)[-111]	**0.48**	0.42	0.33
(011)[1-11]	0.11	0.15	0.06	(21-1)[1-11]	**0.38**	**0.31**	0.12
(10-1)[1-11]	0.38	**0.34**	0.14	(-112)[1-11]	0.28	0.29	0.12
(110)[1-11]	0.27	0.19	0.08	(121)[1-11]	0.10	0.02	0.01

In Grain 2, the active slip systems are also reproducible. Exactly the same slip systems in both families repeat themselves in the different specimens, as can be confirmed in Fig. 4.6(b) by the parallel slip traces with the same colors. The primary slip system is the one with the highest Schmid factor, as expected. The activity of the secondary slip systems may, at first glance, be regarded as anomalous as these slip systems have much lower Schmid factors. The pole figure in Fig. 4.6(b) reveals that the activated secondary {110}<111> and {112}<111> slip systems

have the same slip direction, represented by the marked projection points. The slip on the secondary slip systems compensates the horizontal component of the slip on the primary system. These observed secondary slip systems are activated since they belong to the group of 6 slip systems that can accommodate the boundary constraint on the specimen gauge. Hence, the same mechanism of Grain 1 explains the activation of the two secondary slip systems in Grain 2. In this fact, there is no noticeable difference between the two slip families as they are both activated through the loading constraints.
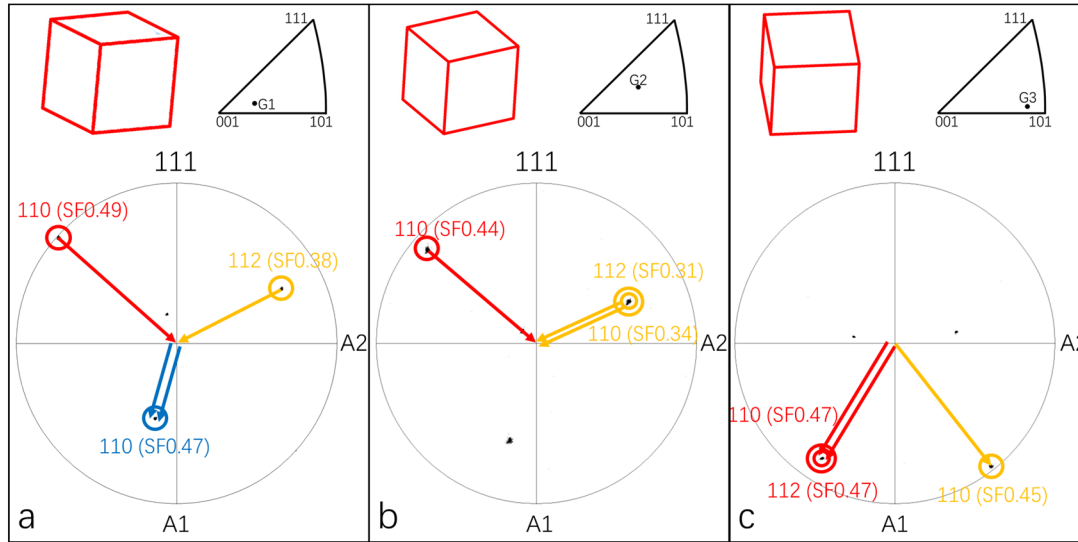
Figure 4.6 (a-c) {111} pole figures of Grain 1-3 respectively, which represent the slip direction of the {110}<111> and {112}<111> systems. The colors correspond to the dislocation traces in Fig. 4.3 and the marked slip systems in Table 4.1. The slip systems marked in red and orange are the observed active slip systems in Fig. 3, with the corresponding Schmid factors given in the brackets. Note that the blue point in (a) is an example illustrating why the corresponding slip systems are not activated, see text. The unit cells indicate the orientations of the grains with respect to the specimen axes respectively (top left figure). The {100} pole figures represent the loading direction with respect to the crystallographic coordinates of the grains respectively.

In Grain 3, two set of primary slip systems are observed, the {110}<111> and {112}<111> system with the highest Schmid factors, which are marked in red in Table 4.1. The {110}<111> system is identified as the secondary slip system, which is marked in orange. The slip directions of these three slip systems are marked in the pole figure in Fig. 4.6(c). G3S3 and G3S4 reveal activation of all these three systems. Specimens G3S1, S2 only activated the primary systems, both of which inducing a horizontal displacement of the lower part of the gauge section to the left in the horizontal direction. Due to the fact that the horizontal displacement by slip of the primary systems can be compensated by the orange {110}<111> secondary system, G3S3, S4 preserve a straight deformed gauge section. Similar to Grain 1 and Grain 2, the activation of the secondary slip system due to the boundary constraint is the governing mechanism.

4.3.3 Crystal plasticity simulations: the effect of boundary constraints

To verify the role of boundary constraints on slip systems activation, we consider the specimens extracted from Grain 3. The specimens are modeled with a standard Crystal Plasticity model (see Appendix for details on the model). Measured Euler Angles are used to define the grain orientation, including the {110}<111> and {112}<111> slip systems. Only the gauge section is modeled, whereby the measured specimen dimensions are assigned.

Two model configurations are considered. To model the unconstrained boundary condition of specimen G3S1 and G3S2, in Configuration 1, the bottom face of the specimen is free to move laterally and to rotate, which is achieved by applying only an average axial displacement from the experiments along the A1 direction to the bottom face. To capture the constrained boundary condition of specimen specimens G3S3 and G3S4, in Configuration 2, the averaged vertical displacement from the experiments along the axial (A1) direction is applied to the bottom face to enforce a straight specimen shape.
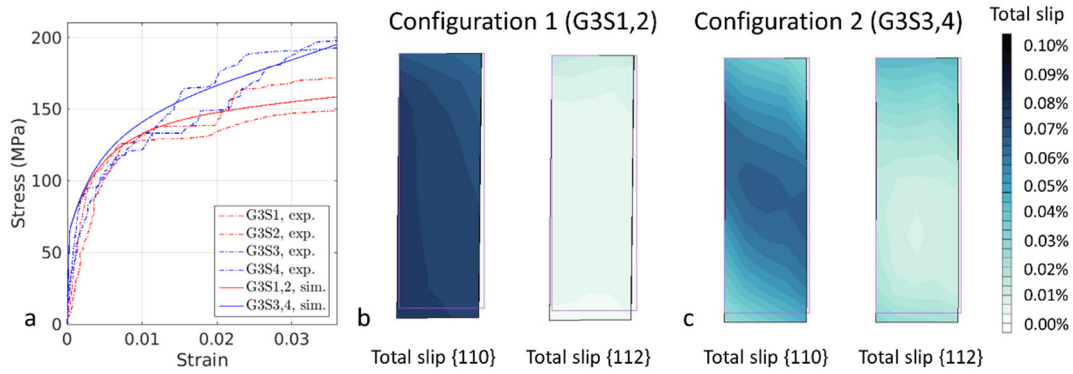
Figure 4.7 (a) stress-strain response of Configuration 1 (G3S1,2) and Configuration 2 (G3S3,4) versus experiments; (b) total slip on {110}<111>, peak value 7.5%, and {112}<111>, peak value 1.6%, for Configuration 1 and (c) total slip on {110}<111>, peak value 6.5%, and {112}<111>, peak value 5%, for Configuration 2.

Model material parameters (CRSS and hardening), reported in Table 4.A.1 (Appendix), have been tuned until the measured ~50 MPa strength difference between the axial stress-strain responses of the two model configurations was reproduced, see Fig. 4.7(a). Note, that the hardening behavior is reproduced only qualitatively, since details of the flow response depend on the unknown specific distribution of dislocations and dislocation sources in the specimens, dislocation interactions and phenomena like cross-slip, that are not included in the adopted Crystal Plasticity model. As a consequence, also the plastic response in terms of slip systems should be interpreted qualitatively. Note that, in both configurations, both {110}<111> and {112}<111> slip systems are active, like in experiments G3S1-4. In Configuration 2 (G3S3, S4) {112}<111> slip is spread almost homogeneously over the specimen, while {110}<111> tends to localize in the position and orientation of the secondary slip systems identified in G3S3, S4. Such slip systems are named "secondary" and hence their activation depends on the active

boundary constraints. Localization of deformation triggered by particular glide planes is not observed in Configuration 1, where both {110}<111> and {112}<111> slip activities are homogeneous throughout the sample. This is consistent with observations in experiments (GS1,2), where more than one slip trace is activated for both slip systems. Simulations, which are analyzed at 3.5% tensile strain, show more {110}<111> slip activity than {112}<111>, suggesting that the former activates earlier than the latter. This cannot be deduced from the micrographs, which are taken at more than 5% strain, where slip activity in the two slip systems seems to be similar.

To summarize the observations so far, slip activity in the three grains are all reproducible in the sense that repeating slip traces are observed in the same grains. The activation of the observed slip systems is predictable based on Schmid's law, but only when taking into account the change of Schmid factors caused by the accommodation of the specimen deformation due to the change of loading state resulting from the applied boundary constraints. This change of Schmid factors upon specimen deformation might be confused with a non-Schmid effect, especially when performing a slip trace analysis in cases where the exact local boundary constraints are not known, e.g., for macro-sized sample or for a grain within in a polycrystalline material.

4.3.4 Calculation of CRSS values

With the present setup of the micro-tensile tests under optical microscopy, accurate determination of the true yield point, i.e. the stress at which the first dislocations start to glide, and thus the CRSS is not feasible. Nevertheless, the activation of the primary and secondary slip systems can be used to obtain the quantitatively assess the relative bounds for the CRSS values of {110}<111> and {112}<111> slip systems. For instance, for Grain 1, the primary slip system that is activated is the (1-10)[11-1] system with a Schmid factor of 0.49, whereas the (211)[-111] system with a Schmid factor of 0.48 has not been activated. Assuming that all slip systems of the {110}<111> family have the same CRSS while the {112}<111> family also has a single CRSS, this means that ratio between resolved shear stress and CRSS is larger for the (1-10)[11-1] slip system than for the (211)[-111] system, yielding the following bound: $CRSS_{\{110\}} < 1.02 \times CRSS_{\{112\}}$. A similar calculation of an upper or lower bounds of the ratio of $CRSS_{\{110\}}$ to $CRSS_{\{112\}}$ was performed for the primary slip system(s) of Grain 2 and 3, and the secondary slip system(s) of Grain 1–3, as graphically represented in a bar plot in Fig. 4.8. Note that the secondary slip systems of Grain 2 and primary slip systems of Grain 3 are atypical in the sense that two slip systems are activated at the same time, yielding simultaneously an upper and lower bound on the ratio, as shown by the single value in Fig. 4.8. All upper or lower bounds on the ratio of $CRSS_{\{110\}}$ to $CRSS_{\{112\}}$ agree with each other within experimental uncertainties, yielding an average ratio of approximately (1.0±0.1), i.e. $CRSS_{\{110\}} = (1.0 \pm 0.1) \times CRSS_{\{112\}}$. In other words, in most cases both slip systems will be activated at room temperature. In bulk polycrystalline ferrite, the grains are adhered to neighboring grains in all directions resulting in more severe boundary constraints, which might explain why most literature studies do see both {110}<111> and {112}<111> slip activity, see Introduction. For crystal plasticity simulations, the CRSS values are often has chosen equal for the {110}<111> and {112}<111> family, either

for convenience or to avoid the many contradictory results in the literature, see e.g. Ref. [35].
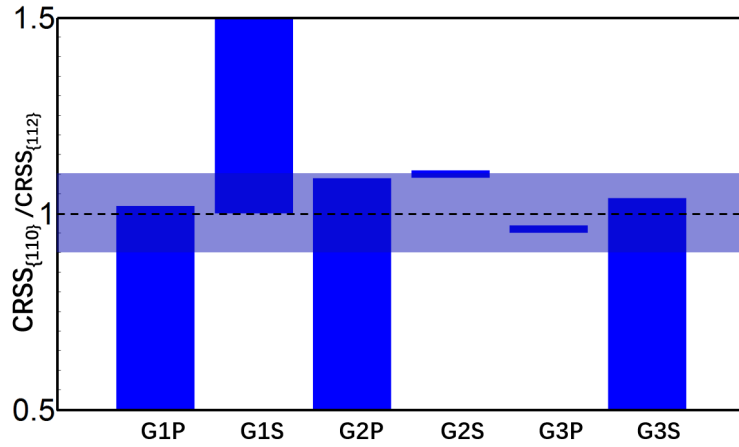
Figure 4.8 Chart presenting the ratio of CRSS{110} over CRSS{112} based on the Schmid factor analysis. This ratio has been determined six times, for both the primary ('p') or secondary ('s') slip system(s) for each of the three grains ('G'). The horizontal dashed line and band corresponds to the estimated average ratio with error margin of $\mathrm{CRSS}_{\{110\}} = (1.0 \pm 0.1) \times \mathrm{CRSS}_{\{112\}}$.

With the obtained understanding of the role of the boundary constraints in the observed flow response, the primary and secondary slip traces in all 12 micro-specimens can be explained. Yet, more complicated slip activity, such as cross-slip, can be observed in Fig. 4.4. Cross-slip is often reported in BCC iron testing, for specimens ranging from in-situ TEM samples [16] to mm-sized single crystals [10]. Cross-slip depends on the Schmid factors of the two slip systems sharing a [111] slip direction [36]. On a more fundamental level, atomistic simulations revealed that cross-slip is caused by a kink pair mechanism, resulted from the <111> screw dislocation core structure [37-39]. In this study, many indications of cross-slip are observed. For instance, all Grain 3 tests show cross-slip between the (1-10)[11-1] and (-121)[11-1] slip system, which share the [11-1] slip direction. For Grain 2, specimens G2S2 and G2S3 also show cross-slip between the (21-1)[1-11] slip system and a non-close-packed atomic plane marked in black in Fig. 4.4. Careful examination of these black traces on the front, bottom and side surface reveals that this is the (143)[1-11] slip system of the {134} family, again sharing the [1-11] slip direction. In addition to cross-slip observations, curved slip traces, indicated by white lines, can be seen in G2S1 and G3S1 in Fig.4.4, which are probably composed of small elementary steps on different glide planes that share the same slip direction, i.e. crystallographic planes of the same [111] zone. [19]. This so-called 'pencil glide' phenomenon has often been observed in literature, e.g. in [30,40], which has been attributed to consecutive cross-slip events, resulting in wavy and curved slip traces in macro-sized specimens, especially when the strain is high, e.g. in [10].

In summary, it is shown that all slip traces in all 12 micro-specimens can be explained by (i) application of the conventional Schmid's law, (ii) taking the role of applied boundary constraints into account for the activation of secondary slip systems, and (iii) and attribution of the remaining, often curved slip traces to cross-slip activity. In other words, none of the reasons

reported in the literature to explain anomalous slip behavior (the non-Schmid effect [20-22], the influence of the shear stress on other planes of the same family than the slip plane [23], the effect of load application on a twinning or anti-twinning plane [6,10], etc.) are needed to explain the details of the here-presented micro-tensile tests. This does not imply that these non-Schmid effects are absent. It does, but their influence is more limited than expected, e.g., limited to a few percent of the CRSS.

4.4 Conclusions

Single crystal ferrite micro-specimens of different orientations were tested with a nano-force tensile stage. Reproducible results within statistics were obtained in all the test orientations. Based on the slip trace and stress-strain analysis of the specimens, the following conclusions are drawn:

(1) Both the {110}<111> and {112}<111> slip systems contribute to the deformation, while {123}<111> family is not activated. For both the {110}<111> and {112}<111> family, the primary slip system or systems were consistently the ones with the highest Schmid factors.

(2) The CRSS of the {110}<111> and {112}<111> slip systems are close to each other and the following ratio has been identified: $\mathrm{CRSS}_{\{110\}} = (1.0 \pm 0.1) \times \mathrm{CRSS}_{\{112\}}$.

(3) Secondary slip systems, i.e. slip systems that activate at later stage during in the deformation are necessary to accommodate the applied boundary constraints. At first glance, these slip systems appear to exhibit anomalous slip activity, as their initial Schmid factor is low. Careful analysis revealed that the actual Schmid factor must be (much) higher due to the increase in resolved shear stress due to the elastic strain caused by the combination of primary slip plasticity and boundary constraints, i.e. Schmid's law is still valid.

(4) Cross-slip and pencil glide account for the remaining, often curved slip traces. As a result, anomalous slip effects, such as the well-known non-Schmid effect, are not needed to explain the observed slip activities and, thus, their possible contribution is expected to be limited.

The identified slip systems complement insight on slip system activation in the ferrite literature. It is essential to take the exact boundary constraints into account in the analysis slip system activation, which could be a complicated task for macro-specimens, micro-specimens under complex loading conditions, or grains within a polycrystalline material.

References

[1] D. Rodney, J. Bonneville, Dislocations, Physical metallurgy, fifth edition, 2 (2014) 1591-1680.

[2] D. Hull, D.J. Bacon, Introduction to dislocations, fifth edition, 2011.

[3] W.R. Hibbard, A study of <112> edge dislocations in bent silicon-iron single crystals, Acta Metallurgica, 4 (1956) 306-315.

[4] F.W. Noble, D. Hull, Deformation of single crystal of iron 3% silicon, Philosophical Magazine, 12 (1965) 777-796.

[5] D.F. Stein, P.D. Gorsuch, Etch pit evidence of (112) slip in iron, Acta Metallurgica, 9 (1961) 904.

[6] T. Taoka, S. Takeuchi, E. Furubayashi, Slip systems and their critical shear stress in 3% silicon iron, Jounal of the Physical Society of Japan, 19 (1964) 701-711.

[7] B. Orlans-Joliet, J.H. Driver, F. Montheillet, Plane strain compression of silicon-iron single crystals, Acta Metallurgica et Materialia, 38 (1990) 581-594.

[8] H.D. Nine, Slip planes and asymmetric slip in fatigue of iron single crystals, Philosophical Magazine, (26) 1972 1409-1418.

[9] W.A. Spitzig, A.S. Keh, The effect of orientation and temperature on the plastic flow properties of iron single crystals, Acta Metallurgica, 18 (1970) 611-622.

[10] P. Franciosi, L.T. Le, G. Monnet, C. Kahloun, M.H. Chavanne, Investigation of slip system activity in iron at room temperature by SEM and AFM in-situ tensile and compression tests of iron single crystals, International Journal of Plasticity, 65 (2015) 226-249.

[11] W.A. Spitzig, The effects of orientation, temperature and strain rate on deformation of Fe-0.16wt.% Ti single crystals, Materials science and engineering, A 12 (1973) 191-202.

[12] H. Ghassemi-Armaki, R. Maass, S.P. Bhat, S. Sriram, J.R. Greer, K.S. Kumar, Deformation response of ferrite and martensite in a dual-phase steel, Acta Materialia 62 (2014) 197-211.

[13] E.Y. Guo, H.X. Xie, S.S. Singh, A. Kirubanandham, T. Jing, N. Chawla, Mechanical characterization of microconstituents in a cast duplex stainless steel by micropillar compression, Materials Science and Engineering A, 598 (2014) 98-105.

[14] B.R.S. Rogne, C. Thaulow, Effect of crystal orientation on the strengthening of iron micro pillars, Materials Science and Engineering A, 621 (2015) 133-142.

[15] B.R.S. Rogne, C. Thaulow, Strengthening mechanisms of iron micropillars, Philosophical Magazine, (95) 2015 1814-1828.

[16] D. Caillard, Kinetics of dislocations in pure Fe. Part I. In situ straining experiments at room temperature, Acta Materialia, 58 (2010) 3493-3503.

[17] E. Pink, Low-temperature softening in body-centered cubic alloys, Progress in Materials Science, 24 (1980) 1-50.

[18] J.R. Greer, J.T.M. de Hosson, Plasticity in small-sized metallic systems: Intrinsic versus extrinsic size effect, Progress in materials science, 56 (2011) 654-724.

[19] G. Taylor, C. Elam, The distortion of iron crystals, Proceedings of the Royal Society of London A, 761 (1926) 337–361.

[20] J.W. Christian, Some surprising features of the plastic deformation of Body-Centered Cubic metals and alloys, Metallurgical Transactions A, 14 (1983) 1237-1256.

[21] G. Taylor, Thermally-activated deformation of BCC metals and alloys, Progress in Materials Science, 36 (1992) 29-61.

[22] M.S. Duesbery, V. Vitek, Plastic anisotropy in b.c.c. transition metals, Acta Materialia, 46 (1998) 1481-1492.

[23] K. Ito, V. Vitek, Atomistic study of non-Schmid effects in the plastic yielding of BCC metals, Philosophical Magazine A, 81 (2001) 1387-1407.

[24] H. Gough, The behavior of a single crystal of alpha iron subjected to alternation torsional stresses, 1928.

[25] L.L. Hsiung, On the mechanism of anomalous slip in bcc metals, Materials Science and Engineering A, 528 (2010) 329-337.

[26] D. Kaufmann, R. Monig, C.A. Vokert, O. Kraft, Size dependent mechanical behavior tantalum, International Journal of Plasticity, 27 (2011) 470-478.

[27] D. Kaufmann, A.S. Schneider, R. Monig, C.A. Volkert, O. Kraft, Effect of surface orientation on the plasticity of small BCC metals, International Journal of Plasticity, 49 (2013) 145-151.

[28] C. Du, J.P.M. Hoefnagels, L.I.J.C. Bergers, M.G.D. Geers, submitted for publication, 2016.

[29] L.I.J.C. Bergers, J.P.M. Hoefnagels, M.G.D. Geers, On-wafer time-dependent high reproducibility nano-force tensile testing, Journal of Physics D: Applied Physics, 49 (2014) 495306.

[30] R.P. Steijn, R.M. Brick, Flow and fracture of single crystals of high-purity ferrites, Transactions of American Society for Metals, 46 (1954) 1406–1448.

[31] J.R. Greer, W.C. Oliver, W.D. Nix, Size dependence of mechanical properties of gold at the micron scale in the absence of strain gradients, Acta Materialia, 53 (2005) 1821-1830.

[32] P. Chen, H. Ghassemi-Armaki, S. Kumar, A. Bower, S. Bhat, S. Sadagopan, Microscale-calibrated modeling of the deformation response of dual-phase steels, Acta Materialia, 65 (2014) 133-149.

[33] D.B. Willianms, C.B. Carter, Transmission electron microscopy, second edition, Springer, (2009).

[34] G. Gottstein, Physical foundations of materials science, first edition, Springer, New York, (2004).

[35] M. Bertin, C. Du, J.P.M. Hoefnagels, F. Hild, Crystal plasticity parameter identification with 3D measurements and Integrated Digital Image Correlation, Acta Materialia, 116 (2016) 321-331.

[36] R.E. Smallman, R.J. Bishop, Modern physical metallurgy and materials engineering, sixth edition, Butterworth-Heinemann, (1999).

[37] M.S. Duesbery, On kinked screw dislocations in the BCC lattice-I, The structure and peierls stress of isolated kinks, Acta Metallurgica, 31 (1983) 1747-1758.

[38] M.S. Duesbery, On kinked screw dislocations in the BCC lattice-II. Kink energies and double kinks, Acta Metallurgica, 31 (1983) 1759-1770.

[39] M. Wen, A.H.W. Ngan, Atomistic simulation of kink-pairs of screw dislocations in body-centered cubic iron, Acta Materialia, 48 (2010) 4255-4265.

[40] F.L. Vogel, R.M. Brick, Deformation of ferrite single crystals, Transactions of the American Institute of Mining and Metallurgical Engineering, 5 (1953) 700–706.

[41] F. Roters, P. Eisenlohr, L. Hantcherli, D.D. Tjahjanto, T.R. Bieheler, D. Raabe, Overview of constitutive laws, kinematics, homogenization and multiscale methods in crystal plasticity finite-element modeling: Theory, experiments, applications, Acta Materialia, 58 (2010) 1152-1211.

Appendix

Crystal plasticity modeling (see [41]) accounts for the influence of crystallographic slip-induced anisotropic on plastic deformation. It is defined by considering the decomposition of the deformation gradient $\boldsymbol{F}$ into elastic $\boldsymbol{F}_e$ and plastic $\boldsymbol{F}_p$ contributions:

$$\boldsymbol{F} = \boldsymbol{F}_e \cdot \boldsymbol{F}_p \ .$$

Here, elasticity is described by the stress-strain relation

$$\overline{\boldsymbol{S}} = \mathbb{C} : \boldsymbol{E}_e$$

between the push-forward of the Second Piola-Kirchhoff stress to the plastic configuration and the elastic Green-Lagrange tensor. $\mathbb{C}$ is the cubic symmetric fourth-order elasticity tensor.

The plastic contribution to deformation is calculated via the plastic velocity gradient $\boldsymbol{L_p} = \dot{\boldsymbol{F}}_p \cdot \boldsymbol{F}^{p-1}$, which is a function of the plastic slip rates $\dot{\gamma}^\alpha$ on each α slip system

$$\boldsymbol{L_p} = \sum_{\alpha=1}^{n_s} \dot{\gamma}^\alpha \boldsymbol{P}^\alpha$$

where $\boldsymbol{P}^\alpha = \boldsymbol{s}^\alpha \otimes \boldsymbol{n}^\alpha$ is the Schmid tensor of the slip system with slip direction $\boldsymbol{s}^\alpha$ and normal $\boldsymbol{n}^\alpha$, and n_s is the number of slip systems.

The amount of slip on each slip system is determined by calculating the plastic slip rate $\dot{\gamma}^\alpha$, which is defined as

$$\dot{\gamma}^\alpha = \dot{\gamma}_0 \left(\frac{|\tau^\alpha|}{s^\alpha} \right)^{\frac{1}{m}} \text{sign}(\tau^\alpha)$$

where $\dot{\gamma}_0$ is a reference slip rate and m the strain rate sensitivity parameter. τ^α is the resolved shear stress on the αth slip system

$$\tau^\alpha = (\boldsymbol{C}_e \cdot \overline{\boldsymbol{S}}) : \boldsymbol{P}^\alpha$$

where $\boldsymbol{C}_e$ is the elastic right Caughy-Green strain.

The current slip resistance (or yield stress) s^α is defined by the evolution law

$$\dot{s}^\alpha = \sum_{\beta=1}^{n_s} h^{\alpha\beta} |\dot{\gamma}^\beta|$$

where $h^{\alpha\beta}$ is the hardening matrix. This matrix has the form

$$h^{\alpha\beta} = h_0 \left(1 - \frac{s^\alpha}{s_\infty} \right)^a q^{\alpha\beta}$$

where $q^{\alpha\beta}$ is a matrix where elements are equal to 1 on the diagonal and equal q_n off diagonal.

This crystal plasticity model has been implemented as a user-defined element subroutine in a commercial FE code. Table 4.A.1 reports the fitted parameters related to results reported in Fig. 4.7 in the main text.

Table 4.A.1. Crystal Plasticity model parameters adopted for Configuration 1 and 2.

Initial slip resistance, {110}	τ_{0A}	35 MPa
Initial slip resistance, {112}	τ_{0B}	40 MPa
Slip resistance saturation value {110}	$s_{\infty A}$	70 MPa
Slip resistance saturation value {112}	$s_{\infty B}$	105 MPa
Initial hardening rate {110}	h_{0A}	8 GPa
Initial hardening rate {112}	h_{0B}	12 GPa
Reference slip rate	$\dot{\gamma}_0$	0.01
Strain rate sensitivity	m	0.05
Hardening exponent	a	1.5
Ratio self/latent hardening	q_n	1.4
Elastic constant	C_{11}	233.5 GPa
Elastic constant	C_{12}	135.5 GPa
Elastic constant	C_{44}	118.0 GPa

Chapter 5. Martensite crystallography and chemistry in dual phase and fully martensitic steel[1]

Abstract

Lath martensite is important in industry because it is the key strengthening component in many advanced high strength steels. The study of lath martensite crystallography and chemistry is extensive in the literature, however, most studies are based on fully martensitic steels. In this work, lath martensite in dual phase steels is investigated with a focus on the substructure identification of the martensite islands and microstructural bands using electron backscattered diffraction, and on the influence of the industrial coating process on the alloying elements distribution using atom probe tomography. Unlike findings for the fully martensitic steels, no martensite islands with all 24 Kurdjumov-Sachs variants have been observed. Almost all martensite islands are transformed from a single prior austenite grain, with most laths within one main packet. In addition, most sub-blocks seem to have only one lath, contrary to sub-blocks containing multiple laths in fully martensitic steel. Similarly, the martensite bands are composed of connected packets from different prior austenite grains with only few random blocks. The coating process causes a strong carbon partitioning to lath boundaries and Cottrell atmospheres at dislocation core regions, while auto-tempering also contributed to the carbon redistribution. The substitutional elements are all homogenously distributed. The phase transformation process has two effects on the material: mechanically, the earlier-formed laths are larger and softer and therefore more ductile, and chemically, due to the lower dislocation density inside the larger laths, carbon Cottrell atmospheres are predominantly observed in the smaller laths.

5.1 Introduction

Ferrous martensite appears in a variety of morphologies, such as lath, lenticular and thin-plate, which are influenced by the alloying elements, the transformation temperature, and the state of prior austenite [1-3]. Among these morphologies, lath martensite has a particularly high industrial relevance, as it is the main strengthening component of many advanced steels. Typical representatives are dual phase (DP) steels, transformation induced plasticity (TRIP) steels, maraging steels, and quenching and partitioning (QP) steels.

Lath martensite is formed in Fe-C(<0.6%wtC), Fe-Ni(<28wt%Ni), and Fe-Mn(<10wt%Mn) alloys [4]. Its morphology and crystallography have been investigated extensively using different experimental techniques, including optical microscopy [2,5,6], scanning electron microscopy (SEM) [6], transmission electron microscopy (TEM) [2,5-9] and electron

---

[1] Reproduced from: C.Du, J.P.M. Hoefnagels, S. Koelling, M.G.D. Geers, R. Petrov, V. Bliznuk, A. Behnam, J. Sietsma, P. Koenraad, Martensite crystallography and chemistry in dual phase and fully martensitic steel, submitted (2016).

backscattered diffraction (EBSD) [5,6,10], providing a detailed description of the substructure constituents. Due to the diffusionless phase transformation, there exists an orientation relationship (OR) between the prior austenite (parent phase) and martensite laths (product phase). The OR of lath martensite is generally close to the Kurdjumov-Sachs (K-S) OR, where the habit plane ranges from $\{111\}_\gamma$ to $\{225\}_\gamma$ and $\{3\ 10\ 15\}_\gamma$, which depends on the chemical composition of the material [4,5,9]. The most fundamental structure units, the laths, with small misorientations (2-5°), are bundled together in a so-called 'variant' or 'sub-block' [6]. There are 24 possible K-S variants originating from a single prior austenite grain, which are grouped into a hierarchical structure of packets, blocks and sub-blocks. The variants within a packet share the same habit plane, which is one of the four $\{111\}_\gamma$ closest packed planes of the prior austenite. Each packet contains three blocks, each with a different closest packed direction parallel to that of the parent austenite. Each block can be further divided into two sub-blocks which share the same Bain axis and have a misorientation of ~10° with each other. Figure 5.1(a) shows a schematic drawing of the substructures of lath martensite in a prior austenite grain. Figure 5.1(b) shows the pole figure of the 24 variants, taking the crystallographic coordinate of Variant 1 as the reference. A detailed overview of the misorientation values between the 24 variants can be found in [5].
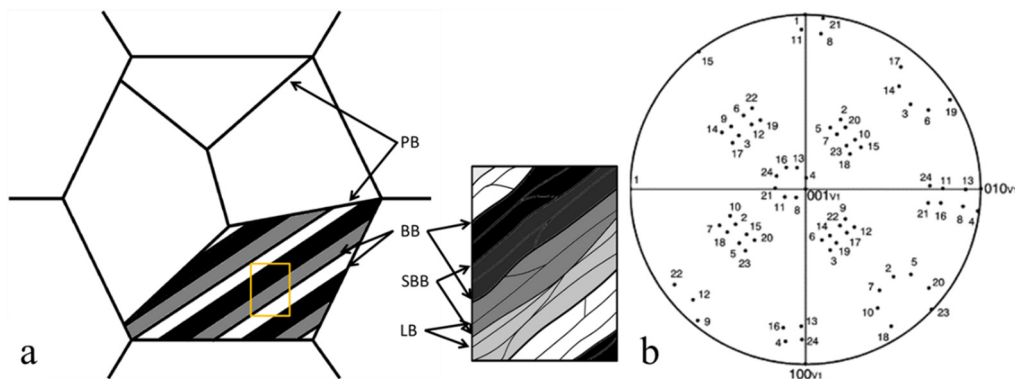
Figure 5.1(a) Schematic drawing of the hierarchical microstructures of lath martensite in a prior austenite grain. A zoom-in of the orange frame shows substructures at smaller scales. PB, BB, SBB, LB represent packet boundary, block boundary, sub-block boundary and lath boundary respectively. The typical size of a packet is a few micrometres to tens of micrometres. (b) Pole figure showing the orientation of the 24 K-S lath martensite variants with respect to the crystal coordinate of variant 1 [5].

Lath martensite appears in engineering metals either as one of the component phases in multi-phase materials, or as the single phase of a fully martensitic (FM) steel. A vast amount of research has been done on the morphology and crystallography of FM steels in the literature. All above-mentioned conclusions related to the OR between martensite and prior austenite and the sub-structures of lath martensite originate from FM steels. Considerably less work has been done on lath martensite crystallography in multiphase steels. The typical dimensions of the martensite islands in multiphase steels and their substructures are smaller, by which the

present variants differ from those found in FM steels. It is therefore necessary to investigate the substructures of lath martensite in multiphase steels in more detail.

This paper focuses on a particular multiphase steel, i.e. DP steel, which is an advanced high strength steel that is widely used in the automobile industry. DP steel contains mainly ferrite and martensite, with martensite acting as the strengthening phase. Commercial DP steels are typically produced by rolling, which leads to severe banding of martensite in the centre region of the material's thickness direction [11,12]. The effect of this banding on the mechanical properties is generally assessed to be negative, e.g. in [12,13]. However, insights into the precise crystallography of such banded structures is still missing in the literature.

Besides the crystallography, the distribution of the alloying elements is essential for the mechanical properties of materials. The local chemical composition analysis of lath martensite is traditionally investigated using X-ray methods, TEM related techniques and electron probe microanalysis in SEM. However, it is difficult to obtain the local element distribution at sub-micron scale due to resolution limitations of these methods. Recently, 3D atom probe tomography (APT) has been widely applied to acquire the element distribution of materials in 3D at atomic scale [14,15]. The application of APT to lath martensite, e.g. in [16,17], provided novel insights into the alloying elements distribution and their potential influence on the mechanical response of FM steels. Studies of the element distribution in lath martensite in DP steel at this scale are rare. Moreover, there are no studies on the effects of the commonly applied industrial coating process on the element distribution of lath martensite in the commercial DP steels. Using 3D APT, a comparison between DP steel with and without coating can yield a deeper understanding of the influence of the coating process on the element distribution and the mechanical properties.

This study is structured as follows. The crystallography of lath martensite in a commercial DP steel is investigated using EBSD and TEM, where both the martensite islands and the martensite bands formed due to the rolling process will be studied, using a FM steel with the same overall chemical composition as a reference. In addition, the alloy element distribution of a commercial DP steel and a home-made DP steel will be measured using APT to understand the influence of coating process on the element distribution, where again a FM steel will be used as a reference.

5.2 Experiments

The materials used in this study are a commercial DP600 steel (DP^C), a lab-processed DP steel (DP^L) and an FM steel. The DP^C steel (0.092C-1.68Mn-0.24Si-0.57Cr in mass percent/ 0.43C-1.68Mn-0.48Si-0.61Cr in atomic percent) was subjected to a zinc coating process at 450 °C for 5 mins. The DP^L is obtained by reheating the DP^C to the inter-critical range at 750 °C for 5 mins followed by water quenching to room temperature. This should remove the influence of the thermal treatment during the coating process. The volume fraction of martensite in both DP^L and DP^C is approximately 25%. The FM is obtained by heating the DP^C at 1000 °C for 2 hours followed by water quenching to room temperature. The long homogenization time removes the chemical heterogeneities in the DP^L and is meant to obtain large prior austenite grain size.

The materials are characterized by EBSD, TEM and the local chemical composition is measured by APT. For EBSD investigations, the specimens were prepared by grinding and polishing and finished by electro-chemical polishing using A2 electrolyte from Struers with a voltage of 40 V for 10 seconds at room temperature. The EBSD measurement was carried out using an EDAX system mounted on a FEI Sirion SEM. A cleaning step of the raw EBSD data was applied by using the neighbor confidence index correlation method for pixels with a confidence index lower than 0.1. The TEM sample was prepared by double-jet electro-chemical polishing of a thin plate that was thinned by grinding and polishing. The APT specimens were prepared by lift-out methods using FIB from a bulk material that was finished by electro-chemical polishing. A final step with low beam current and voltage (5 kV, 44 pA) was applied to minimize the impact of the Gallium ion beam on the analysed volume. The APT measurements were conducted using a local-electrode atom-probe system (LEAP 4000X-HR, Cameca Instruments) in voltage mode at a specimen temperature of ~65 K. Data analysis was performed using the IVAS software (Cameca Instruments) and the mass-to-charge peaks are decomposed according to the proportion between isotopes of the alloying elements.

5.3 Results and discussion

5.3.1 Morphology

Figure 5.2 shows typical TEM bright field images of lath martensite in DP[C] and FM steel, respectively (Fig. 5.2(b)). In Fig. 5.2(a) the dark martensite island in DP[C] is surrounded by ferrite grains. Two sharp and bright laths are visible while other laths are more blocky. In contrast, the laths in FM steel (Fig. 5.2(b)) are much longer and stacked on top of each other. Parallel laths are likely to belong to the same packet, since the substructures in the same packet share the habit plane. Although the size of the martensite island of DP is significantly smaller than the FM martensite packets (also shown later in this paper, Fig. 5.3-7), the lath widths are of a comparable size.
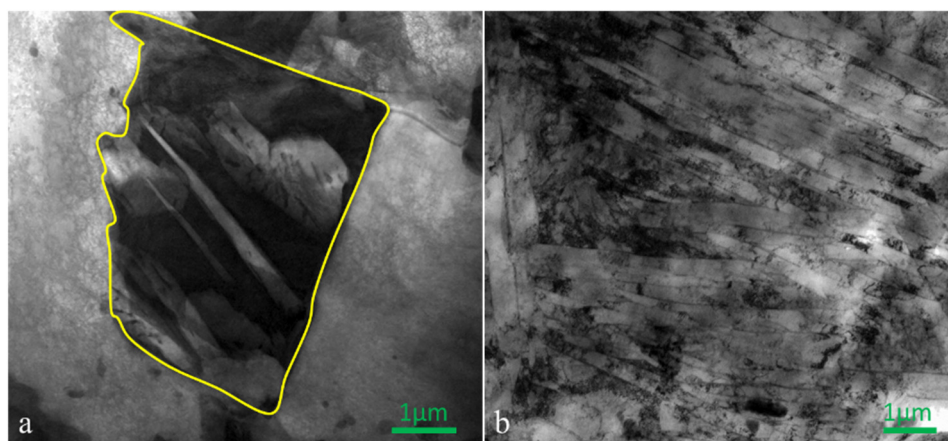
Figure 5.2 TEM bright field image of lath martensite from (a) commercial DP 600 steel (DPC) and (b) fully martensitic (FM) steel. The island marked with the yellow line is lath martensite in (a).
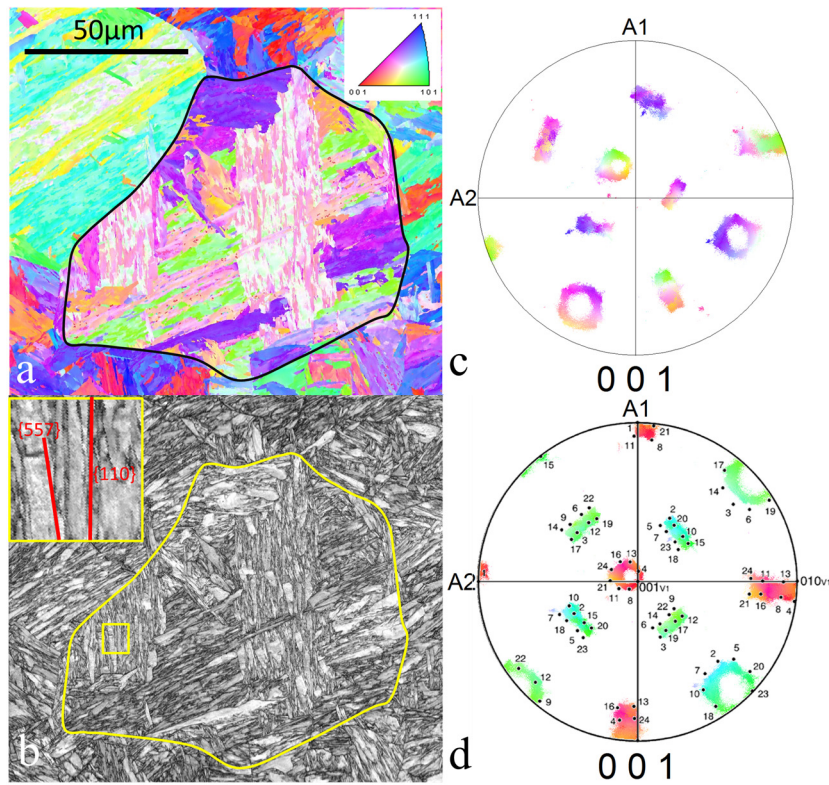
Figure 5.3 (a,b) Typical IPF and IQ maps of FM steel with a prior austenite grain marked by black/yellow lines. The insert in (b) is a zoom-in of the yellow square region, which shows the traces of substructure boundaries in the packet. The two red lines mark the theoretical surface trace of {110} and {557} planes respectively, which indicates that the habit plane is {110}. (c) Pole figure of the prior austenite region highlighted with the corresponding colours in the IPF. (d) The pole figure of (c) rotated to the frame of the reference pole figure in order to identify the presence of the variants.

5.3.2 Crystallography

Figure 5.3(a) shows an inverse pole figure (IPF) map from EBSD measurements of the FM steel. The image quality (IQ) map, which is shown in Fig. 5.3(b), clearly shows the substructure boundaries. The prior austenite grain is reconstructed using the method proposed in [18] and marked by black and yellow lines in Fig. 5.3(a,b), respectively. Parallel blocks are clearly visible in the packets, and each block contains two sub-blocks with a misorientation of ~10°. The sizes of packets and blocks are not equal and the laths in the large packets/blocks are more parallel than the ones in the smaller packets/blocks that show a more random morphology, which is in line with [19]. The traces of {110} and {557} families are shown in the inset of Fig. 5.3(b), whereby the {110} traces are aligned much closer to the lath boundary direction, indicating that the habit plane of the material is close to {110}. The pole figure of the marked prior austenite region shown in Fig. 5.3(c) is rotated to maximize the overlap with the theoretical pole figure of the K-S OR, as is shown in Fig. 5.3(d). It can be seen that the experimental pole figure matches well with the theoretical one, indicating that the laths are close to the K-S orientation relationship with respect to the prior austenite. Although only three packets are visible at the

surface, for which not all variants are observable in this measurement, the three Bain zones are present, evidenced by all theoretical points almost coinciding with the measured ones.
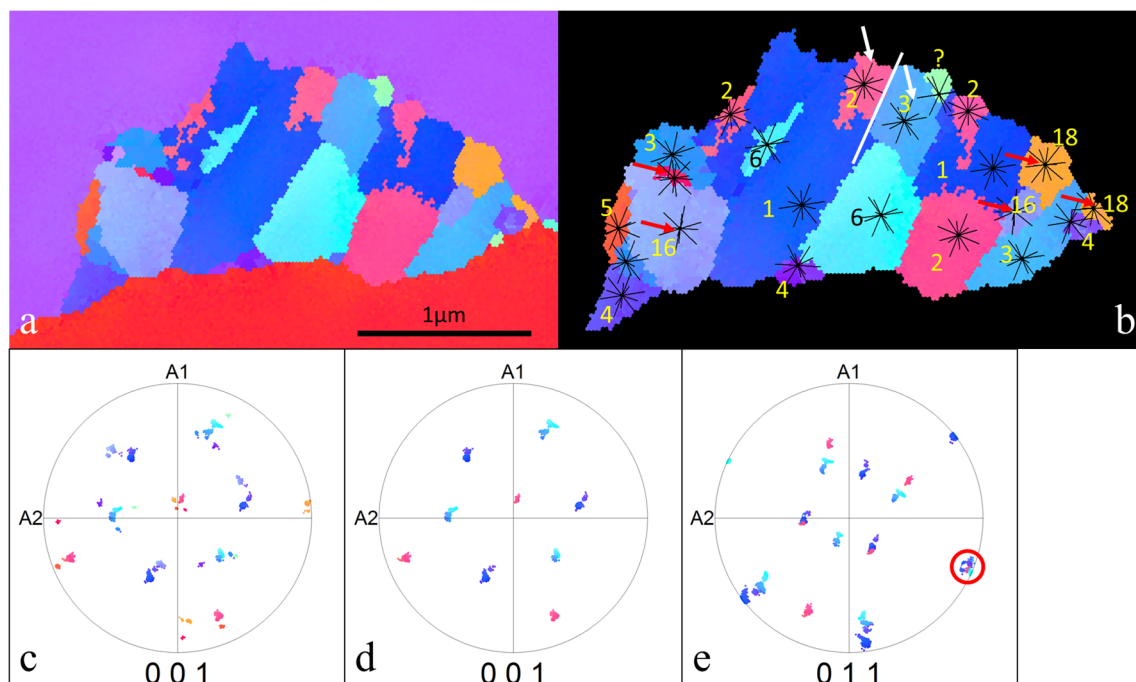
Figure 5.4(a) A typical EBSD measurement of a lath martensite island in DP^C steel. The top purple and bottom red grains are ferrite grains. The small martensite grains are separately shown in (b). {110} plane traces are marked for every block for identification of the variants belonging to the same packet. Variant V1-V6 belong to the same packet. Variant V16 and V18 are from a second packet. The small variant marked with question mark do not originate from the prior austenite grain containing the numbered variants. (c) {001} pole figure of the complete area. (d) {001} and (e) {110} pole figure of only the V1-6. The projection point marked in red denotes the common habit plane.

Figure 5.4 shows an EBSD measurement of a lath martensite island in DP^C steel. The large purple and red grains are ferrite and the small grains in the centre of Fig. 5.4(a) are martensite, which are separately shown in Fig. 5.4(b). The boundaries are nearly parallel, except for the curved ones. It may therefore be assumed that they belong to the same packet. Trace analysis shows that most traces correspond to the {110} planes, suggesting the habit plane to be {110} for the FM steel. However, the {001} pole figure of the martensite island shown in Fig. 5.4(c) does not show such a complete and organized distribution as shown in the FM pole figure in Fig. 5.3(d). Hence, variants from different packets might be present. To identify these variants, the surface traces of all {110} planes are plotted for each of the coloured regions in Fig. 5.4(b). Since there are six {110} planes, only the trace (e.g. the one marked by white arrows for variant 2 and variant 3 respectively) that is parallel to the parallel variant boundaries (the white line in Fig. 5.4(b)) is the one representing the habit plane. The substructures from the same packet share the habit plane and thus the corresponding {110} plane traces are parallel. The pole figure of

the martensite island without the marked regions in Fig. 5.4(d) shows a twinned distribution of three sets of projection points. The sub-blocks have been identified by rotating the {001} pole figure to overlap with the reference pole figure (Fig. 5.3(d)). The regions marked by red arrows do not belong to the packet, but are identifies to belong to the same prior austenite grain (V16, V18). The island is therefore predominantly a single packet of variants, with two smaller variants (V16 and V18) from another packet, and the small unidentified variant marked with question marks at the island extremities. All three blocks are present in this main packet, with 6 variants present as also indicated by small misorientation between the projection points in the pole figure. The misorientation is ~60° across the block boundaries and ~10° across the sub-block boundaries. The presence of sub-blocks rules out the Nishiyama-Wassermann OR which does not have sub-blocks. The variants seem to be distributed randomly and variant pairs, such as V1-V4, V2-V5 and V3-V6 that are frequently reported in FM steels [5], are not present. In addition, unlike the sub-blocks of FM steel shown in Fig. 5.3, there are no lath boundaries observable in the EBSD micrographs of the DP martensite island. The lowest level of the hierarchical structure is therefore sub-blocks with a size in the range of 50 nm to 500 nm. The morphology of the sub-blocks is mostly equi-axed, which also differs from the lath shape of the FM steel shown in Fig. 5.3.
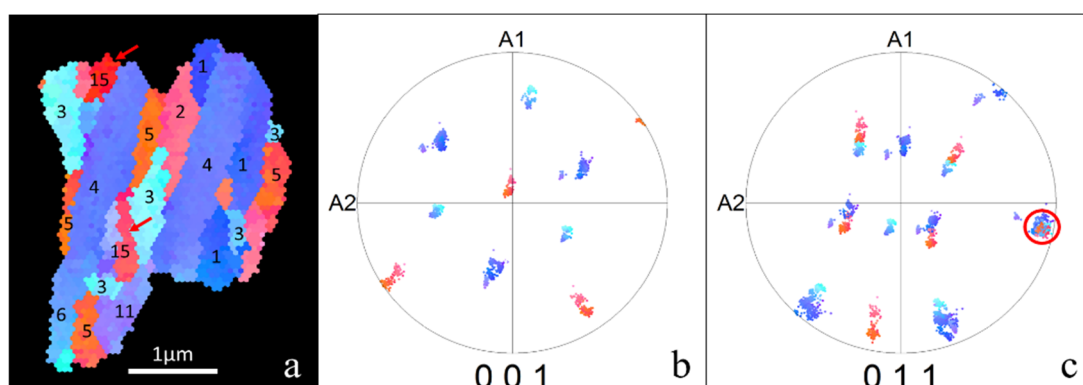
Figure 5.5(a) A martensite island from DP^C mainly composed of a packet with all 6 variants and a minor variant V15 from the same prior austenite. This is confirmed by the {001} and {011} pole figures of variants V1-V6 (b,c). The projection point marked by the red circle represents the common boundary plane of variants V1-V6.

The habit plane traces, as explained above, can be used to verify if a sub-block/block belongs to a certain packet, and to identify the variants that belong to a different packet than the rest of the blocks. Using the same method, a second martensite island is analysed, as shown in Fig. 5.5(a). Analysis reveals that the red block marked by the red arrow does not belong to the packet which contains all unmarked regions. This martensite island therefore also consists of one main packet and a minor variant of a different packet, similar to the DP island analysed in Fig. 5.4. Again, the sub-block seems to be the fundamental structure unit, because no lath boundaries are visible in the martensite island shown in Fig. 5.5. In contrary to the martensite shown in Fig. 5.4, the laths in this region have a higher length/width aspect ratio, but their shape is still

'blocky' compared to the laths in the FM steel (Fig. 5.3). In this measurement, variant pairs are present, e.g. V1 shares a boundary with V4, while V2 and V5 share a boundary as well. The {001} and {011} pole figures of variant V1-V6 in Fig. 5.5(b,c) confirms that this island is mainly composed of a single packet.

Figure 5.6 shows an EBSD micrograph of a lath martensite band around the centre of the thickness direction of the DP^C sheet. Since comparable colours between martensite and ferrite may trigger confusion, the IPF map (Fig. 5.6(a)) is shown together with an image quality (IQ) map (Fig. 5.6(b)). The dark regions in the IQ map have a lower image quality compared to the adjacent ferrite and are identified as martensite because the large density of dislocations inside the laths distorts the crystal lattice and thus the Kikuchi patterns. The main martensite regions are divided into five domains, which are marked with blue outlines and numbers. These domains are analysed separately and shown in Fig. 5.6(c-g). By the same method proposed in Figure 5.4, a packet is identified in each domain. Only the variants that belong to the main packet are shown, together with the {001} and {011} pole figure of only these variants. The orange arrows in the IPF indicate the locations in the martensite band where minor variants exist that do not belong to the main packet and are therefore made invisible. It is interesting that all these minor variants are found to belong to the same prior austenite as the main packet. The projection points marked by the red circle in the {011} pole figures represent the habit plane of the packet, which is shared by all the variants. Similar to the observations of the martensite islands in Fig. 5.3-5.4, the sub-structure boundaries are approximately parallel to the {110} plane trace and all the 6 variants are present in the identified packet for domain 1, see Fig. 5.6(c). Variant pairs are observed for all three blocks. The adjacent domain 2 does not show straight and parallel sub-structure boundaries. But still a packet is found with 6 variants, as shown in Fig. 5.6(d). Domain 3 has been identified to be a single packet, but not all 6 variants are present. The presence of only 2 blocks does not give a certain {110} pole of habit plane based only on information of the projection points. However, due to the parallel boundaries between the yellow block and two blue blocks, the habit plane is the one which represents a vector which is perpendicular to the boundary traces. Therefore, the probable projection point is marked in the {110} pole figure in Fig. 5.6(e). The boundaries are irregular inside domain 4, which is identified to be a full single packet with minor variants of the same prior austenite grain. The identified packet in domain 5 shows regular substructures and variants are fully present in the packet, as indicated by Fig. 5.6(g).
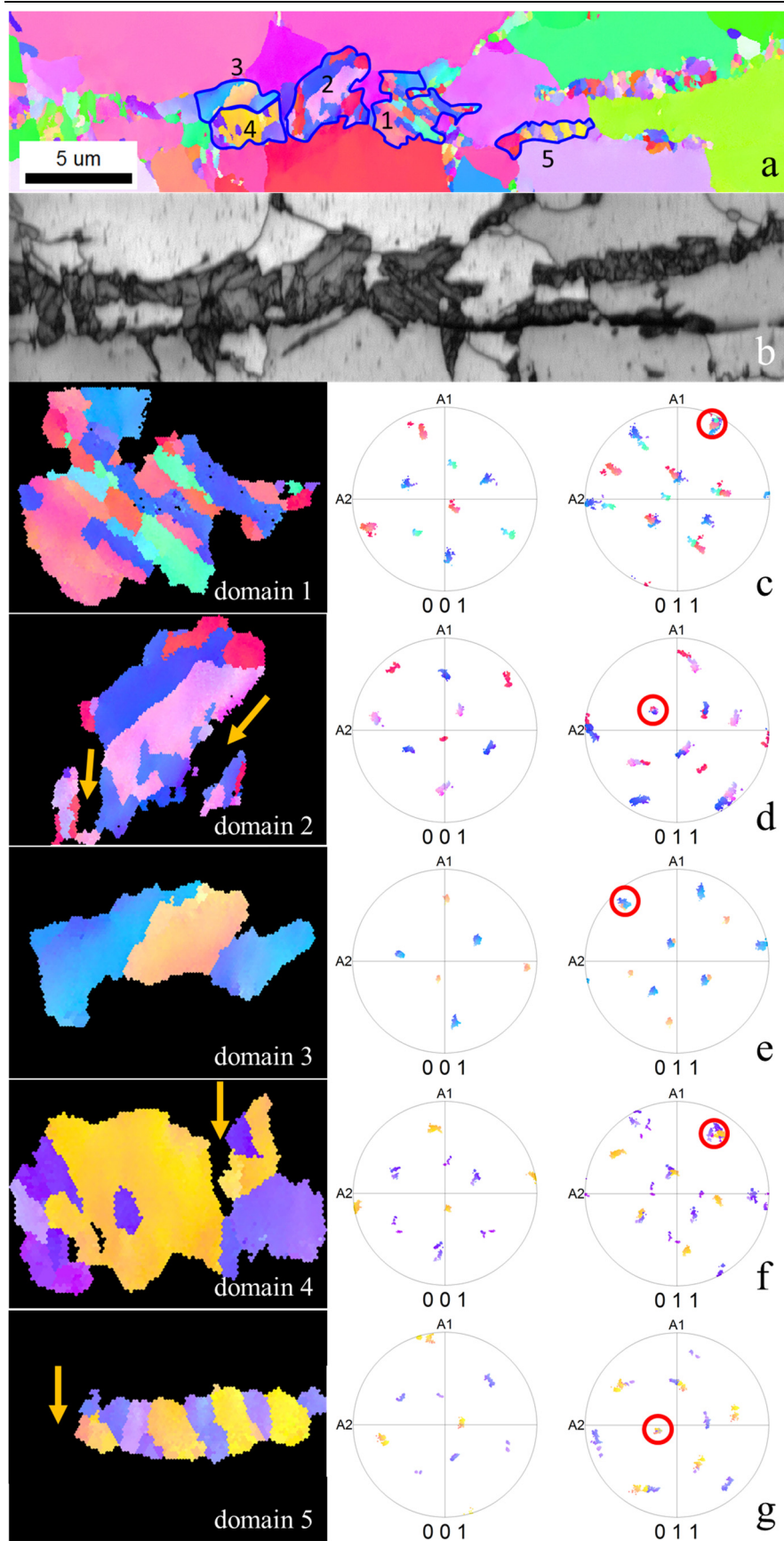
Figure 5.6 (a) IPF and (b) IQ map of a lath martensite band in the middle of the thickness direction of DP^C steel. The dark regions in the IQ map represent martensite, with different domains by marked by blue lines. In (c-g) the variants belonging to the identified main packet of domains 1-5 are shown in the IPF together with the {001} and {011} pole figures. The orange arrows indicate the locations in martensite domains where minor variants exist that do not belong to the main packet and are therefore made black. The red circles in the {011} pole figures mark the projection point of the habit plane, which is shared by all variants.

In general, four full packets can be identified in the band, whereas the fifth packet contains only two blocks. In addition, most of the adjacent packets do not originate from the same prior austenite grain. This is similar to the measured martensite islands (Fig. 5.4-5.5), which are predominantly a single packet with minor variants from another packet of the same prior austenite grain. However, conclusions may be different for the many smaller martensite islands that exist and that are difficult to measure by EBSD with good image quality. These small, strong islands seem to show much lower degree of deformation than the large islands [20] and therefore may not play an important role in the overall mechanics of DP steel during deformation. The martensite domain size is inherited from the size of prior austenite grains, which are nucleated during the inter-critical annealing at the boundaries of ferrite grains, and is controlled by the local austenite grain growth rate. The competition between austenite nucleation and grain growth determines the final austenite grain size. In martensite regions to the upper right of domain 5 in Fig. 5.6 the nuclei of austenite are probably more numerous than in other regions, which leads to smaller austenite grains and therefore smaller packets after transformation. According to Ref. [21] the initial variant that is formed is triggered through an energy minimization, which is followed by the formation of a block from a second packet belonging to the same Bain zone corresponding to the first one. This might explain the existence of the minor sub-blocks from the second packet in Fig. 5.3-5.4. In addition, the size of sub-blocks/blocks are different within the same packet. The larger ones are expected to form at earlier stages when more space was available for the laths to grow [17]. The later-formed ones have less space and the austenite lattice is already strained by the adjacent prior martensite transformation. Hence, they are smaller and more dislocated, leading to a lower image quality in the EBSD measurement. This phenomenon will probably lead to heterogeneity of mechanical properties of lath martensite, which can be assessed by locally probing the mechanical material behaviour by means of nanoindentation, which is discussed next.

Due to the small dimensions of the martensite islands in DP steel, the nanoindentation measurements will be affected by their distance to the much softer ferrite phase, which makes a reliable measurement of any correlation between the hardness and the lath size unfeasible. However, as can be seen in Fig. 5.3, the FM microstructure also shows laths with different dimensions. Hence, a series of nano-indentation tests have been applied on the FM steel, as shown in Fig. 5.7, and the location of each indent has been analysed with EBSD. The hardness has been plotted as a function of the width of the indented lath, while the data points have been grouped by the position of the indents, i.e. inside the lath, on a low angle boundary, or on a high angle boundary. Even though there is a considerable scatter in the data due to the large variability in 3D microstructure and chemical distribution at each indenter location, the hardness clearly increases going from indentations in the laths, to indentations on low angle boundaries, to indentations on high angle boundaries. These boundaries act as barriers to dislocation motion, and the strengthening effect is larger for high angle boundaries, which is in qualitative agreement with results in the literature [22] and, in particular, with direct micro-mechanical measurements on the same FM material reported recently [23]. A clear trend is visible that the thicker laths are softer, which is probably due to less dislocations and

boundaries, confirming the explanation above. According to [24], this means that the larger laths have a higher probability to fail during service.
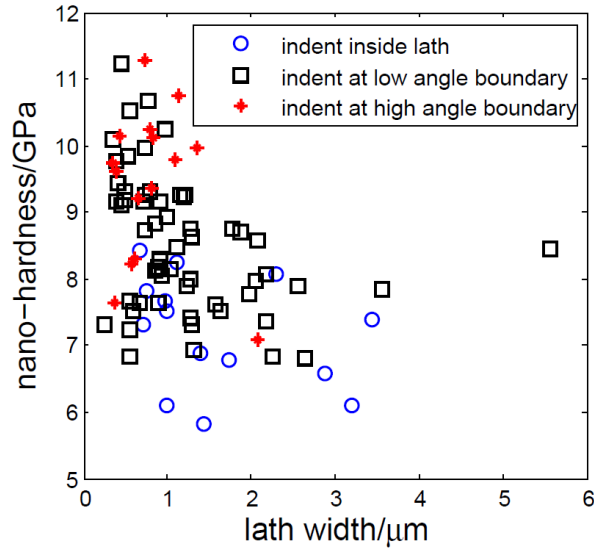
Figure 5.7 Nano-indentation measurement of the FM steel. The hardness is plotted as a function of the width of lath. The indent positions are grouped. A trend emerges, indicating that the thicker laths are softer.

5.3.3 Element distribution

The element distribution is analysed through reconstructed 3D maps from APT measurements. First, one APT specimen from the early-formed (DP^{C}A) and one from the late-formed (DP^{C}B) martensite in the quenching process of coated DP^C are discussed, followed by APT results for the un-coated DP^L and FM material. Figure 5.8 shows an overview of the element distribution for specimen DP^{C}A. Partitioning of carbon into layers occurs, while all the analysed substitutional elements, Cr, Mn and Si, are homogeneously distributed. To visualize the C partitioning more clearly, the iso-surface at 5at% C is presented in Fig. 5.8(f), where the carbon-enriched boundary layer is clearly visible. Three layers with high C concentration are observed and the distance between the top two layers is ~60 nm, which corresponds to the average lath thickness. The logical explanation is to identify these two layers as lath boundaries regions. The average C concentration at the bottom right of the specimen is considerably lower, i.e. only 0.23 at%, which is a clear indication that this is ferrite, as shown similarly in [25]. The rest of the specimen is martensite with an average C concentration of 2.24 at%, which is significantly higher than the calculated C content for martensite, i.e. (1.7±0.2) at%, assuming a homogeneous C distribution in martensite and a martensite volume fraction of (25±3)%. The chemical composition of the volume enclosed by the green frame, an in-lath region, in Fig. 5.8(f) is presented in Fig. 5.8(g), which shows a nearly homogenous distribution of all alloying elements inside the laths. The distribution of the main elements inside the blue frame in Fig. 5.8(f) along the direction crossing the bottom boundary layer is shown in Fig. 5.8(h). This plot confirms the heterogeneous distribution of C, in contrast to the homogenous distribution of substitutional

elements across ferrite, martensite, and their boundary layer.
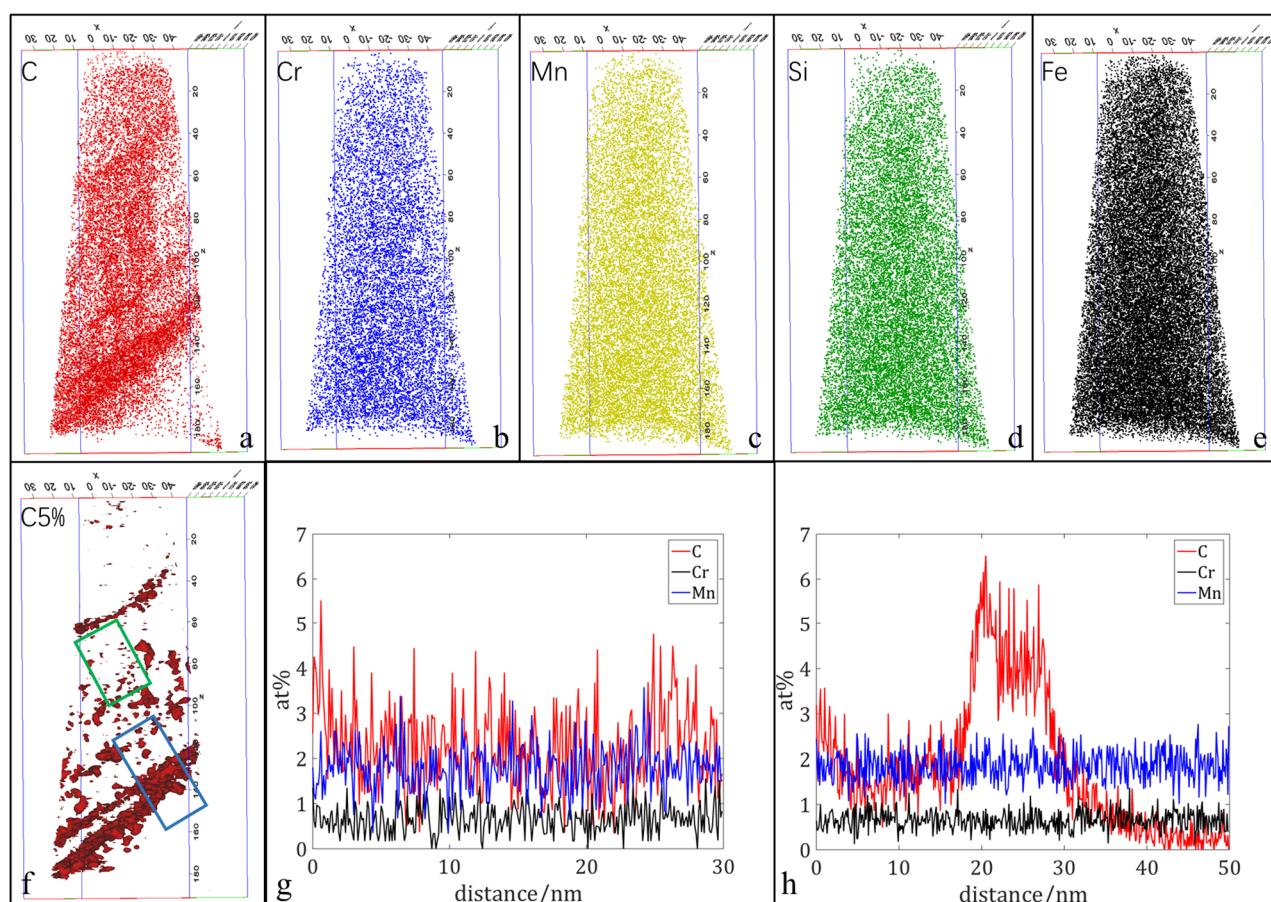
Figure 5.8 3D element distribution maps of specimen DP^{C}A taken from early-formed martensite in DP^C. (a) inhomogeneous layerwise C distribution is visible. (b-d) substitutional elements (Cr, Mn, Si) distribution and (e) map of the base element Fe. (f) iso-surfaces of C with 5at% of specimen DP^{C}A. (g,h) the elements distribution in the highlighted green and blue volumes respectively in (f).

The C distribution of the late-formed martensite DP^{C}B is shown in Fig. 5.9(a). The 3D maps of the other elements are not presented because segregation was again not observed. The overall C concentration is 2.98at%, which is considerably higher than in the martensite of specimen DP^{C}A. In contrast to the enriched C layers observed in Fig. 5.8, this specimen shows a strong partitioning of C atoms in a network-like structure for which a maximum C concentration as high as ~16.0at% is found. This network is more visible in the iso-surface shown in Fig. 5.9 (a), which has the appearance of the 3D structure of a dislocation network. Therefore, the most logical interpretation is that the enrichment of C in this network is caused by C segregation in the Cottrell atmosphere of the dislocations [26]. The consequence of the carbon segregation in boundary layers and dislocation networks is that the carbon concentration in dislocation-free regions inside the laths must be significantly lower than the average C content in martensite, as observed for instance in the top part of the specimens (Fig. 5.8(f), Fig. 5.9(a)).

The C distribution map and the iso-surfaces of the un-coated DP^L specimen are shown in Fig.

5.9(b). In contrast to the coated DP^C specimens, the C distribution in DP^L is far more homogeneous with an average concentration of 1.94at%, which is in agreement with the homogeneous C content in martensite of (1.7±0.3) at% (note the somewhat larger estimated error bar than for the un-coated DP). No clear (dislocation) networks or (boundary) layers of C enrichment regions are observed as the density of 5at% C iso-surface regions is significantly less than the 5 at% iso-surfaces of the DP^C samples (Fig. 5.8(f), Fig. 5.9(a)).
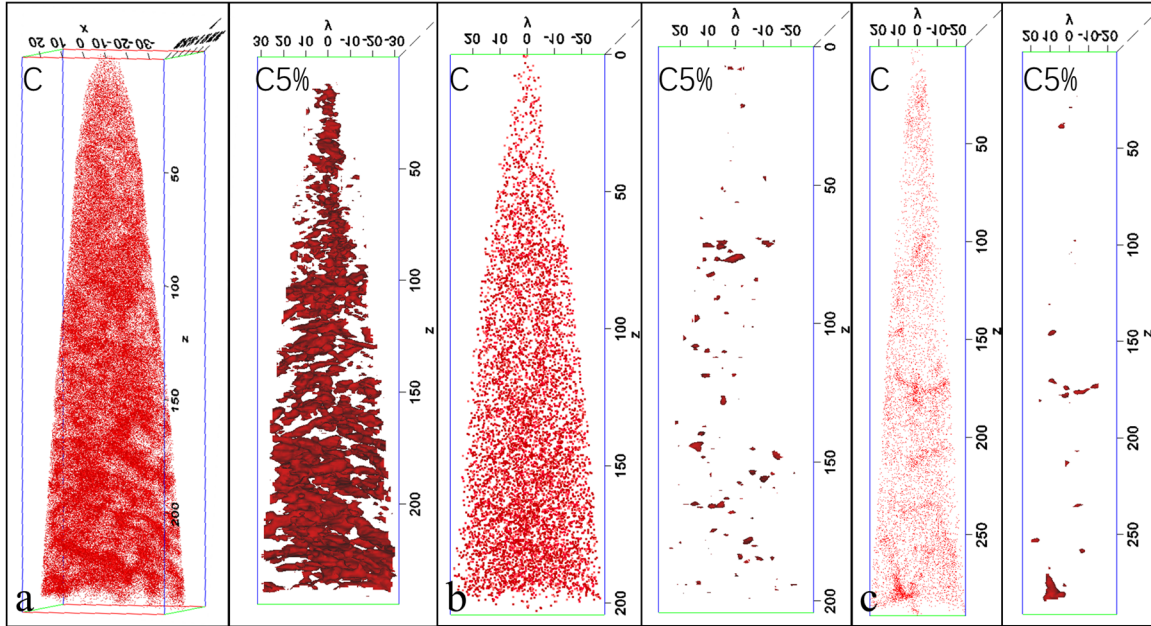
Figure 5.9 (a-c) (a-c) C distribution maps along with their 5 at% iso-surface for (a) DPCB specimen taken from late-formed martensite in coated DPC steel, (b) the un-coated DPL specimen, and (c) the FM material. The particle size of the C map is moderated to increase the visibility of carbon concentrations in the materials.

The C distribution map and the iso-surfaces of C from the FM specimen are shown in Fig. 5.9(c). The average C concentrations of FM and DP^C are identical since the base material of FM is obtained by heat treatment of DP^C. A change of martensite volume fraction from (25±3) % to 100% lowers the C concentration with a factor of 4 in the martensite. The average C concentration is 0.57at%, which is slightly higher than the overall C concentration of DP^C/DP^L (0.43at%). However, the C atoms in the APT tip reveal a minor partitioning to the Cottrell atmosphere of two dislocations, as indicated by the C map and the 5at% iso-surface. The number of Cottrell atmospheres is much less than that of specimen DP^{C}B, which suggests that the dislocation density in FM martensite is not that high.

Generally, the distribution of the substitutional alloying elements is homogeneous in the three tested materials, which complies with the observations in the literature [16,27]. On the contrary, the C distribution shows partitioning to different degrees. The Ms temperature of FM is estimated to be ~370 °C using the formula proposed in [28]. Therefore, auto-tempering of several seconds can occur in the FM steel during quenching. On the other hand, due to the large

prior-austenite grain size, the dislocation density in the FM specimen is lower than that of the DP^C specimens, therefore, the Cottrell atmospheres in the FM specimen are less numerous than in specimen DP^{C}B. The Ms temperature is estimated to be ~270 °C for both the coated DP^C and un-coated DP^L specimens. Therefore, a shorter period of auto-tempering is expected to have occurred in both DP materials. Similar to the FM specimen, the C enrichment in the un-coated DP^L is not obvious, i.e. only a small number of C-enriched regions are visible in the 5% iso-surface map, which seems to be random scattering in the specimen volume. In contrast, the DP^C samples show significant partitioning. This difference is due to the coating process at 450°C for 300 seconds which enables the diffusion to redistribute the C atoms in DP^C to the dislocation cores and boundary layers. Therefore, whereas the auto-tempering during quenching has only a limited influence on the C segregation, the thermal treatment accompanying the coating process causes strong C segregation.

Carbon partitioning to the boundary regions and dislocation structures is driven by the supersaturation of C in martensite. In specimen DP^{C}A, the thickness of the enriched C layers between two adjacent martensite laths is ~10 nm. Based on the C concentration of ~5at%, these ~10 nm-thick layers may be layers of inter-lath retained austenite, as a similar thickness and C concentration was found for inter-lath retained austenite layers in [16]. The Cottrell atmosphere around dislocations in martensite and bainite has been measured (by APT) in Refs. [16,27,29,30]. The maximum C concentration in the core of a Cottrell atmosphere was found to be higher than the theoretical maximum value of 6at% [31], but lower than the C concentration in carbides [32]. Therefore, these Cottrell atmospheres can be the possible regions of carbides formation if more C atoms are able to segregate there, as suggested in [33].

The two DP^C specimens were fabricated from the same martensite island, however, they show a completely different C atom segregation behaviour. This may well originate from the transformation sequence, as already briefly addressed in the EBSD results. The substructure size in early-formed martensite is larger than that in late-formed martensite because more space was available for the phase transformation at the earlier stage. In contrast, in the late-formed martensite, more dislocations are present for the accommodation of C atoms, as a result of the larger transformation-induced strain emanating from the growing constraint on the remaining austenite. This explanation is supported by the EBSD measurements of the lath martensite in DP steel, as the smaller sub-blocks and blocks have a lower image quality of the measured Kikuchi patterns, as visible in IQ maps in Fig. 5.3(b) and Fig. 5.6(b). These observations are in line with the proposed relation between substructure size and transformation sequence in Ref. [17]. During the thermal stage of the coating process, the solute C atoms can further diffuse to the dislocation regions or the boundary regions. These two mechanisms, namely C enrichment in boundary regions and at dislocation cores, are competing with each other. The destinations of the C diffusion, whether to the boundary regions or the vicinity of dislocations, depend on the presence and proximity of these two defect structures. Dislocations are more available in late-formed martensite, and they are probably closer for C atoms, leading to the observed C concentration network. In conclusion, the auto-tempering has limited effect on the C distribution of the martensite in DP steels (both coated and un-coated),

but the influence of thermal treatment during the coating process is significant.

5.4 Conclusions

The crystallography and alloying elements distribution of lath martensite in DP steel has been studied by EBSD, TEM, and APT. The main findings are:

(1) Unlike FM steels, the martensite islands in DP steel do not span the full range of the 24 K-S variants. The measured islands are mostly composed of a single packet with all 6 variants and a small number of minor variants from the same prior austenite grain. The variants in DP steels do not always appear in pairs, as is the case for FM steels. The sub-blocks (variants) seem to only contain one lath, while their shape is blockier than the laths in FM steel.

(2) The examined rolling-induced martensite band consists of multiple packets, out of which four with full 6 variants, while one packet has only 2 blocks.

(3) The element distribution has been measured for early-formed and late-formed martensite in coated commercial steel DPC, martensite in lab-processed uncoated DPL, and FM martensite. The C atoms segregate in all these materials to a different extent, while the substitutional elements are homogenously distributed in all cases. Un-coated DPL and FM specimens show only minor C segregation because the effect of auto-tempering during the quenching process is limited. However, the thermal treatment accompanying the coating process has a significant influence on the C distribution. C atoms re-distribute at either lath boundary regions or at Cottrell atmospheres in the vicinity of the dislocation cores.

(4) The martensite transformation sequence influences the size of substructures of lath martensite and the dislocation densities inside. The early-formed laths are larger with lower dislocation density, whereas the late-formed ones are smaller with higher dislocation density, organized in dislocation networks. From a mechanical perspective, as confirmed by nano-indentation measurement, the larger early-formed laths are softer.

References

[1] R.G. Davies, C.L. Magee, Influence of austenite and martensite strength on martensite morphology, Metallurgical Transactions, 2 (1971) 1939–1947.

[2] G. Krauss, A.R. Marder, The morphology of martensite in iron alloys, Metallurgical Transactions, 2 (1971) 2343–2357.

[3] M.J. Carr, J.R. Strife and G.S. Ansell, An investigation of the effect of austenite strength and austenite stacking fault energy on the morphology of martensite in Fe-Ni-Cr-0.3C alloys, Metallurgical and Materials Transactions A, 9A (1978) 857–864.

[4] T. Maki, Morphology and substructure of martensite in steels, Phase transformation in Steels, Woodhead publishing, (2012).

[5] S. Morito, H. Tanaka, R. Konishi, T. Furuhara, T. Maki, The morphology and crystallography of lath martensite in Fe-C alloys, Acta Materialia, 51 (2003) 1789-1799.

[6] S. Morito, X. Huang, T. Furuhara, T. Maki, N. Hansen, The morphology and crystallography of lath martensite in alloy steels, Acta Materialia, 54 (2006) 5323-5331.

[7] P.M. Kelly, A. Jostsons, R.G. Blake, The orientation relationship between lath martensite and austenite in low carbon, low alloy steels, Acta Metallurgica and Materialia, 38 (1990) 1075-1081.

[8] M.X. Zhang, P.M. Kelly, Accurate orientation relationship between ferrite and austenite in low carbon martensite and granular bainite, Scripta Materialia, 47 (2002) 749-755.

[9] H. Kitahara, R. Ueji, N. Tsuji, Y. Minamino, Crystallographic features of lath martensite in low-carbon steel, Acta Materialia, 54 (2006) 1279-1288.

[10] C.C. Kinney, K.R. Pytlewski, A.G. Khuachaturyan, J.W. Morris Jr., The microstructure of lath martensite in quenched 9Ni steel, Acta Materialia, 69 (2014) 372-385.

[11] F.G. Caballero, A. Garcia-Junceda, C. Capdevila, C.G. de Andres, Evolution of microstructural banding during the manufacturing process of dual phase steels, Material Transactions 47 (2006) 2269-2276.

[12] C.C. Tasan, J.P.M. Hoefnagels, M.G.D. Geers, Microstructural banding effects clarified through micrographic digital image correlation, Scripta Materialia, 62 (2010) 835-838.

[13] A.S. Bor, Effect of pearlite banding on mechanical properties of hot-rolled steel plates, ISIJ International, 31 (1991) 1445-1446.

[14] M.K. Miller, R.G. Forbes, Atom probe tomography, Materials Characterization, 60 (2009) 461-469.

[15] M.K. Miller, Atom probe tomography, Analysis at the atomic level, Springer Science and Business Media, LLC, (2000).

[16] C. Lerchbacher, S. Zinner, H. Leitner, Atom probe study of the carbon distribution in a hardened martensitic hot-work tool steel X38CrMoV5-1, Micron, 43 (2012) 818-826.

[17] L. Morsdorf, C.C. Tasan, D. Ponge, D. Raabe, 3D structural and atomic-scale analysis of lath martensite: Effect of the transformation sequence, Acta Materialia, 95 (2015) 366-377.

[18] M. Abbasi, T.W. Nelson, C.D. Sorensen, L. Wei, An approach to prior austenite reconstruction, Materials Characterization, 66 (2012) 1-8.

[19] S. Morito, Y. Edamatsu, K. Ichinatani, T. Ohba, T. Hayashi, Y. Adachi, T. Furuhara, G. Miyamoto, N. Takayama, Quantitative analysis of three-dimensional morphology of martensite packets and blocks in iron-carbon-manganese steels, Journal of Alloys and Compounds, 577 (2013) 587-592.

[20] H. Ghadbeigia, C. Pinna, S. Cellotto, J.R. Yates, Local plastic strain evolution in a high strength dual-phase steel, Materials Science and Engineering A, 527 (2010) 5026-5032.

[21] S.Y. Zhang, S. Morito, Y. Komizo, Variant selection of low carbon high alloy steel in an

austenite grain during martensite transformation, ISIJ International, 52 (2012) 510-515.

[22] T. Ohmura, T. Hara, T. Tsuzaki, Relations between nanohardness and microstructures in high-purity Fe-C as quenched and quench-tempered martensite, Jounal of Materials Research, 18 (2003) 1465-1470.

[23] C. Du, J.P.M. Hoefnagels, R. Vases, M.G.D. Geers, Block and sub-block boundary strengthening in lath martensite, Scripta Materialia, 116 (2016) 117-121.

[24] E. Keehan, L. Karlsson, H.O. Andren, Influence of carbon, manganese and nickel on microstructure and properties of strong steel weld metal. Part 1—effect of nickel content, Science and Technology of Welding and Joining, 11 (2006) 1-8.

[25] M.J. Santofimia, C. Kwakernaak, W.G. Sloof, L. Zhao, J. Sietsma, Experimental study of the distribution of alloying elements after the formation of epitaxial ferrite upon cooling in a low-carbon steel, Materials Characterization, 61 (2010) 937-942.

[26] A.H. Cottrell, B.A. Bilby, Dislocation Theory of yielding and strain ageing of iron, Proceedings of the Physical Society Section A, 62 (1949) 49-62.

[27] F.G. Caballero, M.K. Miller, S.S. Babu, C. Garcia-Mateo, Atomic scale observations of bainite transformation in a high C silicon steel, Acta Materialia, 55 (2007) 381-390.

[28] S. Lee, K. Park, Prediction of martensite start temperature in alloy steels with different grain sizes, Metallurgical and materials transactions A, 44A (2013) 3423-3427.

[29] D. Blavette, E. Cadel, A. Fraczkiewicz, A. Menand, Three-dimensional atomic-scale imaging of impurity segregation to line defects, Science, 286 (1999) 2317-2319.

[30] J. Wilde, A. Cerezo, G.D.W. Smith, Three-dimensional atomic-scale mapping of a Cottrell atmosphere around a dislocation in iron, Scripta Materialia, 43 (2000) 39-48.

[31] A.W. Coachardt, G. Schoek, H. Wiedersich, Interaction between dislocations and interstitial atoms in body-centered cubic metals, Acta Metallurgica, 3 (1955) 533-537.

[32] C. Zhu, A. Cerezo, G.D.W. Smith, Carbide characterization in low-temperature tempered steels, Ultramicroscopy, 109 (2009) 545-552.

[33] E.V. Pereloma, M.K. Miller, I.B. Timokhina, On the decomposition of martensite during bake hardening of thermomechanically processed transformation-induced plasticity steels, Metallurgical and Materials Transactions A, 39A (2008) 3210-3216.

Chapter 6. Block and sub-block boundary strengthening in lath martensite[1]

Abstract

Well-defined uniaxial micro-tensile tests were performed on lath martensite single block specimens and multi-block specimens with different numbers of block boundaries parallel to the loading direction. Detailed slip trace analyses consistently revealed that the {110}<111> slip system with the highest Schmid factor is activated. Both block and sub-block boundaries act as barriers to dislocation motion, whereby a Hall-Petch like behavior is observed. Sub-block boundary strengthening appears to be only slightly less effective than block boundary strengthening, even though fracture analyses indicate that dislocation motion can cross sub-block boundaries, but not block boundaries.

6.1 Introduction

Lath martensite, the most typical morphology of martensite, has high industrial relevance being the prime constituent that elevates the strength in high strength steels, such as dual-phase steel, transformation-induced plasticity steel and quenching-partitioning steel. For decades, research has been conducted on the strengthening mechanisms of this material, which can be categorized into (i) forest dislocation hardening [1,2], (ii) solid solution hardening by alloying elements [2], (iii) precipitation strengthening, e.g., by carbides [2,3], and most importantly (iv) substructure boundary strengthening [4-12]. Indeed, the hierarchical structure, which shows substructures of packets, blocks and sub-blocks within prior austenite grains, gives lath martensite an abundance of internal boundaries [13]. It was suggested that these boundaries can act as potential barriers to dislocation motion [2,4,5,6].

The mechanical effect of lath martensite boundaries has been investigated in a number of high quality research studies, which can be categorized according to the experimental methodologies used: Morito *et al.* and Zhang *et al.* performed macroscopic tensile tests and concluded that a Hall-Petch relation holds between the yield strength and the averaged block size [4,5]. A more microscopic analysis was carried out by Ohmura *et al.* through nano- and micro-indentation tests, who concluded that the block structure increases the hardness of martensite [6,7], although no differentiation was made between different types of (packet/block/sub-block) boundaries. Shibata *et al.* [8,9] performed micro-bending tests, including two single-block specimen tests. From slip trace analysis from the bending side, where the slip activity is highly inhomogeneous due to the complex loading state, they concluded that the block boundaries are the most effective barriers to dislocation motion. The influence of the sub-block boundaries' presence was, however, not investigated in detail.

Alternatively, lath martensite has been tested by micro-pillar compression tests, including TEM diffraction analysis, by Ghassemi-Armaki *et al.* [10,11], who found that single block specimens show perfect elasto-plastic behavior, whereas multiple block specimens show significant strain hardening. These authors acknowledge, however, that the multiple-block specimens may be jeopardized with one or more packet boundaries, making it difficult to determine whether the hardening is due to the block or packet boundaries. Finally, micro-tension tests on lath martensite, including (single-sided) electron-backscattered diffraction (EBSD) analysis, were conducted by Mine *et al.* [12]. Besides specimens containing multiple packets and even multiple prior austenite grains, also two single-packet specimens were tested with the block boundaries parallel to the loading direction. The authors concluded that block boundaries can be an effective strengthening mechanism, although the contribution of the sub-block boundaries was again not studied. In general, the distinct role of block and sub-block boundaries in terms of the resulting strengthening mechanism remains to be unclear. Therefore, to directly expose the most relevant microscopic deformation mechanisms, reliable experiments under well-defined loading conditions are required, testing single-packet specimens with different numbers of block boundaries as well as single-block specimens with different numbers of sub-block boundaries. The mechanical tests should be accompanied by detailed orientation analyses from at least two sides to confirm the 3D orientation(s) throughout the specimen volume.

6.2 Experiments

In this study, we perform uniaxial micro-tensile tests, using an in-house developed nano-force tensile tester (Fig. 6.1(a,b)) [14], of lath martensite specimens consisting of either a single packet or a single block with a range of block or sub-block boundaries respectively. The methodology involves the following steps: (i) fabrication of a wedge of lath martensite by grinding/polishing/electro-chemical etching, (ii) careful selection of the specimen location at the edge of wedge based on EBSD maps, (iii) focused ion beam milling of micro-tensile specimens with constant thickness, (iv) detailed top- and bottom-side EBSD analysis of each specimen (Fig. 6.2-6.4), (v) uniaxial tensile tests with highly accurate specimen alignment, force- and displacement measurements (Fig. 6.1(a,b,c)) under (vi) *in-situ* optical microscopy enabling microscopic slip trace analysis[15]. We will show that not only block boundaries but also sub-block boundaries play a key role in lath martensite strengthening.

Bulk lath martensite (0.092C-1.68Mn-0.24Si-0.57Cr) out of which the micro-tensile specimens are made was heat treated by homogenization at austenite temperature (first batch, 950 °C for 30 mins; second batch, 1000 °C for 120 mins), followed by water quenching. Most specimens were discarded for analysis because detailed EBSD analysis at both specimen sides showed that the microstructure was not homogeneous over the thickness. For a first batch of specimens, with an average block size smaller than the specimen size, only one specimen was identified with the intended microstructure and desired orientation. Therefore, a second batch of specimens with larger block size was produced with more suitable specimens. The single specimen retained from the first batch is first discussed, since it clearly reveals the role of the block boundary, see Fig. 6.2.
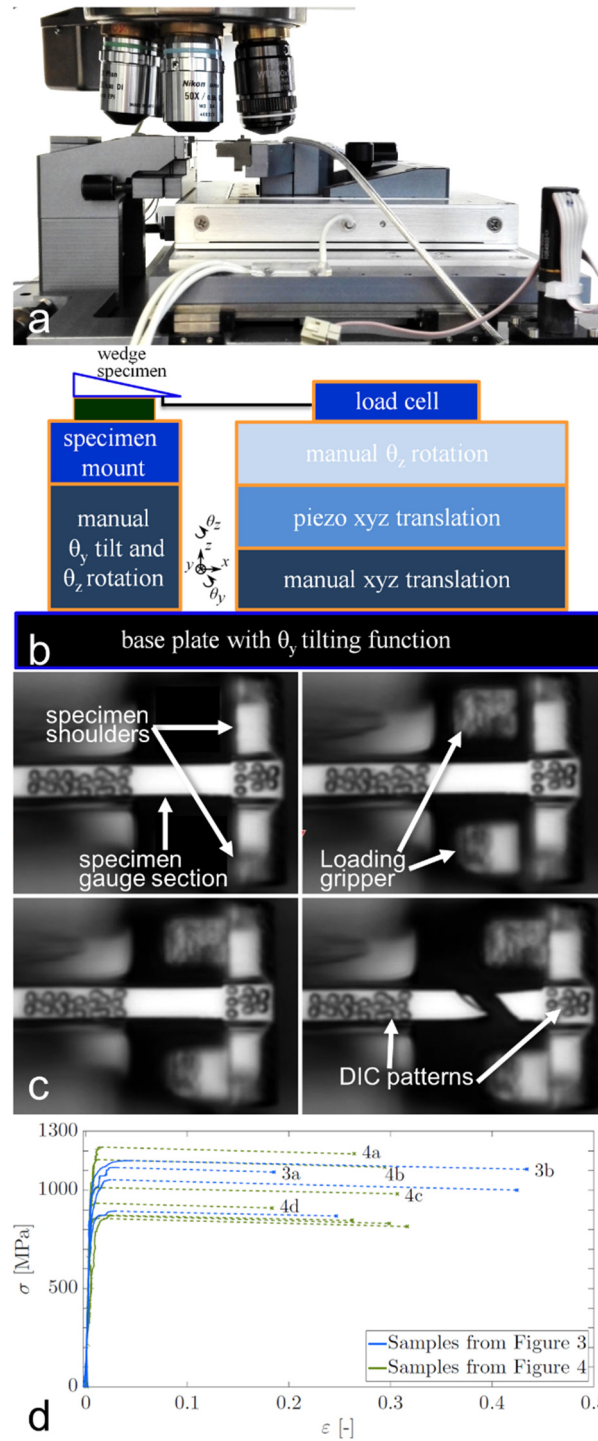
Figure 6.1 (a) The in-house developed nano-force tensile stage under optical profilometer. (b) Schematic drawing of the tensile stage. (c) The testing procedure, in which the load is applied by a 'double-hook' gripper on the specimen shoulders (only the specimen gauge section is in focus). (d) Stress-strain curves of all specimens shown in Fig. 6.3 and Fig. 6.4; the specimens discussed in detail are labeled with their figure numbers. Note that in the unstable deformation regime (dashed line) the applied load decreases slightly.

6.3 Results and discussion

The EBSD maps of the top and bottom sides (Fig. 6.2(a,b)) confirm that the block boundary is approximately in the middle of the specimen and runs vertical through the thickness. The pole figures of the top and bottom sides are shown in Fig. 6.2(e,f), which demonstrate the uniformity of the microstructure within the specimens. The block boundary was confirmed to be a high angle boundary with ~60 degrees misorientation. From the austenite-to-martensite orientation relationship it is known that boundaries inside packets form at a {111} prior austenite plane, i.e. parallel to a {110} martensite plane, therefore, the dots (red circles) on the peripheral in the {110} plots in Fig. 6.2(e,f) confirm that the block boundary is perpendicular to the specimen surface. Black circles highlight the favorable slip direction and slip plane of the {110}<111> slip systems. The marked slip traces (dotted lines) in Fig. 6.2(d) is in good agreement with the favorable slip systems, considering the significant crystal rotation upon fracture. More convincing evidence for single slip system activation is shown below for the single block specimens. Interestingly, the fracture surfaces join exactly at the block boundary in the middle, where the slip systems are interrupted. This is the first direct evidence that block boundaries in lath martensite act as barriers to dislocation motion for the case where the activated slip system is crossed by a block boundary.
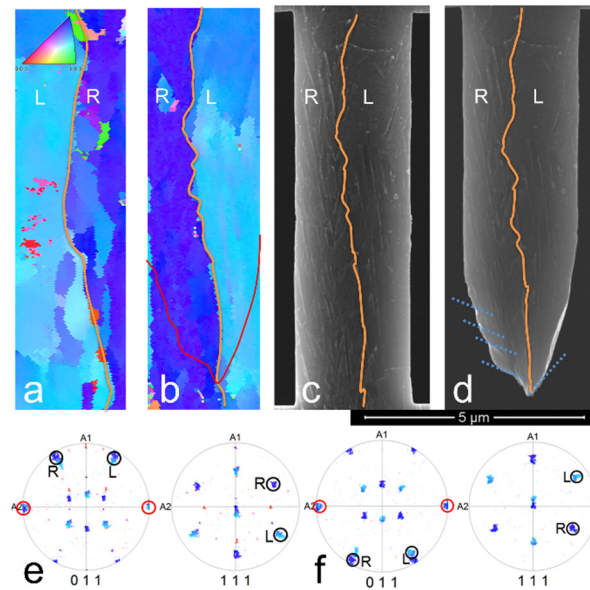
Figure 6.2 EBSD maps of a bi-block specimen from front (a) and backside (b). Backside SEM image before (c) and after (d) fracture. (e,f) the {110} and {111} pole figures of the front side and backside respectively. The circles indicate the observed slip systems of both the left block (L) and the right block (R).

From the second batch of specimens, a series of specimens with different configurations of boundaries are produced and tested: specimens with no block boundaries (i.e. single block specimens), one parallel block boundary and multiple parallel block boundaries. In Fig. 6.3(a,b), two examples of specimens with multiple block boundaries are shown. In the case of few block

boundaries (Fig. 6.3(a)), with large boundary-free regions at the specimen sides, the fracture propagates from both specimen sides and arrests at the first block boundary, similar to the single block boundary case. However, between the two block boundaries, the slip activity is more complex due to the induced loading constraints, resulting in a jagged fracture surface. The same phenomenon is also observed when the boundary-free regions at the specimen sides are small, due to the presence of many block boundaries (Fig. 6.3(b)). Due to the fact that the dislocations cannot propagate through block boundaries, a zig-zag fracture surface is formed with multiple peaks, again in agreement with the block boundaries. The identified slip systems of both samples are in line with the ones marked with corresponding colors of the blocks in the pole figures (Fig. 6.3(c,d)).
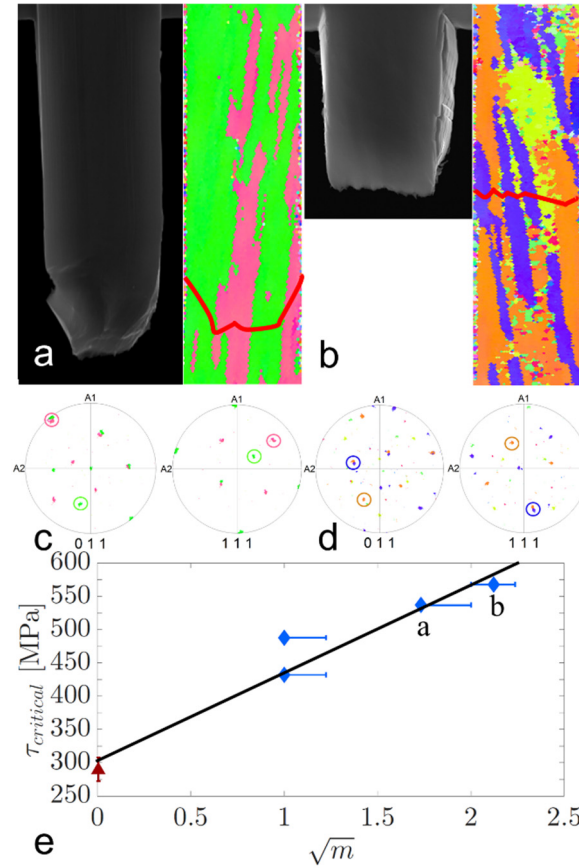
Figure 6.3 (a,b) The fracture surface (left) and EBSD map (right) for both specimens marked in (e). The length of undeformed samples is 9μm. Red curves mark the fracture traces in the EBSD maps. (c,d), {110} and {111} pole figures of sample a and b respectively, (e) $\tau_{critical}$ versus $\sqrt{m}$, where the error bars reflect (an estimation of) the uncertainty in the number of block boundaries m (same for n in Fig. 6.4(e)). The data point at $\sqrt{m} = 0$ in red corresponds to the strength without block and sub-block boundaries as obtained from the offset in Fig. 6.4(e).

To analyze the strengthening caused by block boundaries, Fig. 6.3(e) shows the critical stress, $\tau_{critical}$, versus the square root of the average number of block boundaries, $\sqrt{m}$ where m is the average number of block boundaries observed at both sides. $\tau_{critical}$ is calculated by multiplying the highest Schmid factor of the largest block with the tensile strength, which is

used as some specimens localize before 2% strain offset.

Interestingly, Fig. 6.3(e) shows that $\tau_{critical}$ increases linearly with $\sqrt{m}$. This observation provides direct microscopic evidence of a Hall-Petch type relationship for block boundaries, as already suggested in [4,5]. Note that only clean multi-block specimens have been included in Fig. 6.3(e), i.e. all of these specimens are free of sub-block boundaries, except for the specimen with the lowest $\tau_{critical}$ where one sub-block boundary is observed only on the top-right side. This specimen would have had an even lower $\tau_{critical}$ without this sub-block boundary. Therefore, the observed strengthening cannot be attributed to the presence of sub-block boundaries, but must be caused by the block boundaries. The slope of the linear fit in Fig. 6.3(e) is 132±10 [MPa], including all inaccuracies. This value cannot directly be compared to Hall-Petch constants for bulk lath martensite, because the fraction of 'grains' in our micro-specimens that are cut off at the side by the free surface is significant.

Next, the strengthening effect of sub-block boundaries is investigated. Two examples of single block specimens from the same packet and with the same sub-blocks are shown in Fig. 6.4(a,b). The misorientation between the sub-blocks is ~8 degrees, i.e. a small angle boundary. Both fracture surfaces and slip traces are continuous across the sub-block boundary and no difference can be observed in the two sub-blocks due to the small misorientation. Both samples in Fig. 6.4(a,b) reveal the same slip trace and fracture surface, which demonstrates the reproducibility of this testing method as well as the consistent activation of micro-mechanical mechanisms. The {110}<111> system with the highest Schmid factor is activated in both sub-blocks and marked with black circles in the pole figures.

Two other single block specimens are shown in Fig. 6.4(c) and Fig. 6.4(d). Again, analysis shows that the slip system of the {110}<111> family with the highest Schmid factor is again active. The slip traces are nearly equivalent in the two sub-blocks, while the fracture surfaces cross the sub-block boundaries. The specimen in Fig. 6.4(d) contains more sub-block boundaries in the upper part. Perhaps not surprisingly, the specimen fractures at the bottom part where it is less heterogeneous, which confirms the sub-block boundary strengthening mechanism.

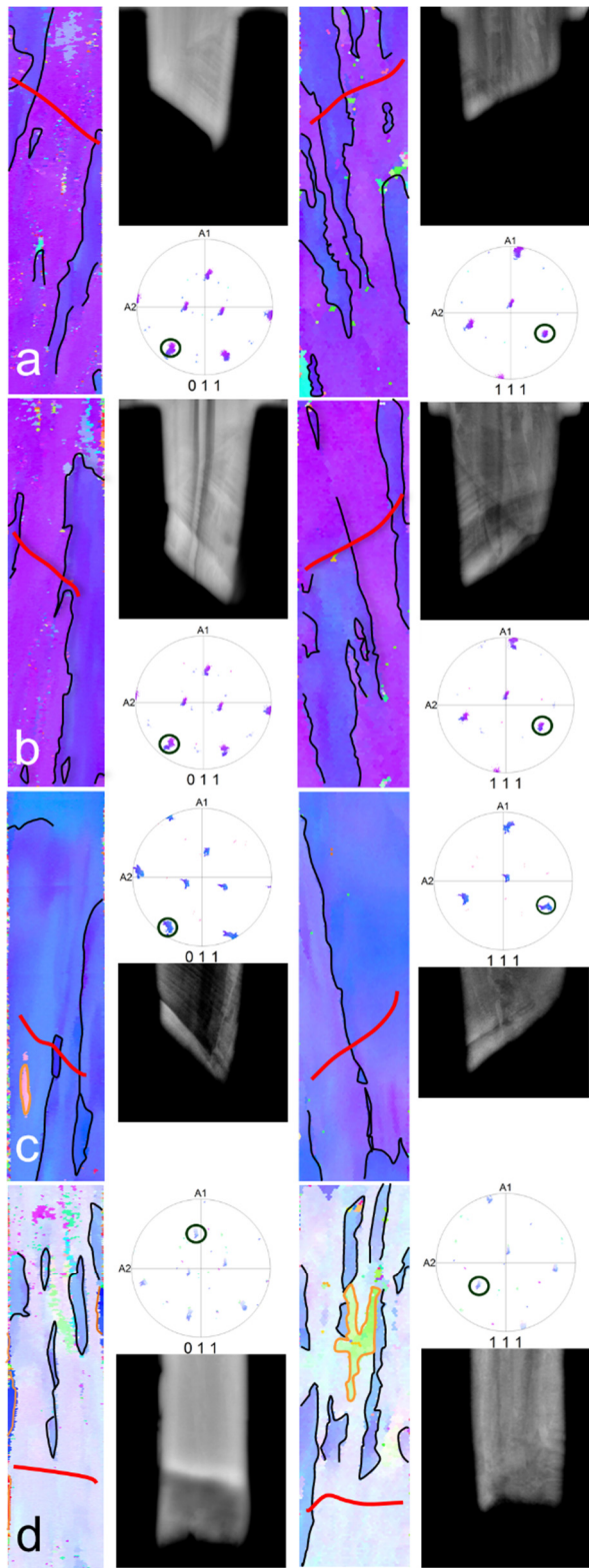*Figure 6.4 (a-d) EBSD maps and BSE fracture images of the front (left) and back (right) side and the {110} and {111} pole figures for each specimen, marked in (e). The length of undeformed samples is 9μm. (e) $\tau_{critical}$ versus the square root of number of sub-block boundaries $\sqrt{n}$. The fracture traces and sub-block boundaries are marked with, respectively, red and black curves in the EBSD maps.*
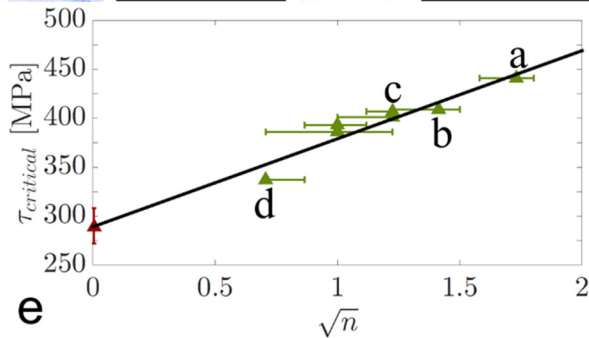
For the single block specimens, $\tau_{critical}$ is plotted as a function of the square root of the number of sub-block boundaries, n, in Fig. 6.4(e), where n is calculated similarly to m in Fig. 6.3(e). The main difference between the four specimens shown in Fig. 6.4 lies in the number of sub-block boundaries crossed by the fracture surface. The more sub-block boundaries crossed by the fracture surface, the stronger the specimen are. Similar to the strengthening mechanism of block boundaries, $\tau_{critical}$ increases linearly with $\sqrt{n}$, with a slope of 90±10 MPa, which suggests a Hall-Petch type relationship also for sub-block boundary strengthening. Although the slopes of Fig. 6.3(e) and Fig. 6.4(e) are subject to experimental and microstructural uncertainties, the slightly smaller slope in Fig. 6.4(e) indicates that strengthening by sub-block boundaries is only somewhat less effective. This in-depth uniaxial tension analysis directly proves that the strengthening effect of sub-block boundaries is highly important, which is in sharp contrast to the statement in Ref. [8] that the sub-block boundaries have a negligible contribution to the macroscopic strength of lath martensite.

Interestingly, yet qualitative, *in-situ* TEM observations in [16] showed that dislocations pile up at a low angle boundary followed by transmission through it. This may explain why (almost) all fracture surfaces of the single-block specimens show a single straight fracture surface spanning the complete cross-section. It was also suggested in [16], from the sudden disappearance of dislocations at a block boundary, that dislocations 'reflect' and then glide along the high-angle boundaries (to the free surface). If dislocations can indeed glide along a block boundary instead of cutting through the boundary, this may explain why the fracture surfaces of two adjacent blocks join exactly at the block boundary, as shown most clearly in Fig. 6.2, and why the fracture surface for multi-block specimens is jagged.

6.4 Conclusions

In summary, uniaxial micro-tensile tests were performed on lath martensite specimens with different numbers of block boundaries parallel to the loading direction and single-block specimens with different numbers of sub-block boundaries. For the single-block specimens, the observed slip traces match the {110}<111> slip system with the highest Schmid factor. Both the block and sub-block boundaries act as a barrier for dislocation motion, clearly strengthening the material. A Hall-Petch type relationship was found between $\tau_{critical}$ and the number of boundaries, and the strengthening effect of sub-block boundaries appears to be only slightly less effective as that of block boundaries. For multi-block specimens, the fracture surface joins at the block boundary, indicating that the fracture cannot propagate across block boundaries. This is in contrast to sub-block boundaries for which a single straight fracture surface over the cross-section is consistently identified.

References

[1] S. Takaki, K. Ngo-huynh, N. Nakada, T. Tsuchiyama, Strengthening mechanism in ultra low carbon martensitic steel, ISIJ International, 52 (2012) 710-716.

[2] G. Krauss, Martensite in steel: strength and structure, Materials Science and Engineering A, 273-275 (1999) 40-57.

[3] T. Ohmura, T. Hara, K, Tsuzaki, Evaluation of temper softening behavior of Fe–C binary martensitic steels by nanoindentation, Scripta Materialia, 49 (2003) 1157-1162.

[4] S. Morito, H. Yoshida, T. Maki, X. Huang, Effect of block size on the strength of lath martensite in low carbon steels, Materials Science and Engineering A, 438-440 (2006) 237-240.

[5] C. Zhang, Q. Wang, J. Ren, R. Li, M. Wang, F. Zhang, K. Sun, Effect of martensitic morphology on mechanical properties of an as-quenched and tempered 25CrMo48V steel, Materials Science and Engineering A, 534 (2012) 339-346.

[6] T. Ohmura, T. Hara, K. Tsuzaki, Relationship between nanohardness and microstructures in high-purity Fe–C as-quenched and quench-tempered martensite, Journal of Materials Research, 18 (2003) 1465-1470.

[7] T. Ohmura, T. Hara, K, Tsuzaki, Evaluation of temper softening behavior of Fe–C binary martensitic steels by nanoindentation, Scripta Materialia, 49 (2003) 1157-1162.

[8] A. Shibata, T. Nagoshi, M. Sone, S. Morito, Y. Higo, Evaluation of the block boundary and sub-block boundary strengths of ferrous lath martensite using a micro-bending test, Materials Science and Engineering A, 527 (2010) 7538-7544.

[9] A. Shibata, T. Nagoshi, M. Sone, S. Morito, Y. Higo, Micromechanical characterization of deformation behavior in ferrous lath martensite, Journal of Alloysand Compounds, 577 (2013) 555-558.

[10] H. Ghassemi-Armaki, P. Chen, S. Bhat, S. Sadagopan, S. Kumar, A. Bower, Microscale-calibrated modeling of the deformation response of low-carbon martensite, Acta Materialia, 61 (2013) 3640-3652.

[11] H. Ghassemi-Armaki, R. Maaß, S.P. Bhat, S. Sriram, J.R. Greer, K.S. Kumar, Deformation response of ferrite and martensite in a dual-phase steel, Acta Materialia, 62 (2014) 197-211.

[12] Y. Mine, K. Hirashita, H. Takashima, M. Matsuda, K. Takashima, Micro-tension behaviour of lath martensite structures of carbon steel, Materials Science and Engineering A, 560 (2013) 535-544.

[13] S. Morito, H. Tanaka, R. Konishi, T. Furuhara, T. Maki, The morphology and crystallography of lath martensite in Fe-C alloys, Acta Materialia, 51 (2003) 1789-1799.

[14] L.I.J.C. Bergers, J.P.M. Hoefnagels, M.G.D. Geers, On-wafer time-dependent high reproducibility nano-force tensile testing, Journal of Physics D: Applied Physics, 47 (2014) 495306.

[15] C. Du, J.P.M. Hoefnagels, L.I.J.C. Bergers, M.G.D. Geers, submitted for publication.

[16] T. Ohmura, A.M. Minor, E.A. Stach, J.W. Morris, Dislocation–grain boundary interactions in martensitic steel observed through in situ nanoindentation in a transmission electron microscope, Journal of Materials Research, 19 (2004) 3626-3632.

Chapter 7. Plasticity of lath martensite by sliding of substructure boundaries[1]

Abstract

Well-defined uniaxial micro-tensile tests were performed on lath martensite with different types of substructure boundaries (block, sub-block and lath boundaries) tilted with respect to the loading direction. A characteristic deformation mechanism of lath martensite is hereby identified, i.e. sliding along the substructure boundaries. This boundary sliding can occur at all types of boundaries at relatively low stresses. Internal boundaries not only strengthen lath martensite, as well established in literature, but under favorable orientations also mitigate plastic deformation. The overall plastic deformation results from the competition of crystallographic slip with boundary sliding.

7.1 Introduction

Lath martensite, the most typical morphology of martensite, is the prime constituent that elevates the strength in high strength steels. It has high industrial relevance as it is present in e.g. dual-phase (DP) steel, transformation-induced plasticity steel, and quenching-partitioning steel. Lath martensite has a complex hierarchical microstructure in which a prior austenite grain is divided into packets, packets subdivided into blocks, and blocks into sub-blocks each containing multiple laths [1]. This leads to many internal boundaries, which influence the mechanical properties of lath martensite strongly [2].

Lath martensite mechanics has been studied to limited extent, in part due to the complexity of small-scale experimentation. From macroscopic tensile tests, Morito et al. and Zhang et al. found that a Hall-Petch relation holds between the yield strength and block size [3,4]. From nano- and micro-indentation tests, Ohmura et al. concluded that the block structure increases the hardness [5,6]. From micro-bending tests, Shibata et al. [7,8] reported that block boundaries are the most effective barriers to dislocation motion, which was also concluded by Ghassemi-Armaki et al. and Mine et al. from, respectively, micro-compression and micro-tension tests [9-11]. Recently our micro-tensile tests on well-defined multi-block and single-block specimens showed that sub-block boundary strengthening is almost equally important as block boundary strengthening [12].

In general, research mentioned above focused on the strengthening effects of lath martensite boundaries caused by their interaction with dislocations during plastic deformation. Yet, plasticity was also found to occur parallel to the (tilted) lath boundaries, although at large strains slip cut across boundaries [13,14]. The former may be related to the Kurdjumov-Sachs transformation orientation relationship through which two BCC slip systems in each martensite

lath are closely aligned to the neighboring boundary. Additionally, in lath-martensite-containing engineering steels, the small martensite islands typically do not contain all variants, while a single (tilted) boundary often reach across the small martensite ligaments, which are highly relevant for the overall mechanics [15,16]. Crystallographic slip does not cross the boundary to accommodate ligament stretching, especially because two slip systems are aligned with each boundary. Consequently, the role of internal boundaries may differ substantially from the strengthening mechanism suggested in literature.

This work studies the micro-mechanical role of substructure boundaries in lath martensite, in configurations where crystallographic slip is not forced to cut across the boundaries. Therefore, in-situ uniaxial micro-tensile tests are performed on single-packet specimens containing different types of boundaries that are all tilted at approximately 45° to the loading direction, simulating the loading of tilted boundary regions in fully martensitic steel and small ligaments in martensite islands in DP steels. A new deformation micro-mechanism other than crystallographic slip will be revealed.

7.2 Experiments

The lath martensite specimens (0.092C-1.68Mn-0.24Si-0.57Cr) were produced by 2-hour heating at 1000°C, followed by water quenching, yielding large packets well suited for fabrication of single-packet specimens. The test procedure involves [18]: (i) wedge fabrication from lath martensite sheet by grinding/polishing/electro-chemical etching, (ii) careful selection of specimen locations at the wedge tip using large-area EBSD, (iii) accurate focused-ion-beam (FIB) milling of micro-tensile specimens with constant ($3.0\times2.5\mu m^2$) cross-section (Fig. 7.1(d)), (iv) detailed top- and bottom-side EBSD analysis of each specimen, enabling Schmid factor analysis (Table 7.1), (v) uniaxial tensile tests with highly accuracy in specimen alignment (<0.1 mrad angular alignment and near-perfect co-linearity) and force (from 0.07 μN to 250 mN) and displacement (<6 nm reproducibility) measurement (Fig. 7.1(a-c)) [18], under (vi) in-situ optical microscopy enabling microscopic slip trace analysis.

7.3 Results and discussion

In all EBSD maps, the type of boundaries (block or sub-block) was analyzed here from the boundary misorientation (respectively $\Delta\theta$>12°, 5°<$\Delta\theta$<12°) and is consistently marked with different line colors: orange and black for, respectively, block and sub-block boundaries. All laths within one sub-block have almost identical orientation, making their boundaries invisible in EBSD maps. For the first sample batch, the top and bottom sides were milled flat to yield the best EBSD quality, at the expense of invisible topographic contrast of the lath boundaries due to etching-induced surface traces. Therefore, a second batch of specimens was fabricated without topside milling, for which the lath boundaries are identified. It was confirmed that (almost all) lath-, sub-block-, and block-boundaries in one packet are (approximately) parallel.
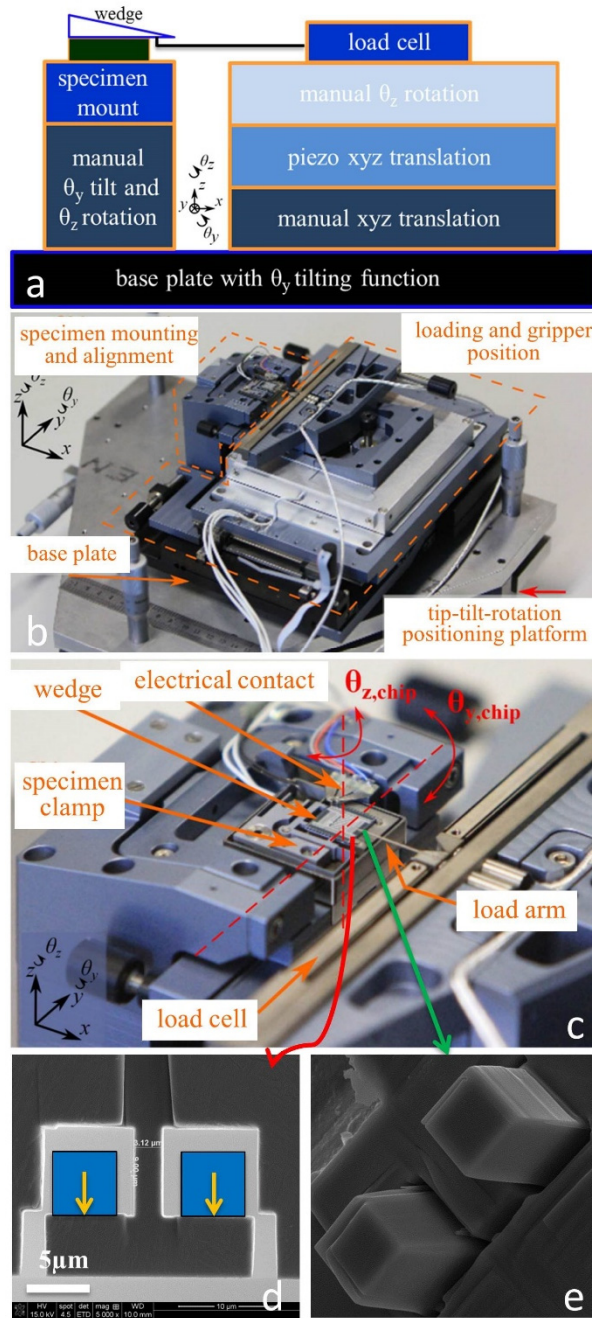
Figure 7.1 (a,b) A schematic drawing [12] and real image [18] of the nano-force tensile stage, with the specimen on the left and loading block on the right, (c) zoom of the load cell and specimen holder, (d) top view of the micro-tensile specimen at the wedge tip, with the two-teeth gripper drawn in blue, and (e) detailed zoom of the two-teeth gripper at the end of the load arm.

Starting with the second batch, Fig. 7.2 shows the topsides of two samples both before and after plastic deformation and the {110} and {111} inverse pole figures of the undeformed state. Figure 7.2(a1-6) shows a single-packet sample, of predominantly one block, with block boundaries and sub-block boundaries that are (i) tilted to the loading direction, (ii) aligned with one (110) martensite plane corresponding to a (111) prior-austenite plane, and (iii) roughly perpendicular to the specimen surface (indicated by a red circle at the peripheral of {011} pole

figure). The slip system with the highest Schmid factor, indicated by the red circles in Fig. 7.2(a5) and Fig. 7.2(a6), is parallel to the boundaries. As this favorable slip system needs not to cross the boundaries, one would expect all plastic slip to occur inside the laths. However, slip seems not to occur between the boundaries. Instead, clear steps occur exactly at the boundaries, as clearly observed from the zoom of the edge of the deformed specimen in Fig. 7.2(a4). Apparently, another deformation mechanism is active in lath martensite, responsible for most global deformation, i.e. relative sliding of laths at the boundaries. However, close inspections of these and other specimens do reveal some small slip steps in interior lath regions corresponding to conventional plasticity on favored slip systems. Consequently, plastic deformation is mitigated by a competition between two deformation mechanisms, namely boundary sliding and conventional in-lath dislocation motion. The fracture surface confirms these observations as it is composed of three parts (white dashed line in Fig. 7.2(a1,2)), i.e. the fracture surface propagates along a sub-block boundary (right edge), then continues along part of the block boundary (middle), and finally cuts through the adjacent lath (left edge). In addition, Fig. 7.2(a3) shows that the boundaries close to the fracture surface have rotated significantly (~20°) towards the most favorable orientation, which is similar to the well-known crystallographic lattice rotation in single-crystal specimens due to constrained boundary conditions [19]. Here, boundary sliding is accompanied with in-lath crystallographic slip to accommodate the constrained gripper movement in horizontal direction. Therefore, crystallographic slip promotes boundary sliding by rotating the boundaries to obtain a higher resolved shear stress.

Figure 7.2(b1–6) shows the plastic deformation of a two-block specimen with multiple block and sub-block boundaries tilted to the loading direction. Again, steps are observed in the deformed state of the specimen (Fig.7.2(b3,4)). Corresponding positions where sliding happens before and after deformation, are indicated by arrows, which shows that sliding occurs exactly at a block and sub-block boundary. The favored slip system is again parallel to the block boundaries (red circles in Fig. 7.2(b5,6)). Consequently, the plastic deformation mechanism is a competition between the dislocation slip and boundary sliding. Dislocation slip could activate anywhere inside the crystals. However, similar to specimen 2a, steps are found exactly at the boundary location, and careful analysis of the side surface shape revealed that crystallographic slip occurring in-between the boundaries is, at best, very limited. Hence, this specimen is predominantly deformed by block boundary sliding. Again, rotation of the blocks results from the constrained boundary conditions. Note that the boundary sliding mechanism is not caused by concentration of FIB-induced gallium ions at the boundaries [20], because the top surface was never subjected to FIB milling, while Fig. 7.2(b3) clearly shows boundary sliding over the complete top surface, and probably through the whole specimen volume. Regarding the fracture surface, the right upper part appears to run along a block boundary and its lower part along a lath or sub-block boundary (white dashed line in Fig. 7.2(b1,2)).
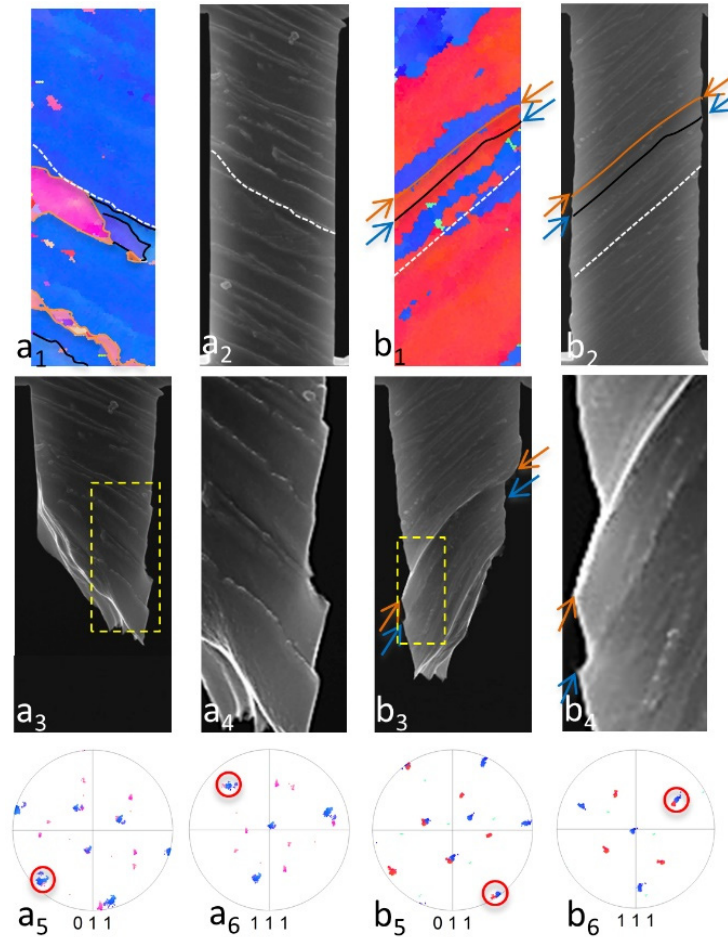
Figure 7.2 Two 9 µm-long specimens with tilted boundaries to the loading direction shown with inverse pole figure orientation map (a1, b1), SEM pictures before loading (a2, b2) and after facture (a3, b3) together with a zoom (yellow frame) of the fractured specimens (a4, b4). The red circles in the {110} (a5, b5), {111} (a6, b6) pole figures indicate the favored slip system. Block and sub-block boundaries are marked with orange and black lines respectively; the fracture surface with a white dotted line. The many lath boundaries are not marked. The arrows in b1–b4 indicate sliding boundaries.

Table 7.1 Schmid factor analysis based on the block's Euler angles (φ1, Φ, φ2). Because most specimens localize before 2% strain offset, the "critical stress", τcritical, is calculated by multiplying the ultimate tensile strength (UTS) with the block's highest Schmid factor (SF).

Spec. No.	Fig.7.2(a)		Fig.7.2(b)		Fig.7.3(a)		Fig.7.3(b)		Fig.7.3(c)
Block color	Pink	Blue	Red	Blue	Red	Blue	Red	Blue	Purple
$(\varphi_1, \Phi, \varphi_2)$	(11,23,309)	(191,52,141)	(314,9,55)	(142,57,234)	(254,9,100)	(10,51,316)	(26,6,335)	(123,47,219)	(71,35,307)
SF	0.45	0.49	0.44	0.46	0.45	0.47	0.43	0.47	0.48
UTS/MPa	785		873		860		981		871
$\tau_{critical}$ /MPa	353	385	384	402	387	404	422	461	418

Figure 7.3 shows three examples from the first-batch specimens (with invisible lath boundaries) with clear fracture surfaces, all of which having boundaries again tilted to the loading.

Compared to Fig. 7.2, no sliding steps are observed in the deformed state of the specimen, however, for all three specimens the fracture surface clearly propagates along (a part of) one of the lath martensite substructure boundaries.

An example of a multi-block specimen is shown in Fig. 7.3(a). Careful analysis suggests that the fracture surface runs along the sub-block boundary (inside the blue block), which is roughly at 45°. The Schmid factors of the most favorably oriented slip systems in both the blue and red blocks are high (SF=0.47 and 0.45, see Table 7.1) which means that crystallographic slip should be relatively easily activated. Especially for the blue block, for which the favored slip system is parallel to the fracture surface and which contains a large through-thickness region without sub-block boundaries, one would expect crystallographic slip to be activated throughout the block [12]. However, no slip is observed in the blue block, neither in the red block, whereas all deformation and fracture is localized at the sub-block boundary. This observation is especially surprising because (i) the fracture surface propagates from the gauge section (which stops at the bottom side of Fig. 7.3(a2–a5)) into the much wider gripping part of the specimen, where the resolved shear stress is significantly decreased, and (ii) the resulting fracture surface is wavy rather than straight, whereas a straight fracture is consistently observed for single-block crystallographic slip [12]. These observations provide a strong indication that, for this particular configuration, the boundary sliding mechanism is activated (considerably) more easily than crystallographic slip.

In the case of specimen 3b, the gauge section consists almost of one (blue) block, although a small, second (red) block is present in the center. The fracture position is located exactly at one of the block boundaries, indicated by the arrow in the EBSD map. More precisely, the fracture surface slides partially along this block boundary instead of propagating through intra-block regions. This again confirms that under favorable orientation boundary sliding is more easily activated than crystallographic slip.

Figure. 7.3(c) shows a single-block specimen for which the bottom side is relatively free of boundaries, while the topside shows more sub-block boundaries. In this case, the most favorable slip system (SF=0.48) does not align with the fracture surface. The fracture surface cuts through, respectively, one and two sub-block boundaries on the top and bottom side of the specimen. Careful analysis of the slip plane orientation with the boundary morphology shows a number of regions where crystallographic slip might have occurred by cutting through less (one or two) sub-block boundaries. Hence boundary sliding is again easier activated than crystallographic slip. In addition, a high number of slip traces are observed on the bottom side, which clearly shows that boundary sliding and crystallographic slip are in competition.

These results provide evidence that boundary sliding can be easily activated in lath, sub-block, and block boundaries, and probably also in packet and prior-austenite boundaries. The question remains whether there exists a difference between these boundaries. Because all substructure boundaries inside a packet are approximately parallel, the resolved shear stress on them should be nearly equal as well. Even though in most specimens sliding happens only at a specific type of boundary, all types of boundaries were revealed as candidates for sliding,

which seem statistically determined. Considering all tested specimens, including all ~20 specimens with tilted boundaries not shown here, no significant difference was observed between different boundaries regarding their probability for sliding. This is nicely illustrated in Fig. 7.2(a) where lath, sub-block and block boundary sliding co-occur, with fracture resulting from a synergy of the latter two.
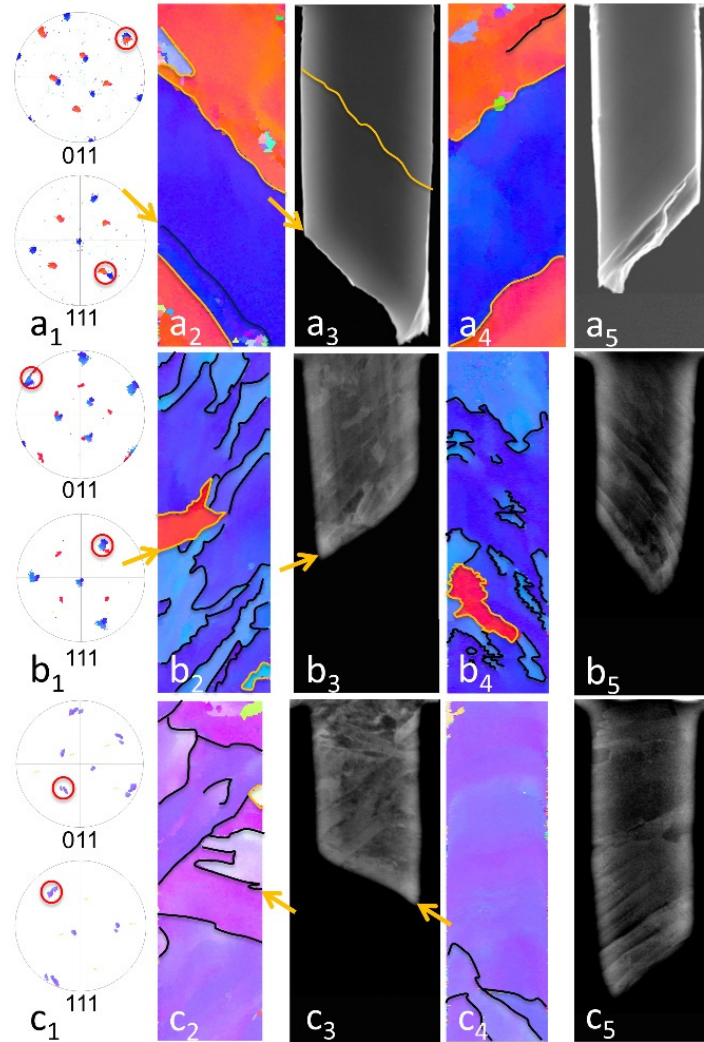
Figure 7.3 Three 9 μm-long specimens with substructure boundaries tilted to the loading direction, shown with {011} and {111} pole figures of the topside (a1, b1, c1) with red circles indicating the most favorable slip system(s), inverse pole figure orientation maps of top (a2, b2, c2) and bottom (a4, b4, c4) side, and SEM pictures after fracture of top (a3, b3, c3) and bottom (a5, b5, c5) side. Yellow arrows indicate the fracture surfaces.

All samples show that, for boundaries titled to the loading, boundary sliding is an important deformation mechanism that is often favored over crystallographic slip. It was shown earlier [12] that for configurations where boundary sliding is prohibited by a low resolved shear stress due to unfavorable orientation, e.g. boundary orientation parallel to the loading direction, the plastic deformation of lath martensite is predominantly carried by crystallographic slip within laths. In that case, the boundaries obstruct or even block crystallographic slip, resulting in

boundary strengthening. It is therefore concluded that boundary sliding and crystallographic slip are the main mechanisms of lath martensite deformation.

Finally, interesting macro-tensile tests of lath martensite were performed in [13,14], from which it was concluded that, at small strains, the deformation is carried by crystallographic slip parallel to the lath boundaries ('the Burger's vector in the in-lath plane'), while at high strain, the deformation mode shifts to crystallographic slip at high angle to the boundaries. Considering the limitations of observation which prevented direct observation of the very local plastic deformations, it is plausible that the 'in-lath plane' crystallographic slip along tilted boundaries may in fact have been the same boundary sliding mechanism that is observed here. This suggests that boundary sliding also occurs in bulk martensite.

The question remains what causes the boundary sliding mechanism. The substructure boundaries often contain so-called 'inter-lath retained austenite' films between the laths, even in lath martensite with low carbon (e.g. in [21]). It is also argued that martensite transformation is never complete [22]. Recently, the impact of ~10 nm-wide inter-lath retained austenite films on the global response of martensite was investigated using crystal plasticity simulations [23]. Interestingly, because three FCC slip systems in austenite films are aligned with the boundary, slip in the films should occur at lower resolved shear stress than slip in the neighboring laths, i.e. "the austenite film acts like a "greasy" plane on which the stiffer laths can slide" [23]. At a larger scale of observation, however, slip in the ultra-thin austenite films would appear as boundary sliding, which would explain the observed mechanism.

7.4 Conclusions

In summary, uniaxial micro-tensile tests were performed on lath martensite specimens from single packets with different types of substructure boundaries tilted to the loading direction. Clear evidence was provided that boundary sliding is an important mechanism for lath martensite deformation. In most cases, boundary sliding constitutes the dominant deformation micro-mechanism. However, boundary sliding co-exists with crystallographic slip both contributing to the overall deformation. Boundary sliding can be activated in all types of tested boundaries: lath, sub-block, and block boundaries.

References

[1] S. Morito, H. Tanaka, R. Konishi, T. Furuhara, T. Maki, The morphology and crystallography of lath martensite in Fe-C alloys, Acta Materialia, 51 (2003) 1789-1799.

[2] G. Krauss, Martensite in steel: strength and structure, Materials Science and Engineering A, 273-275 (1999) 40-57.

[3] C. Zhang, Q. Wang, J. Ren, R. Li, M. Wang, F. Zhang, K. Sun, Effect of martensitic morphology on mechanical properties of an as-quenched and tempered 25CrMo48V steel, Materials Science and Engineering A, 534 (2012) 339-346.

[4] S. Morito, H. Yoshida, T. Maki, X. Huang, Effect of block size on the strength of lath martensite in low carbon steels, Materials Science and Engineering A, 438-440 (2006) 237-240.

[5] T. Ohmura, T. Hara, K. Tsuzaki, Relationship between nanohardness and microstructures in high-purity Fe–C as-quenched and quench-tempered martensite, Journal of Materials Research, 18 (2003) 1465-1470.

[6] T. Ohmura, T. Hara, K, Tsuzaki, Evaluation of temper softening behavior of Fe–C binary martensitic steels by nanoindentation, Scripta Materialia, 49 (2003) 1157-1162.

[7] A. Shibata, T. Nagoshi, M. Sone, S. Morito, Y. Higo, Evaluation of the block boundary and sub-block boundary strengths of ferrous lath martensite using a micro-bending test, Materials Science and Engineering A, 527 (2010) 7538-7544.

[8] A. Shibata, T. Nagoshi, M. Sone, S. Morito, Y. Higo, Micromechanical characterization of deformation behavior in ferrous lath martensite, Journal of Alloys and Compounds, 577 (2013) 555-558.

[9] H. Ghassemi-Armaki, P. Chen, S. Bhat, S. Sadagopan, S. Kumar, A. Bower, Microscale-calibrated modeling of the deformation response of low-carbon martensite, Acta Materialia, 61 (2013) 3640-3652.

[10] H. Ghassemi-Armaki, R. Maaß, S.P. Bhat, S. Sriram, J.R. Greer, K.S. Kumar, Deformation response of ferrite and martensite in a dual-phase steel, Acta Materialia, 62 (2014) 197-211.

[11] Y. Mine, K. Hirashita, H. Takashima, M. Matsuda, K. Takashima, Micro-tension behaviour of lath martensite structures of carbon steel, Materials Science and Engineering A, 560 (2013) 535-544.

[12] C. Du, J.P.M. Hoefnagels, R. Vaes, M.G.D. Geers, Block and sub-block boundary strengthening in lath martensite, Scripta Materialia, 116 (2016) 117-121.

[13] M. Michiuchi, S. Nambu, Y. Ishimoto, J. Inoue, T. Koseki, Relationship between local deformation behavior and crystallographic features of as-quenched lath martensite during uniaxial tensile deformation, Acta Materialia, 57 (2009) 5283-5291.

[14] S. Nambu, M. Michiuchi, Y. Ishimoto, K. Asakura, J. Inoue, T. Koseki, Transition in deformation behavior of martensitic steel during large deformation under uniaxial tensile loading, Scripta Materialia, 60 (2009) 221-224.

[15] H. Ghadbeigi, C. Pinna, S. Celotto, J.R. Yates, Local plastic strain evolution in a high strength dual-phase steel, Materials Science and Engineering A, 527(2010) 5026-5032.

[16] J.P.M. Hoefnagels, C.C. Tasan, F. Maresca, F.J. Peters, V.G. Kouznetsova, Retardation of plastic instability via damage-enabled micro-strain delocalization, Journal of Materials Science, 50 (2015) 6882-6897.

[17] C. Du, J.P.M. Hoefnagels, L.I.J.C. Bergers, M.G.D. Geers, Uni-axial nano-force tensile test of individual constituents from bulk material, submitted (2016).

[18] L.I.J.C. Bergers, J.P.M. Hoefnagels, M.G.D. Geers, Characterization of time-dependent

anelastic microbeam bending mechanics, Journal of Physics D: Applied Physics, 47 (2014) 3626-3632.

[19] R.E. Smallman, R.J. Bishop, Modern physical metallurgy and materials engineering, sixth ed., Butterworth Heinemann, Oxford, 1999.

[20] K.A. Unocic, M.J. Mills, G.S. Daehn, Effect of gallium focused ion beam milling on preparation of aluminum thin foils, Journal of Microscopy, 240 (2010) 227-238.

[21] S. Morito, K. Oh-Ishi, K, Hono, T. Ohba, Carbon enrichment in retained austenite films in low carbon lath martensite steel, ISIJ International, 51 (2011) 1200-1202.

[22] S.M.C. van Boheman, J. Sietsma, Effect of composition on kinetics of athermal martensite formation in plain carbon steels, Materials Science and Technology, 25 (2009), 1009-1012.

[23] F. Maresca, V.G. Kouznetsova, M.G.D. Geers, On the role of interlath retained austenite in the deformation of lath martensite, Modelling and Simulation in Materials Science and Engineering, 22 (2014) 045011.

Chapter 8. Lath martensite plasticity enabled by sliding of sub-structure boundaries[1]

Abstract

Lath martensite is widely present in advanced high strength steels as a key strengthening phase. The unexpected ductility of lath martensite has been reported in literature in both single phase and multiphase steels, however, without systematic identification of the plasticity mechanisms. In this study, well-defined micro-tensile tests are carried out on fully martensitic steel with a clean large substructure and a variety of substructure boundaries orientations with respect to the loading direction. Two lath martensite deformation mechanisms were identified, namely, crystallographic slip and substructure boundaries sliding, that compete with each other to carry the overall plasticity. The conditions under which these two mechanisms are active depend on the difference between the highest Schmid factor of the slip systems which lie in the boundary planes and that of the slip systems which do not lie in the boundary planes. In addition, micro-tensile tests are applied on dual phase specimens after a detailed analysis of the lath martensite boundaries. It was found that the sliding mechanism is also of great importance for lath martensite deformation in multiphase steels, which leads to an unexpected high local strain. Finally, the potential contribution of the sliding mechanism to plasticity in bulk materials is discussed.

8.1 Introduction

Among all types of ferrous martensite, lath martensite can be found in a large variety of commercial steels such as dual phase (DP) steel, transformation induced plasticity (TRIP) steel, maraging steel and quenching and partitioning steel, where it serves as a strengthening phase. Its strengthening mechanisms include dislocation hardening [1,2], solid solution hardening [2], precipitation strengthening [2,3] and the substructure boundary strengthening [4-10] which has the most important contribution to lath martensite's strength. On the other hand, similar to most strong materials, lath martensite is generally known to be brittle [2,11-15]. The origin of the brittleness of lath martensite has been attributed to elements segregation, e.g. in [11], and tempering embrittlement [2,12-15].

On the contrary, apparent ductility of lath martensite has also been reported in the literature. Ghadbeigi *et al.* showed evidence of remarkably high strains in martensite within DP steel up to 120% [16]. Similar observations are reported by [17,18] with local martensite strain exceeding 70%. Moreover, the fracture surfaces of DP steel show dimples [18-21], which are attributed as signature of ductile fracture [19,22,23]. In single-phase steels which contain only lath martensite, the overall fracture strain can still be as large as 20% in sandwiched specimens [24,

---

25]. Therefore, in both single phase and multi-phase steels, lath martensite may reveal (much) higher ductility than what is usually expected for a brittle material.

In order to investigate the ductility of lath martensite, we recently performed uniaxial tensile tests on micro-specimens of lath martensite specimens out of a single packet/block [10, 26]. Specimens with a specific orientation of the martensite substructure boundaries were selected, yielding the maximum resolved shear stress on the boundary planes, i.e. boundaries perpendicular to the specimen front surface and with an angle of ~45° with respect to the loading direction. These micro-tensile tests revealed a novel sliding mechanism of lath martensite, as shown in Fig. 8.1 taken from Ref. [26]. Sliding of laths clearly occurs at certain lath boundaries, as indicated by the white arrows at the steps. From this and other tests, it was concluded that this sliding mechanism can be active at all types of tested boundaries, lath, sub-block, and block boundaries, and that boundary sliding is in competition with crystallographic slip. However, these micro-tests on martensite boundaries were only tested at their most favorable orientation for sliding, hence, whether or not boundary sliding is important in other orientations and in bulk multi-phase steels remained an open question.
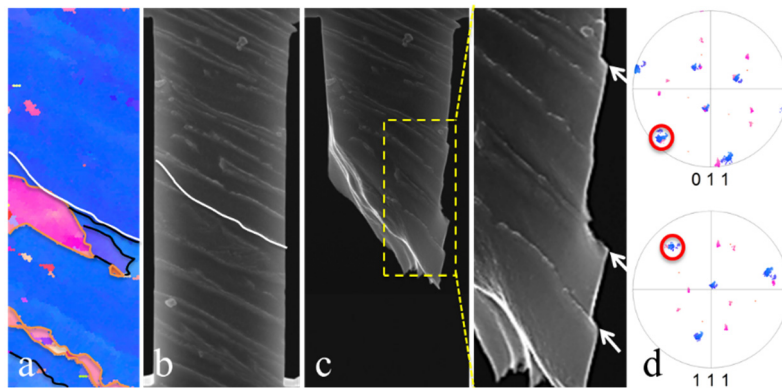
Figure 8.1 The gauge part of a lath martensite micro-tensile specimen. (a) Inverse pole figure map (IPF) on which the substructure boundaries are marked with colors: Orange represents block boundaries, black means sub-block boundaries and the white lines mark the subsequent fracture surface. (b,c) SEM SE images of the gauge section before and after fracture, together with a zoom-in of the area in the yellow dashed frame. The white arrows indicate the positions where boundary sliding occurred. (d) {011} and {111} pole figures of the specimen, in which the slip system with the highest Schmid factor is marked by red circles. The initial length of the specimen is 9 μm.

The goal of this work is to study the conditions under which the sliding mechanism is activated and to investigate the relevance of this mechanism in engineering (multi-phase) steels containing lath martensite. In particular, the following questions will be addressed. (1) Does boundary sliding also occur for random boundary orientations? (2) Under which conditions is this mechanism active? (3) In a multiphase steel, is boundary sliding promoted or demoted by the morphology and orientation of the substructure boundaries in lath martensite islands? And (4), how important is this sliding mechanism as a plastic mechanism in lath-martensite-based

(multiphase) steels?

In an effort to provide conclusive answers to these questions, the research focuses on two engineering steels with the same overall chemical composition, a fully martensitic (FM) steel and a DP steel, which are at the extremes of the spectrum with respect to (i) strength vs. ductility, (ii) martensite volume fraction, and (iii) loading constraints acting on the martensite domains of lath-martensite-containing steels. The FM steel has sharper substructures enabling clear microstructural, crystallographic and micro-mechanical analysis. The DP steel is a well-known example of lath-martensite-based multiphase steels, for which rich data is available in literature on all aspects.

The investigation starts with a more extensive study of the sliding mechanism using micro-tensile tests of specimens with unfavorably oriented boundaries, e.g. boundaries that are not perpendicular to the front surface and/or not at ~45° to the loading direction. Subsequently, the activation threshold for the sliding mechanism is analyzed. Next, the morphology of substructure boundaries of lath martensite in the multiphase steel is analyzed to assess the activation potential of the sliding mechanism. And, finally, micro-tensile tests of DP steel specimens with embedded lath martensite islands inside are conducted to determine the activity of the sliding mechanism in a multiphase steel, after which the relevance of this mechanism for such bulk metals is discussed.

8.2 Material and methodology

Two materials are used in this study, a DP steel (0.092C-1.68Mn-0.24Si-0.57Cr) with 25% lath martensite volume fraction and a fully lath-martensitic (FM) steel obtained by 2-hour heating of the DP steel at 1000 °C, followed by water quenching. The heat treatment transforms the DP steel into a FM steel with clean and large substructures which makes it straightforward to analyze its deformation behavior. Figure 8.2(a,b) shows the microstructure of two materials.

Adopting the micro-tensile test methodology described in Ref. [27], multiple-parallel micro-tensile specimens of the two materials are tested. The specimens are fabricated using focused ion beam (FIB) milling at the tip of a wedge that is prepared from the bulk material. Milling parameters and procedures are carefully chosen to minimize the influence of Ga+ ions on the specimens. The gauge part of the specimens is 9 μm in length with a cross section of ~3×2 μm². Figure 8.2 (c,d) show examples of micro-tensile specimens of FM and DP steel respectively. Each specimen is characterized using scanning electron microscopy (SEM) and electron backscattered diffraction (EBSD) from both the front and backside of the specimen (note, that only the front side images are shown in this paper). The tensile tests are conducted with a nano-force tensile stage with accurate specimen alignment (<0.1 mrad angular alignment and near-perfect co-linearity) and precise force (force range of 0.07 μN to 250 mN) and displacement (<6 nm reproducibility) resolution [28].
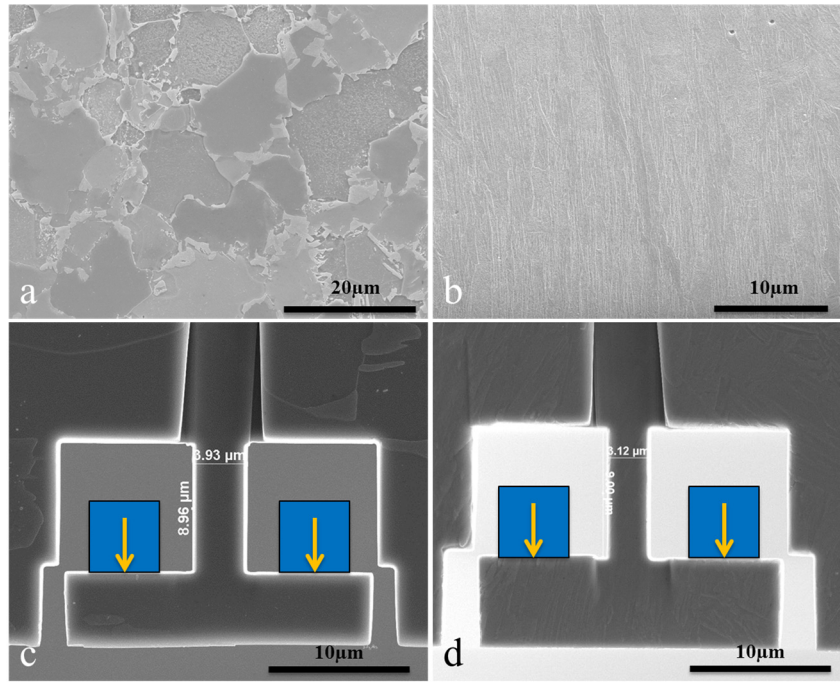
Figure 8.2 (a) SEM SE image of the microstructure of DP steel tested in this study. (b) SEM SE image of the microstructure of FM steel. A region with parallel laths is selected, which is large enough for the fabrication of a micro-tensile specimen. (c,d) Examples of micro-tensile specimens extracted from DP steel and FM steel respectively. The two blue blocks represent the pins of the loading gripper which pulls the specimen cross-bar downwards (in the images). The vertical bar is the specimen gauge section.

8.3 Results and discussion

In total 15 FM steel micro-specimens with clean sub-structures were tested and grouped by the type of deformation exposed. The specimens that showed fracture surfaces parallel to the boundary traces are presented in Fig. 8.3, whereas the specimens that fracture along other directions are shown in Fig. 8.4. For each specimen, from left to right, the following data are shown: (i) a backscattered electron (BSE) SEM image of the untested specimen, which shows the substructure surface traces due to the channeling contrast; (ii) and (iii) a secondary electron (SE) and BSE image of the fractured specimens respectively; (iv) an inverse pole figure (IPF) map from EBSD of the untested specimen, with substructure boundaries marked in different colors as used in Fig. 8.1 and the fracture surface marked in white; (iv) the {110} and {111} pole figures of the specimen gauge section.

The substructure boundaries are parallel to the habit plane of phase transformation, i.e. one of the {111} planes of the parent austenite is parallel to one of the {110} planes of martensite [29]. Therefore, the {110} martensite pole figures can be used to determine the substructure boundary orientations. Since only the {110}<111> slip system is active in lath martensite [10], the {112}<111> or {123}<111> slip systems will not be considered further. Out of the twelve {110}<111> slip systems, two slip systems are parallel to the boundary planes, which will be

referred to as the in-plane slip systems [25]. The in-plane system with the higher Schmid factor is marked in red in the {110} and {111} pole figures. In addition, there are ten slip systems which are distributed over the five {110} planes that are not parallel to the substructure boundaries, which will be referred to as the out-of-plane slip systems [25]. The out-of-plane system with the highest Schmid factor is marked with green circles in the {110} and {111} pole figures. The values of the highest Schmid factors of the in-plane and out-of-plane slip systems are given in Table 8.1.

Most the specimens in Fig. 8.3 (all but specimens S3a, S3c and S3d) have their boundary planes of the samples not perpendicular to the specimen front surface (β different from 90°), as evidenced by projection point marked by the red circles in the {110} pole figure, which does not touch the periphery of the projection circle. In addition, the angle of the boundary surface traces, α, deviate from 45°. These are the main differences between the samples tested in this study compared to the ideal specimens tested in [26], which all have their boundaries perpendicular to the specimen surface and at ~45° to the load axis, as shown e.g. by the red marker on the pole figure periphery in Fig. 8.1.

From Table 8.1 it can be seen that specimen S3a, S3b, and S3c all contain an out-of-plane slip system with a higher Schmid factor than the two in-plane slip systems. Therefore, in case of crystallographic slip, this out-of-plane slip system should activate first. However, for none of these three specimens, out-of-plane slip activity could be observed. In addition, no in-plane slip traces, which would be parallel to the boundary surface traces, are visible nor are there other indications of in-plane slip, e.g., on the side of the specimens. In contrast, the fractures of these specimens are along one of the substructure boundaries, as indicated with the white line in the IPF map. Therefore, there must be a preferential deformation mechanism which occurs at the boundaries of lath martensite substructures. This is the sliding mechanism as was already identified in the previous study (Fig. 8.1). Considering that, for S3a-S3c, the maximum out-of-plane SF is higher than the SF for boundary sliding, this sliding mechanism must be easier to activate than crystallographic slip. Specimens S3a-S3c have a non-optimal surface orientation in the sense that the following requirements are not fulfilled simultaneously: (i) α close to 45° with respect to the loading directions and (ii). β close to 90°. This shows that even under arbitrary boundary orientations where the resolved shear stress on the boundaries is lower than on some of the crystallographic slip systems, the deformation is predominantly mitigated by boundary sliding.

For specimen S3d-S3f the out-of-plane slip systems have Schmid factors that are approximately equal to that of the in-plane slip systems. Given the presence of a huge amount of dislocations in lath martensite and probably also a high density of dislocation sources, it is logical to assume that both in-plane and out-of-plane systems should equally be activated to accommodate the plastic deformation, resulting in slip traces from both these two systems on the specimen surface. However, no slip traces are visible on the deformed specimen surface, the fracture plane of the specimens nicely coincides the sub-structure boundaries, and the deformation localizes at the boundaries. This confirms that the sliding mechanism is the dominant plastic mechanism.
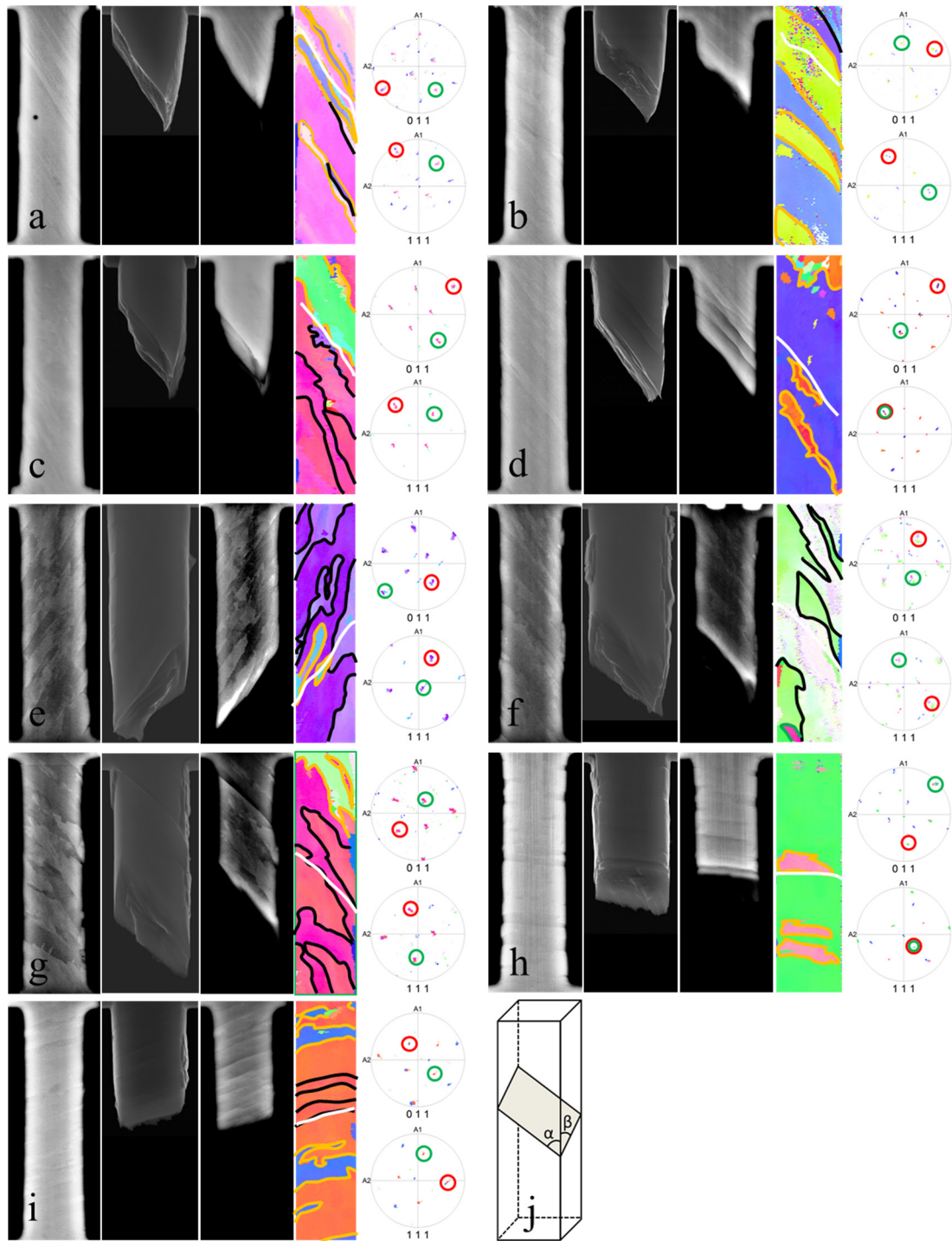
Figure 8.3 Nine 9 µm-long specimens (Specimen 3a-3i) with boundaries tilted with respect to the loading direction. For each specimen from left to right: BSE image of the original specimen gauge section; SE and BSE images of the fractured gauge section respectively; IPF of the gauge section, with the substructure boundaries marked in different colors: block boundaries in orange, sub-block boundaries in black, lath boundaries left unmarked, and fracture surfaces marked in white; {110} and {111} pole figures of the gauge section. The red and green circles indicate, respectively, the in-plane and out-of-plane slip system with the highest Schmid factor. (j) is an illustration of the angle definitions in Table 8.1. The light gray plane represents a substructure boundary of a lath martensite specimen.

For specimen S3g-S3i, the in-plane slip systems have a higher Schmid factor than the out of plane slip systems, therefore, the in-plane slip is favored over the out-of-plane slip. Even though these specimens are more favorably oriented for boundary sliding than specimen S3a-S3e, in-plane crystallographic slip traces parallel to the boundaries are visible in the deformed BSE image of S3i. In spite of these, all specimens fracture along the substructure boundaries. Note that the boundaries in specimen S3i are more straight than most of the other specimens in Fig. 8.3. Particularly, the sliding boundary triggering fracture in specimen S3i shows a curvature in the middle, which explains why the fracture stress is here much higher than that of the other micro-tests in Table 8.1. This may explain why the non-straight nature of the boundary may be the reason why in-plane crystallographic slip is triggered in these cases. Hence, crystallographic slip still contributes to the overall deformation of the specimen. Boundary sliding and crystallographic slip cooperate and compete with each other to carry the overall specimen plasticity. Nevertheless, all specimens fracture along one of the boundaries. Therefore, in the competition between crystallographic slip and the sliding mechanism, the latter is most important for the ultimate behavior.

Table 8.1 Characteristics of the micro-specimen (S1) in Fig. 8.1 and nine specimens (S3a-S3i) of Fig. 8.3, from top to bottom: the fracture stress; the highest Schmid factors of the out-of-plane and in-plane slip systems; the Schmid factor of the boundary planes for sliding (corresponding to the boundary slip direction that yields the highest SF, i.e. greater than or equal to the maximum in-plane SF); the angle between the boundary trace on front surface of the specimen and the load axis (α); and the angle between the boundary trace on side surface of the specimen and the load axis (β) (for the definition of α and β, see plotting in Fig. 8.3(j)). For reference, the characteristics of specimen 1 of Fig. 8.1 are also given.

Specimen No.	1	3a	3b	3c	3d	3e	3f	3g	3h	3i
Fracture stress (MPa)	760	858	871	875	791	859	799	779	842	944
Max. out-of-plane SF (-)	0.45	0.50	0.48	0.48	0.43	0.48	0.44	0.42	0.34	0.42
Max. in-plane SF (-)	0.50	0.46	0.45	0.46	0.43	0.49	0.45	0.45	0.41	0.46
SF boundary sliding (-)	0.50	0.46	0.46	0.49	0.49	0.49	0.49	0.47	0.48	0.48
α (°)	46	34	46	39	41	-54	62	42	-83	-61
β (°)	81	81	51	87	85	53	61	59	54	43

The question remains why the out-of-plane slip systems in specimen S3a-S3c were not activated during the deformation, even though their maximum Schmid factor is higher than the maximum Schmid factor of the in-plane slip systems. This is due to the fact that the out-of-plane slip needs to cross the sub-structure boundaries because their different slip directions do not lie in the boundary planes, which requires a higher resolved shear stress than dislocation movement only inside the martensite lath. It has been demonstrated that both block [3-9] and sub-block boundaries [10] act as barriers to dislocation motion. In addition, as stated already, the critical stress to activate the sliding mechanism is lower than that of crystallographic slip. Therefore, the sliding mechanism is in general the preferred one.
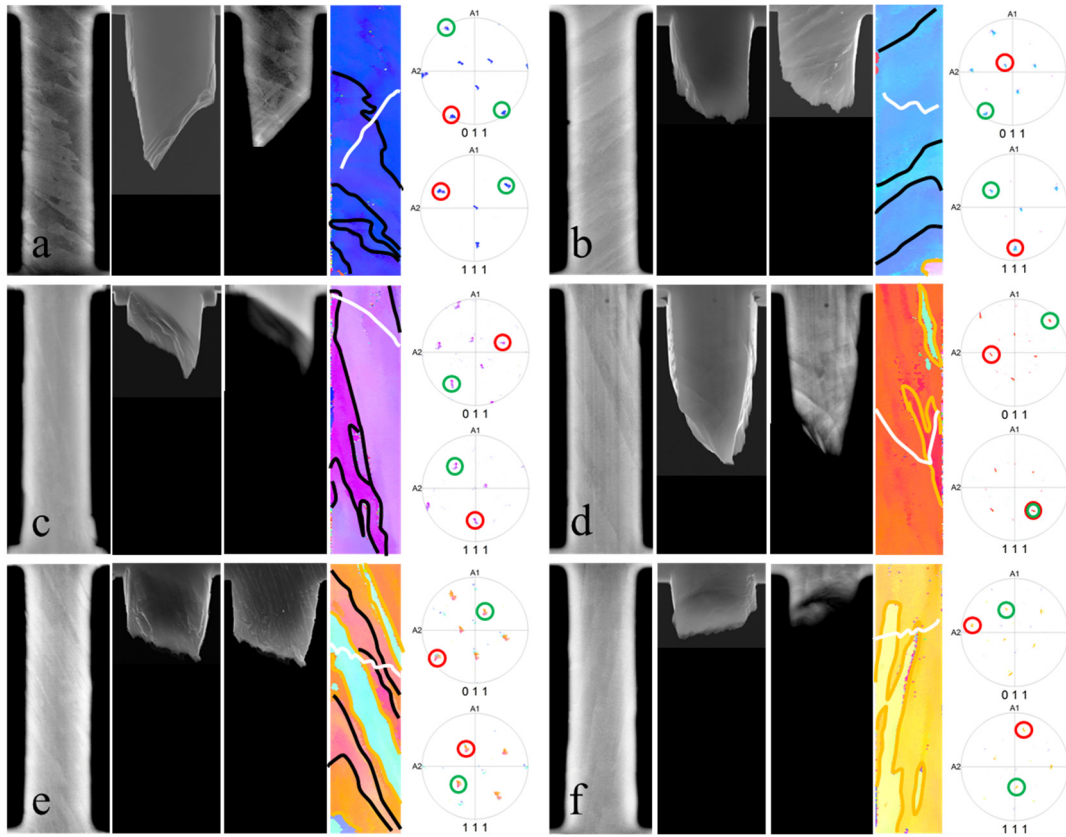
Figure 8.4 Six 9 µm-long specimens (Specimen 4a-4f) with tilted boundaries to the loading direction. For each specimen from left to right: BSE image of the original specimen gauge section; SE and BSE images of the fractured gauge section respectively; IPF of the gauge section, with substructure boundaries marked in different colors: block boundaries in orange, sub-block boundaries in black, lath boundaries left unmarked, and fracture surfaces marked in white; {110} and {111} pole figures of the gauge section. The red and green circles indicate, respectively, the in-plane and out-of-plane slip system with the highest Schmid factor.

Sliding at substructure boundaries is an important deformation mechanism of lath martensite even when the boundary is not favorably oriented. It competes and cooperates with crystallographic slip and often dominates. However, there are also cases where boundary sliding is not activated. Figure 8.4 shows six specimens with substructure boundaries tilted to the loading direction with different angles. Boundary types are again indicated by the marked colors. Specimens S4a-S4c are single block specimens while the others are multi-block specimens. The in-plane slip system and the out-of-plane system with the highest Schmid factors are again indicated with red and green circles respectively. The Schmid factors of the samples are given in Table 8.2.

Contrary to the specimens in Fig. 8.3, the specimens in Fig. 8.4 are all fractured by the out-of-plane slip systems (green systems in the pole figure), which cut through the substructure boundaries, as indicated by the white lines in the IPF maps. All six specimens have a considerably higher maximum Schmid factor of the out-of-plane slip systems compared to the in-plane systems (Table 8.2). Among the three single block specimens, it is not surprising that

the sliding mechanism is not activated in S4b and S4c since the resolved shear stress in the boundary planes is significantly lower than that of out-of-plane crystallographic slip. Moreover, the fracture surface is straight for specimens S4a and S4c, indicating that the dislocations are able to pass through the sub-block boundaries. This observation agrees with Ref. [26]. The multi-block specimens S4d-S4f all show zig-zag fracture surfaces. Further analysis reveals that the turning points of the fracture surfaces correspond to the positions of the block boundaries, which is in agreement with observations that the dislocations cannot move through block boundaries [7,10]. The zig-zag shape of the fracture surface results from the staggering small sections of fracture surface of individual blocks that have different trace angles with respect to the loading direction, in line with the observations in [10]. Due to the low Schmid factors for boundary sliding (and for the in-plane slip systems), the out-of-plane slip systems are first activated, even though the dislocations need to pass through the block boundaries, which are stronger barriers to dislocation motion than the sub-block boundaries [10]. In general, for both single-block and multi-block cases shown in Fig. 8.4, sliding is not possible due to the low resolved stress on the boundary planes, forcing crystallographic slip to carry the plastic deformation.

Table 8.2. Characteristics of six specimens (S4a-S4f) of Fig. 8.4, from top to bottom: the fracture stress; the highest Schmid factors of the out-of-plane and in-plane slip systems; the Schmid factor of the boundary planes for sliding (corresponding to the boundary slip direction that yields the highest SF, thus, it is greater than or equal to the maximum in-plane SF); the angle between the boundary trace on front surface of the specimen and the load axis (α); and the angle between the boundary trace on side surface of the specimen and the load axis (β).

Specimen No.	4a	4b	4c	4d	4e	4f
Fracture stress (MPa)	873	874	857	954	1013	1053
Max. out-of-plane SF (-)	0.45	0.4	0.47	0.45	0.45	0.46
Max. in-plane SF (-)	0.38	0.23	0.22	0.05	0.34	0.12
SF boundary sliding (-)	0.4	0.23	0.24	0.08	0.47	0.13
α (°)	64	-42	17	6	35	-7
β (°)	87	21	58	47	80	77

Note that specimens S3a, S3c, S3d and S4a have their block boundaries perpendicular to the front surface. The former three specimens activated sliding while the latter does not. The difference originates from the relative maximum Schmid factor values of the in-plane systems compared to the out-of-plane ones. Neither the angle between the boundary plane and the specimen front surface (β) alone nor the trace angle (α) alone determines the dominant deformation mechanisms, namely crystallographic slip or sliding at the boundaries. Instead, the difference of the highest Schmid factors of the in-plane slip systems and the out-of-plane systems is the main factor which determines the main deformation mechanism. In addition, the boundary type is also important because it determines the threshhold stress at which dislocations can across a certain boundary. A lath boundary is the weakest in terms of blocking dislocation movement, whereas the sub-block boundaries are stronger and block boundaries

even stronger. This clarifies the difference of the strength of the specimens in Fig. 8.4. For boundaries strongly impeding crystallographic slip, the sliding mechanism might be still more favorable even with less favorable orientations.

The fracture stress varies for specimens with the same active mechanisms (e.g. sliding mechanism in Fig. 8.3). In addition to the differences in curvature of the boundaries, other differences may contribute as well as analyzed next. Reconsidering Fig. 8.1 and Fig. 8.3 in terms of boundary types, the sliding mechanism is observed to be activated at all kinds of sub-structure boundaries, e.g. block boundary in S3a-S3f, lath boundary in specimen S1 shown in Fig. 8.1 and sub-block boundaries observed in S3g, S3i from Fig. 8.3. However, a preference in terms of a boundary type that is more easily activated cannot be identified. In addition, due to the near parallelism between boundaries from the same specimens, the resolved shear stress on all the boundaries are almost equal. Consequently, the boundaries should have equal probability to activate sliding. Yet, in general, only one of the parallel boundaries exhibits sliding. Hence, there exists an intrinsic variability in these boundaries, related to the intrinsic structure of the boundaries at smaller scales.

The austenite-to-martensite phase transformation is never complete and there always remains retained austenite [30,31]. Indeed, the presence of retained austenite has been found by TEM studies of lath martensite, in the form of blocks but also as ultra-thin (~10 nm thick) inter-lath retained austenite films between the laths [32-35]. Using crystal plasticity simulations, it was shown that the presence of such ultra-thin austenite films might explain sliding of the boundaries because the activation of austenite (FCC) slip systems is much easier than those of martensite (BCC) and since three austenite slip systems are always aligned with the habit plane (and thus with the boundaries) [36]. This is one of the possible explanations for why boundary sliding is easier activated than BCC crystallographic slip in the laths. It does, however, not explain the observed large variability in the activation of certain type of boundaries and in boundaries of the same type for sliding. TEM analysis was therefore conducted together with transmission Kikuchi diffraction for boundary type identification. Multiple attempts were conducted to reveal presence of the inter-lath retained austenite films. However, for the two steels investigated here, it was not straightforward to identify these austenite films, consistent with the comments reported in [37]. The interaction-volume contribution from such a thin austenite film is too small compared to the lath martensite and a special orientation is required to reveal their presence. Even though the inter-lath retained austenite films could not be confirmed directly, interesting observations of the boundaries were made that might explain the variability in boundary sliding activation. Figure 8.5 shows an IPF map from transmission Kikuchi diffraction measurement on top of a TEM dark field image and a bright field image. The block boundaries are marked using the same color code as in Fig. 8.3 and Fig. 8.4, the sub-block boundaries are in green here for visibility. The unmarked boundaries are lath boundaries. It can be seen that various boundaries of different substructure levels are present in the region covered by the TEM dark field images. The white precipitates are carbides, which were found at all types of boundaries. The carbides are present only at some of the boundaries and their presence does not depend on the type of boundary. Moreover, their density changes a lot even

along the same boundary, and as a consequence the carbon solid solution concentration must also be rather heterogeneous. Whatever the precise atomic mechanism for boundary sliding, whether it is crystallographic slip in the inter-lath retained austenite or not, the presence of the carbide precipitates in the boundaries will certainly obstruct the boundary sliding mechanism. Therefore, the variability of the carbide density between boundaries and along the boundary length appears to be one of the small scale features inducing the large variability in boundary sliding activation and the accompanying differences in stress levels.
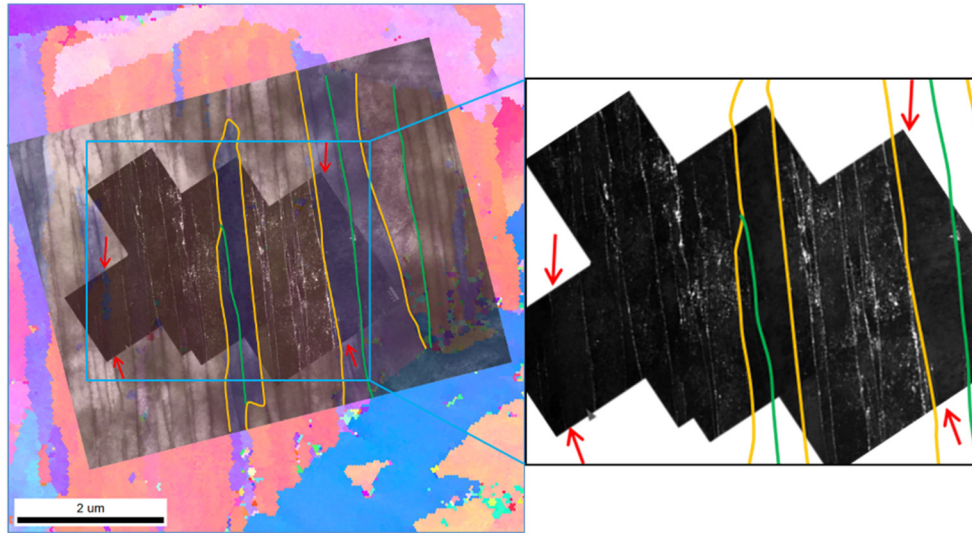
Figure 8.5 An IPF map from transmission kikuchi diffraction measurement on top of a TEM dark field image and a bright field image with a zoom-in of the blue frame. The white particles are carbides in the dark field image. The red arrows indicate the positions of boundaries which do not contain carbides.

It has been demonstrated that sliding at lath martensite boundaries is an important deformation mechanism in FM steels. As stated in the introduction, lath martensite also exists as the strengthening component of multiphase steels. The next aim is therefore to investigate if this sliding mechanism is still activated in these multiphase steels. Let us first characterize the substructure boundaries in the lath martensite islands of the DP material, which is used as an example of lath-martensite-containing multiphase steel. Figure 8.6 shows one EBSD measurements of martensite in DP steel. The IPF maps are plotted together with the image quality (IQ) maps, in which the martensite domains appear darker due to the higher dislocation density. Many boundaries cross over the full width of the martensite band. Most of these boundaries are tilted to the length direction of martensite and almost no boundaries are aligned with the length direction. This is likely due to the orientation-dependent stress built-up in the austenite-to-martensite transformation. In particular, the necking regions of martensite domains have boundaries approximately perpendicular to the length directions. The boundaries which might slide during the deformation are indicated by green arrows in Fig. 8.6(b) when the specimen is pulled horizontally. These are identified from the Schmid factors of slip systems in the laths and the boundaries (under assumption that the boundaries are planar in 3D and are approximately parallel to the {110} planes of the adjacent martensite laths).

Therefore, in lath martensite bands in DP steel many substructure boundaries exist for which boundary sliding is expected to occur based on this morphological analysis. In addition, their substructure boundaries are located preferentially in the thin section of the martensite bands. This is consistent with the results on localized plasticity in martensite banding observed in [38]. Additional analysis was done on individual islands of DP steel, i.e. outside the martensite bands. Even though less clear, the same conclusions apply, i.e. martensite sliding is also expected in the thin section of separate martensite islands.
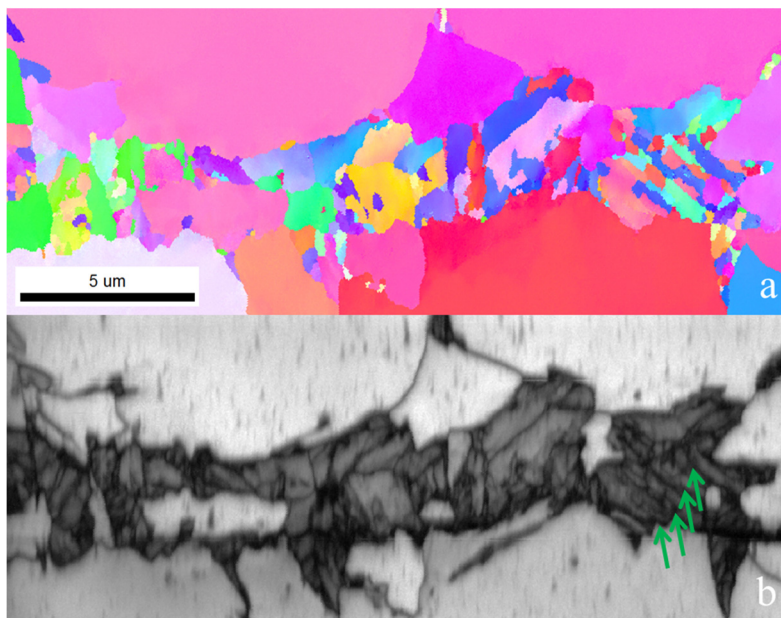

Figure 8.6 EBSD scan of lath martensite in DP steel. (a) IPF of the measurement and (b) the corresponding image quality map in which the green arrows indicate the boundaries at which the sliding mechanism is most probable.

Although the constraints on lath martensite in the DP steel micro-specimen are quite different in comparison to the constraints inside a bulk material, micro-tensile tests on DP steel are carried out to characterize the activation of boundary sliding. These tests allow to focus on the evolution of a particular micro-region under a simple loading state. In total, eight specimens were tested, and seven specimens out of them showed simple fracture behavior along paths in ferrite grains. One example is given in Figure 8.7 where a micro-tensile specimen of DP steel before and after fracture is shown. Due to the phase contrast between ferrite and martensite, the specimen is fractured along an easy path which does not have martensite in it, although the fracture surface needs to cross a ferrite grain boundary. The loading constraints of the martensite islands in a micro-specimen are much lower than in a bulk material. In the bulk, the ferrite grains will start to deform first, at certain point their deformation will be inhibited until either the martensite islands start deforming to accommodate the overall deformation or until the boundary between ferrite and martensite delaminates. In these micro-specimens, however, a deformation percolation path in the ferrite can be easily formed over the entire specimen cross-section, along which all deformation will continue to concentrate until fracture. This explains why in these seven micro-tests the martensite islands did not deform, i.e. revealed

neither boundary sliding nor crystallographic slip. In contrast, in a bulk multi-phase steel, martensite plasticity is known to be an important mechanism to obtain a good contrast between strength and ductility [39]. Therefore, as these seven particular micro-tests do not show any martensite plastic deformation, no conclusion can be drawn yet on the role of boundary sliding.
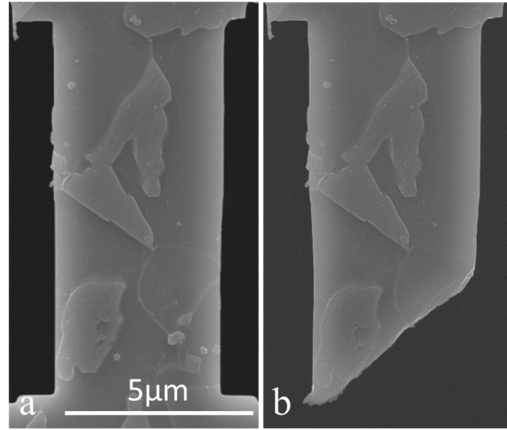
Figure 8.7 SEM SE images of the gauge part of a DP micro-tensile specimen before and after fracture, in which the fracture occurred along a straight path through the ferrite grains.

It is therefore more interesting to investigate in detail whether the micro-test that did show martensite plasticity deformed by boundary sliding or not. In Fig. 8.8, the final micro-tensile specimen of DP steel is shown. A few martensite islands are scattered in the upper part of the gauge section and a long martensite island is aligned roughly parallel to the loading direction while at the bottom another martensite island is present. Although the gap between martensite islands is smaller than that of Fig. 8.6, there is still an 'easy' path for ferrite deformation, as indicated by the white arrow in the undeformed specimen. However, the actual fracture of the specimen occurred at the bottom part of the specimen, which propagates around the bottom martensite domain. Detailed observation reveals that the top part of the island is completely sheared off into two straight parts, indicated by the green arrows in the deformed specimen in the zoom of Fig. 8.8(d). This indicates that the fracture and the shearing of the martensite domain at the bottom of the gauge section is easier than the ferrite path, suggesting an (easy) sliding mechanism across the full martensite island cross section. This is confirmed by the sharp nature of the two sheared parts. Based on the results in Fig. 8.3, a straight shearing surface is a characteristic for boundary sliding. In contrast, when in-plane crystallographic slip is activated in lath martensite, it activates over many crystal planes simultaneously, as shown in specimen S3i, because of the high initial dislocation density. Therefore, the sharp straight shear path suggests the presence of substructure boundary in the martensite domain.

In general, the sliding mechanism is not easily often observed in micro-tensile test of DP specimens, but it did occur, whereas no clear evidence for crystallographic slip was found in any of the martensite islands in all micro-tests (although deformation of the tiny martensite ligaments between martensite islands was observed in a few instances). Taking into account

that martensite plasticity is known to occur frequently in bulk material [16,39], boundary sliding may be the main martensite deformation mechanism in bulk lath-martensite containing multi-phase steels. This mechanism, when it occurs, can introduce large strain locally within the martensite domains. For example, Ghadbeigi *et al.* showed that the local strain of martensite can reach up to 120% [16]. More evidence of martensite ductility can be found in DP steels [17-21] In addition to DP steels, lath martensite in other multiphase steels have shown indications of sliding mechanism as well, as indicated in [40,41] in TRIP steel. Therefore, the sliding mechanism may be an important mechanism explaining ductility of lath martensite at local regions.
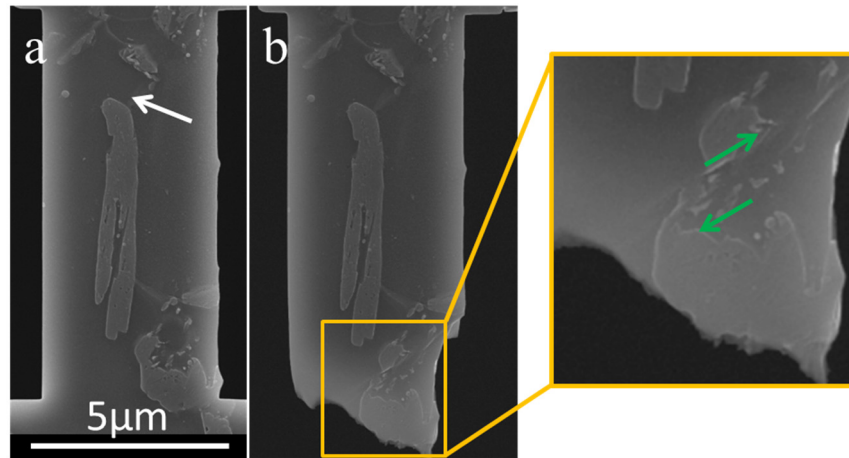

Figure 8.8 SEM SE images of the gauge part of a DP micro-tensile specimen before and after fracture. The fracture did not occur through the ferrite indicated with the white arrow, but in the lower martensite island. A zoom-in of the orange frame is given on the right where the original bottom martensite island is sheared off into two straight parts as indicated by the green arrows.

Moreover, indications of sliding mechanism have been observed in fully martensitic bulk material [24,25]. It is reported that 'at strain levels less than the transition strain, slip bands were found to develop parallel to the lath plane only within martensite blocks that have a large Schmid factor for the slip systems where the Burgers vector is parallel to the lath growth direction.'[24] The slip bands could well be traces of the sliding mechanism since these the traces are perfectly aligned with the boundaries. Moreover, the observation scale in the SEM images in [24] is too large to provide a direct link between the distances between the slip traces and the width of martensite laths. It is easier to visualize the exact positions of the steps/traces from a side view, which is the approach in this study and in [26]. It is worth to note that Nambu et al. pointed out that the slip traces only occur in 'martensite blocks that have a large Schmid factor for the slip systems'. This corresponds with the criteria investigated here under which the sliding mechanism is more favorable than crystallographic slip. If these criteria are not fulfilled, crystallographic slip has to occur, but at higher stress levels. This is consistent with the observations in [24,25], which showed that the crossing of the substructure boundaries is not favored until a high strain level is reached by deformation of lath martensite sandwiched by Nickel layers. Therefore, in bulk fully martensitic steel, the sliding mechanism is important for

the deformation at the early stages, in which the stress level is not high and statistically there are always boundaries aligned in a favorable orientation for this mechanism. When the stress and strain levels get higher, the crossing of substructure by crystallographic slip can be activated.

Hence, the sliding mechanism is not only important for micro-tensile specimens but also in bulk materials which contain lath martensite, either fully martensitic steels or multiphase steels.

8.4 Conclusions

Micro-tensile specimens of lath martensite are tested using a nano-force tensile stage. The substructure boundaries of these specimens are tilted randomly with respect to the loading direction. According to the analysis of the different specimens investigated, following conclusions are drawn:

(1) The sliding mechanism occurs when the substructure boundaries are tilted with respect to the loading direction and it is not necessary that the boundaries are perpendicular to the specimen front surface and have a tilting angle of 45° with respect to the loading direction, as tested previously. Namely, sub-optimally oriented boundaries are also candidates for the sliding mechanism.

(2) The difference between the maximum Schmid factors of the in-plane slip systems and the out-of-plane slip systems determines the dominant deformation mechanism, namely the sliding mechanism or crystallographic slip.

(3) When the resolved stress on the boundary planes is too low, crystallographic slip has to be activated even when it has to cut though the boundaries.

(4) Contrary to fully martensitic steels, the sliding mechanism was infrequently observed in the lath martensite of the multiphase steels at the micro-scale. However, it still occurs, proving the existence of this mechanism in multiphase steels, which is supported by other studies on bulk materials in the literature.

(5) The sliding mechanism is important in the bulk fully martensitic steels, even at low strains and low stress levels. As stress and strain increase, cutting of crystallographic slip through the substructure boundaries becomes a competing deformation mechanism.

References

[1] S. Takaki, K. Ngo-Huynh, N. Nakada, T. Tsuchiyama, Strengthening mechanism in ultra low carbon martensitic steel, ISIJ International, 52 (2012) 710-716.

[2] G. Krauss, Martensite in steel: strength and structure, Materials Science and Engineering A, 273-275 (1999) 40-57.

[3] T. Ohmura, T. Hara, K, Tsuzaki, Evaluation of grain boundary effect on strength of Fe--C low alloy martensitic steels by nanoindentation technique, Scripta Materialia, 49 (2003) 1157-1162.

[4] S. Morito, H. Yoshida, T. Maki, X. Huang, Effect of block size on the strength of lath martensite in low carbon steels, Materials Science and Engineering A, 438-440 (2006) 237-240.

[5] C. Zhang, Q. Wang, J. Ren, R. Li, M. Wang, F. Zhang, K. Sun, Effect of martensitic morphology on mechanical properties of an as-quenched and tempered 25CrMo48V steel, Materials Science and Engineering A, 534 (2012) 339-346.

[6] T. Ohmura, T. Hara, K, Tsuzaki, Evaluation of temper softening behavior of Fe–C binary martensitic steels by nanoindentation, Scripta Materialia, 49 (2003) 1157-1162.

[7] A. Shibata, T. Nagoshi, M. Sone, S. Morito, Y. Higo, Micromechanical characterization of deformation behavior in ferrous lath martensite, Journal of Alloys and Compounds, 577 (2013) 555-558.

[8] H. Ghassemi-Armaki, R. Maaß, S.P. Bhat, S. Sriram, J.R. Greer, K.S. Kumar, Deformation response of ferrite and martensite in a dual-phase steel, Acta Materialia, 62 (2014) 197-211.

[9] Y. Mine, K. Hirashita H. Takashima, M. Matsuda, K. Takashima, Micro-tension behaviour of lath martensite structures of carbon steel, Materials Science and Engineering A, 560 (2013) 535-544.

[10] C. Du, J.P.M. Hoefnagels, R. Vaes, M.G.D. Geers, Block and sub-block boundary strengthening in lath martensite, Scripta Materialia, 116 (2016) 117-121.

[11] P. Bowen, C.A. Hippsley, J.F. Knott, Effects of segregation on brittle fracture and fatigue crack growth in coarse-grained, martensitic A533B pressure vessel steel, Acta Metallurgica, 32 (1984) 637-647.

[12] J.W. Morris, On the Ductile-Brittle Transition in Lath Martensitic Steel, ISIJ International, 51 (2011) 1569-1575.

[13] T. Inoue, S. Matsuda, Y. Okamura, K. Aoki, The fracture of a low carbon tempered martensite, Transactions of the Japan Institute of Metals 11(1970) 36-43.

[14] R.M. Horn, R.O. Ritchie, Mechanisms of tempered martensite embrittlement in low alloy steels, Metallurgical Transactions A, 9 (1978) 1039-1053.

[15] J.P. Materkowski, G. Krauss, Tempered Martensite Embrittlement in SAE 4340 Steel, Metallurgical Transactions A, 10 (1979) 1643-1651.

[16] H. Ghadbeigi, C. Pinna, S. Celotto, J.R. Yates, Local plastic strain evolution in a high strength dual-phase steel, Materials Science and Engineering A, 527 (2010) 5026-5032.

[17] J. Kang, Y. Ososkov, J.D. Embury, D.S. Wilkinson, Digital image correlation studies for microscopic strain distribution and damage in dual phase steels, Scripta Materialia, (56) 2007 999-1002.

[18] J. Kadkhodapour, A. Butz, S. Ziaei Rad, Mechanisms of void formation during tensile testing in a commercial, dual-phase steel, Acta Materialia, 59 (2011) 2575–2588.

[19] X.L. Cai, J. Feng, W.S. Owen, The dependence of some tensile and fatigue properties of a dual-phase steel on its microstructure, Metallurgical Transactions A, 16 (1985) 1405–1415.

[20] M. Calcagnotto, D. Ponge, D. Raabe, Effect of grain refinement to 1 μm on strength and

toughness of dual-phase steels, Materials Science and Engineering A, 527 (2010) 7832-7840.

[21] C.C. Tasan, J.P.M. Hoefnagels, C.H.L.J. ten Horn, M.G.D. Geers, Experimental analysis of strain path dependent ductile damage mechanics and forming limits, Mechanics of Materials, 41 (2009) 1264-1276.

[22] D. Hull, Fractography, Cambridge university press, Cambridge, 1999.

[23] R. Wouters, L. Froyen, Scanning Electron microscope fractography in failure analysis of steels, Materials Characterization, 36 (1996) 357-364.

[24] S. Nambu, M. Michiuchi, Y. Ishimoto, K. Asakura, J. Inoue, T. Koseki, Transition in deformation behavior of martensitic steel during large deformation under uniaxial tensile loading, Scripta Materialia, 60 (2009) 221-224.

[25] M. Michiuchi, S. Nambu, Y. Ishimoto, J. Inoue, T. Koseki, Relationship between local deformation behavior and crystallographic features of as-quenched lath martensite during uniaxial tensile deformation, Acta Materialia, 57 (2009) 5283-5291.

[26] C. Du, J.P.M. Hoefnagels, R. Vaes, M.G.D. Geers, Plasticity of lath martensite by sliding of substructure boundaries, Scripta Materialia, 120 (2016) 37-40.

[27] C. Du, J.P.M. Hoefnagels, L.I.J.C. Bergers, M.G.D. Geers, Uni-axial nano-force tensile test of individual constituents from bulk material, submitted (2016).

[28] L.I.J.C. Bergers, J.P.M. Hoefnagels, M.G.D. Geers, On-wafer time-dependent high reproducibility nano-force tensile testing, Journal of Physics D: Applied Physics, 47 (2014) 495306.

[29] T. Maki, Microstructure and mechanical behaviour of ferrous martensite, Materials Science Forum, 56-58 (1990) 157-168.

[30] A.R. Entwisle, The kinetics of martensite formation in steel, Metallurgical Transaction, 2 (1971) 2395-2407.

[31] S.M.C. van Boheman, J. Sietsma, Effect of composition on kinetics of athermal martensite formation in plain carbon steels, Materials Science and Technology, 25 (2009), 1009-1012.

[32] S. Morito, K. Oh-Ishi, K, Hono, T. Ohba, Carbon enrichment in retained austenite films in low carbon lath martensite steel, ISIJ International, 51 (2011) 1200-1202.

[33] A.L.T. Azevedo, E.G. da Silva, Mossbauer study of retained austenite in a low C low alloy steel, Scripta Metallurgica, 12 (1978) 113-117.

[34] N. Kim, G. Thomas, Effects of morphology on the mechanical behavior of a dual phase Fe/2Si/0.1C steel, Metallurgical and Materials Transactions A: Physical Metallurgy and Materials Science, 12 (1981) 483-489.

[35] B.P.J. Sandvik, C.M. Wayman, Crystallography and substructure of lath martensite formed in carbon steels, Metallography 16 (1983) 199-227.

[36] F. Maresca, V.G. Kouznetsova, M.G.D. Geers, On the role of interlath retained austenite in the deformation of lath martensite, Modelling and Simulation in Materials Science and Engineering, 22(2014) 045011.

[37] K. Wakasa, C.M. Wayman, Crystallography and morphology of ferrous lath martensite, Metallography, 14 (1981) 49-60.

[38] C.C. Tasan, J.P.M. Hoefnagels, M.G.D. Geers, Microstructural banding effects clarified through micrographic digital image correlation, Scripta Materialia, 62 (2010), 835–838.

[39] J.P.M. Hoefnagels, C.C. Tasan, F. Maresca, F.J. Peters, V.G. Kouznetsova, Retardation of plastic instability via damage-enabled microstrain delocalization, Journal of Materials Science, 50 (2015) 6882-6897.

[40] X. Sun, A. Soulami, K.S. Choi, O. Guzman, W. Chen, Effects of sample geometry and loading rate on tensile ductility of TRIP800 steel, Materials Science and Engineering A, 541 (2012) 1-7.
[41] C. Wang, H. Ding, M. Cai, B. Rolfe, Characterization of microstructures and tensile properties of TRIP-aided steels with different matrix microstructure, Materials Science and Engineering A, 610 (2014) 65-75.

Chapter 9. Conclusions and recommendations

9.1 Conclusions

The objective of this thesis was to unravel the micro-plasticity of ferrite and martensite, the two most important phases in advanced high strength steels. To this end, an experimental approach to determine the average phase distribution around damage sites and a micro-tensile test for single grain/phase specimens from bulk materials have been developed. Micro-tensile tests on single crystal ferrite, single packet/block martensite, and on dual phase steel specimens were conducted to analyze their micro-scale mechanics. The conclusions are given bellow.

Average phase distribution around damage sites

Contrary to most research in the literature which focus on individual failure mechanisms of multiphase metals, a general, automated method was developed to obtain the statistics of the phase distribution around damages sites (Chapter 2). Simultaneously-acquired secondary electron images and over-exposed backscattered electron images have been acquired to that purpose. The latter accurately exposes the position and size of the voids, while the former provides the phase information. This method can be applied to obtain the statistics of many materials as long as sufficient contrast between the constituents exists in the images. The method was applied to two uni-axially tensile deformed dual phase steels with different amount of martensite bands. The results showed that for both materials, the voids are mostly surrounded by martensite in the direction of tension, whereby the probability to find ferrite in the cross-direction is lower for the strongly banded dual phase steel.

Micro-tensile testing of single grain/phase specimens

In Chapter 3, a micro-tensile test method was established to examine the micro-plasticity of single grains or single phases extracted from bulk materials. The method consists of the following steps. A deformation-free macro-sized wedge (surface area ~10×10mm^2) is prepared from bulk materials. After microstructural characterization of the wedge, focused ion beam milling is employed to fabricate, multiple parallel micro-tensile specimens (~9×3×2 μm^3) at freely selected locations on the wedge tip. The wedge concept solves the practical issues in micro-specimen handling and facilitates specimen alignment. The specimens are uni-axially loaded in a dedicated tensile tester that is equipped with precise alignment controls, high force and displacement resolution, and *in-situ* microscopic imaging capabilities. As a proof of principle, three typical materials were tested: a simple single phase material (interstitial free steel), a complex single phase material (fully martensitic steel), and a dual phase steel. It was demonstrated that this test method enables to gain deeper understanding of the micro-mechanics of bulk materials, which is otherwise difficult to obtain.

Micro-plasticity of ferrite

Ferrite is an important phase as it is present in many advanced high strength steels. However, its plasticity is complex due to its non-closed packed atomic structure. The literature is still not conclusive on the activation and the role of the different slip systems. Unlike closed-packed

phases such as austenite, slip systems with a low Schmid factor are observed to be active in ferrite. To this end, the above-developed micro-tensile test method was applied to study slip activity in single crystal ferrite (Chapter 4). It was found that specimens from the same grain show a reproducible slip system activity, with both the {110}<111> and {112}<111> families being equally activated, whereas no {123}<111> activity was observed. Moreover, cross-slip between the former slip systems and 'pencil-glide' have been observed. The critical resolved shear stress of these two active slip systems was found to be quite close, i.e. $\mathrm{CRSS}_{\{110\}} = (1.0 \pm 0.1) \times \mathrm{CRSS}_{\{112\}}$. The (primary) slip system(s) with the highest Schmid factor(s) always activate(s) first, whereas low (initial) Schmid factors were found for secondary slip systems that activate later. The origin for the low Schmid factor slip activity is induced by the increase of the Schmid factors of the secondary slip systems resulting from the interaction of primary slip system and applied boundary constraints. Therefore, non-Schmid effect was not the mechanism explaining the observations.

Micro-plasticity of lath martensite

Because of its high strength, lath martensite is the key strengthening phase in most advanced high strength steels. Therefore, the micro-tensile test method was applied to unravel the micro-plasticity of lath martensite in Chapter 6-8, after a detailed microscopic study of the crystallography and alloying elements distribution of lath martensite in dual phase steel in Chapter 5.

In the latter study, it was found that unlike the fully martensitic steels, the characterized lath martensite islands in dual phase steel contain laths of only one main packet with minor variants from a second packet of the same prior austenite. The size of the variants appeared to be related to the phase transformation sequence. The early-formed laths are larger with less dislocations, whereas the late-formed ones are smaller due to the induced space restrictions and have a higher dislocation density due to straining by prior phase transformation. It was confirmed by nano-indentation measurement that the larger variants are indeed softer while the smaller ones are harder. In addition, the boundary regions have higher hardness than the intra-lath regions and the hardening effect from high angle boundaries (block/packet boundaries) is more prominent than that from the low angle boundaries (lath/sub-block boundaries). The transformation sequence also has an influence on the partitioning of carbon atoms in lath martensite of the commercial dual phase steel which was subjected to a coating process at 450 °C for 300 s. 3D atom probe tomography results showed that the substitutional elements are homogenously distributed, whereas the carbon atoms partition to lath boundaries during the coating process in the early-formed variants. In the late-formed variants, the carbon atoms segregate in the vicinities of the dislocation cores to form so-called Cottrell atmospheres. The influence of the carbon redistribution during thermal treatment of the coating process, to which commercial dual phase is subjected, is more significant than the short auto-tempering during martensite phase transformation.

To study lath martensite plasticity, micro-tensile specimens were extracted from single packets and single blocks of heat-treated, large-grained fully martensitic steel, with internal

substructure boundaries either approximately parallel (Chapter 6) or titled (Chapter 7) to the loading direction. It was found that when the boundary is parallel to the loading direction, plasticity is carried by crystallographic slip, even it needs to cross substructure boundaries. Both block and sub-block boundaries strengthen the material by impeding the glide of dislocations. The strength of the single packet and single block specimens increases with, respectively, the number of block and sub-block boundaries, both following a Hall-Petch like relationship. All observed slip activity could be traced back to the {110}<111> system(s) with the highest Schmid factor(s). From tests on lath martensite with the substructure boundaries tilted at ~45° to the loading direction, a novel deformation mechanism, i.e. boundary sliding, was discovered. This mechanism competes with crystallographic slip to carry the overall deformation in lath martensite. All types of tested boundaries (block, sub-block, lath) were shown to exhibit sliding. With this well-tilted boundary configuration, the fractures of the specimens are always along the substructure boundaries, with a fracture stress that is much lower than for a specimen with boundaries parallel to the loading direction.

In Chapter 8, many micro-tensile specimens with boundaries of arbitrary orientation were tested. The specimens were categorized into two groups based on the dominant plasticity mechanisms: crystallographic slip versus boundary sliding. The conditions under which these two mechanisms are active depend on the difference between the highest Schmid factor of the slip systems on the substructure boundary planes and that of the slip systems which do not lie in the boundary planes. Micro-tensile specimens of dual phase steel which contain martensite islands were tested to verify if the sliding mechanism is also active in multiphase steels. Although it is easier to deform the ferrite grains and many specimens indeed fractured along an easy path in the ferrite, deformation through martensite islands was still observed, resulting in high local martensite plasticity. Analysis showed that the deformation path in the martensite islands follows a substructure boundary. Therefore, the sliding mechanism appears to be important in lath martensite in multiphase steels as well. This agrees with the literature and also explains papers that state that the local plasticity in lath martensite in multiphase steel can be higher than what is expected from a supposedly brittle material.

9.2 Recommendations

Although the advanced high strength steel grades used in the automobile industry so far have succeeded in making the vehicles lighter and safer, the increasingly stricter rules of CO_2 emission keep pushing the properties of the applied materials towards a 'greener' profile. Currently, the 3rd generation of advanced high strength steels are under development for mechanical properties such as further improved strength-ductility combination. A good understanding of the deformation mechanisms of the basic phases of advanced high strength steels is essential to realize this goal. To this end, recommendations for further research are given here, based on the insights gained in the study of the micro-plasticity of ferrite and lath martensite:

● The slip system activity in interstitial free steels was identified to be carried by both the {110}<111> and {112}<111> families, whereas in single block fully martensitic steels only

{110}<111> slip system activity was observed. The chemical difference between these two materials is mainly the carbon content (~0% vs. 0.092wt%). The difference of atomic structures between these two materials is almost absent. The latter is body centered tetragonal with low tetragonality due to the low carbon content and can be considered as body centered cubic in most cases. As both ferrite and martensite are important components of advanced high strength steels, it is important to understand the cause of the different crystallographic slip behavior of the two materials. Micro-tests on ferrite and martensite with a different carbon content and initial dislocation density can reveal under which conditions one or two slip families are active.

● The lath martensite specimens tested in this thesis were selected from large and ordered substructures. In Ref [1], it was shown that the substructures of lath martensite are more disordered when the carbon content is increased. In engineering materials, there is a considerable amount of less-organized lath martensite domains even with a low carbon content, where the substructures are entangled and the hierarchical structure is less obvious. It is logical to imagine that these areas are stronger than the well-defined and organized regions. However, the resulting strength and the deformation mechanisms of these disordered regions remain unknown. It would be highly relevant for industry to explore this type of less-ordered lath martensite.

● The sliding mechanism is found to mitigate the plasticity of lath martensite when the substructure boundaries are favorably oriented. The underlying reason was the possible presence of retained austenite films between the martensite laths. This is supported by numerical simulations [2]. To verify the hypothesis of inter-lath retained austenite experimentally, significant effort has been made to identify the presence of austenite films using transmission electron microscope, but without success so far. Instead of direct microscopic observation of the inter-lath retained austenite, it may be more straightforward to mechanically test a type of lath martensite that undoubtedly contains these austenite films. Quenching and partitioning steel is good candidate enabling an adequate measurement of the presence of inter-lath retained austenite [3,4].

● It is well known that austenite can transform into martensite under applied straining at above the Ms temperature [5]. It is therefore plausible to assume that the inter-lath austenite films transform at some point into martensite during the deformation, which reduces the portion of austenite films available for boundary sliding. Transmission electron microscopy of the above-mentioned quenching and partitioning steel, which contains thicker and thus more easily identifiable inter-lath retained austenite films, may be a route to investigate whether or not the 'TRIP' phenomenon occurs for inter-lath retained austenite films and to measure the threshold strain and the proportion of the transformed austenite in the films.

● In the final Chapter of the thesis, micro-tensile test of dual phase steel specimens has been applied to investigate whether or not the sliding mechanism is active in lath martensite of multiphase steels. However, because of the microstructure of the used dual phase steel, an easy localization path over the cross-section of the micro-specimens exists, thereby circumventing

deformation of the martensite islands to comply to the externally applied strain. As it is unfeasible to make the micro-specimens much larger, dual phase steel micro-specimens with a higher martensite volume fraction could be studied in which a localization path has to cross one or more martensite islands.

References

[1] S. Morito, H. Tanaka, R. Konishi, T. Furuhara, T. Maki, The morphology and crystallography of lath martensite in Fe-C alloys, Acta Materialia, 51 (2003) 1789-1799.

[2] F. Maresca, V.G. Kouznetsova, M.G.D. Geers, On the role of inter-lath retained austenite in the deformation of lath martensite, Modelling and Simulation in Materials Science and Engineering, 22 (2014) 040511.

[3] D.V. Edmonds, K. He, F.C. Rizzo, B.C. De Cooman, D.K. Matlock, J.G. Speer, Quenching and partitioning martensite—A novel steel heat treatment, Materials Science and Engineering A, 438-440 (2006) 25-34.

[4] E. De Moor, S. Larroix, A.J. Clarke, J. Penning, J.G. Speer, Effect of retained austenite stabilized via quench and partitioning on the strain hardening of martensitic steels, Metallurgical and Materials Transactions A, 39 (2008) 2589.

[5] G.B. Olson, Morris Cohen, A mechanism for the strain-induced nucleation of martensitic transformations, Journal of the Less Common Metals, 28 (1972) 107-118.

[6] P. C. Maxwell, A. Goldberg, J. C. Shyne, Stress-assisted and strain-induced martensites in Fe-Ni-C alloys, Metallurgical Transactions, 5 (1974) 1305-1318.

Curriculum Vitae

Chaowei Du was born on 10, July, 1986 in Sichuan, China. After finishing Bachelor's degree in Metallurgical Engineering in 2008 at University of Science and Technology Beijing, he continued his master study in the same direction at RWTH Aachen University in Germany. He conducted his master thesis on Atom Probe Characterization of Single Crystal Superalloys under the supervision Prof. Dierk Raabe and Dr. Pyuck-Pa Choi in MPIE Düsseldorf and obtained his Master's degree in 2011. In 2012, he started a PhD project in the group of Mechanics of Materials at Eindhoven University of Technology in the Netherlands under the supervision of Prof. Marc Geers and Dr. Johan Hoefnagels. The results of his PhD work are presented in this dissertation.

Samenvatting

Geavanceerd hoge sterkte staal en in het bijzonder twee-fase staal worden in toenemende mate toegepast in de automobiel industrie om aan de hoge eisen wat betreft CO_2 uitstoot en voertuig-veiligheid te voldoen. Geavanceerd hoge sterkte stalen bestaan overwegend uit meerdere fasen en hebben in het algemeen een complexe microstructuur. Een gedetailleerd begrip van de micromechanica is daarom essentieel om het mechanische gedrag van deze materialen te begrijpen. Het doel van dit proefschrift is het ontrafelen van de microscopische mechanismen van plasticiteit, voor de twee fasen die het belangrijkst zijn voor geavanceerd hoge sterkte staal, namelijk ferriet en lat-martensiet. Daarnaast is het doel om hun interactie in termen van de initiatie van schade te begrijpen.

Ten eerste is een geautomatiseerde techniek ontwikkeld die de gemiddelde fasedistributie rondom schade identificeert. Deze techniek gebruikt twee tegelijkertijd gemaakte microscopische opnames: (opzettelijk) overbelichte opnames van teruggestrooide elektronen, welke de schade locaties scherp markeren; en opnames van secundaire elektronen, welke worden gebruikt om de verschillende fasen te identificeren. Het is aangetoond dat deze techniek toepasbaar is op een brede selectie van meer-fasen materialen. Deze techniek maakt dus nieuwe inzichten in schade-evolutieprocessen mogelijk. Voor twee-fase staal is gevonden een configuratie die bestaat uit gebieden van hard martensiet in de richting van de opgelegde belasting en gebieden van ferriet in de tegengestelde richting het meest gevoelig is voor schade.

Ten tweede is een nieuwe methodologie ontwikkeld welke uiterst nauwkeurige trekproeven mogelijk maakt, waarbij geïsoleerde korrels of fasen met nano-Newton precisie kunnen worden gekarakteriseerd. De belangrijkste aspecten van deze methodologie zijn (i) de selectie van de locatie van de proefstukken, gebaseerd op gedetailleerde microstructurele en kristallografische karakterisatie, (ii) de fabricatie en gemakkelijke hantering van proefstukken van enkele micrometers groot, (iii) nauwkeurige uitlijning van de proefstukken en belasting onder goed gecontroleerde randvoorwaarden, en (iv) kracht- en verplaatsing-metingen met nano-Newton respectievelijk nanometer precisie, gecombineerd met in-situ microscopische analyse van slipsporen. Met voorbeelden is getoond hoe, met behulp van de rijke, complete microscopische en mechanische data, de micromechanica kan worden ontrafeld.

The micro-trekproef is vervolgens toegepast op een interstitieel vrij staal met grote korrels. Verschillende proefstukken gewonnen uit dezelfde korrel vertonen reproduceerbare kristallografische slip. De slip systemen in de {110}<111> en de {112}<111> familie laten gelijke activiteit zien, waarbij het slip systeem (of de slip systemen) met de hoogste Schmid factor altijd als eerste wordt geactiveerd. Daarentegen is er geen activiteit van het slip systemen in de {123}<111> slip familie gezien. Beide actieve slip systemen vertonen bij kamer temperatuur een vergelijkbare kritische geprojecteerde afschuifspanning (τc), namelijk $\tau_{c\{110\}}$ = (1.0±0.1) × $\tau_{c\{112\}}$. Alle andere slip sporen zijn geïdentificeerd als mechanismes die in de literatuur bekend staan als cross-slip en pencil-glide. Niet-Schmid effecten zijn niet nodig gebleken om de observaties te kunnen verklaren.

The kristallografie en de distributie van de legeringselementen van lat-martensiet in twee-fase staal zijn daarna bestudeerd. De latten in de martensiet eilanden in twee-fase staal volgen de Kurdjumov-Sachs (K-S) oriëntatie relatie met de originele austeniet fase nauwkeurig. De eilanden bestaan typisch uit één hoofd-pakket en een beperkt aantal secundaire varianten uit dezelfde originele austeniet korrel. Dit is anders dan in volledig martensitisch staal, dat normaal gesproken alle 24 K-S varianten bevatten. De martensietbanden rondom het midden (in de dikte richting) van de gewalste plaat bestaan uit continue domeinen. De meeste daarvan bestaan ook uit één hoofd-pakket met enkele secundaire varianten uit dezelfde originele austeniet korrel. De opvolgende fase-transformaties veroorzaken vroeg gevormde latten met een lage dislocatie dichtheid en laat gevormde kleine latten met een hoge dislocatie dichtheid. In commerciële twee-fase stalen ondergaat het lat-martensiet een koolstof scheiding met diffusie naar de dislocatiecentra tijdens het coating proces (op 450 graden Celsius gedurende 300 seconden). De distributie van substitutionele elementen blijft homogeen en het effect van zelf-tempering is gering.

De micro-plasticiteit van lat-martensiet is daarna bestudeerd door middel van uni-directionele trekproeven van micro-proefstukken uit volledig martensitisch staal met grove substructuur en rechte substructuurgrenzen. Daarbij zijn verschillende configuraties van deze grenzen beschouwd. Lat-martensiet vertoont daarin alleen kristallografische slip in de {110}<1-11> slip systemen welke gehoorzamen aan de wet van Schmid. Voor proefstukken met grenzen die bij benadering parallel aan de belastingsrichting liggen wordt de deformatie gedomineerd door kristallografische slip en is een verstevigingsmechanisme, dat erg lijkt op het bekende Hall-Patch mechanisme, gevonden voor zowel de subblok- als de blokgrenzen, waarbij de laatste een beetje effectiever zijn. Wanneer de substructuurgrenzen worden georiënteerd onder een hoek van ongeveer 45 graden ten opzichte van de belastingsrichting wordt er een ander mechanisme geactiveerd, welke de kristallografische slip in het lat-martensiet beperkt. Het is namelijk aangetoond dat de substructuurgrenzen zelf ook kunnen glijden, en dat dit mechanisme kan vóórkomen in elk type grensvlak (blok-, subblok- en latgrenzen). Het verschil tussen de maximale geprojecteerde afschuifspanning in de grensvlakken en op de kristallografische slipsystemen buiten deze grensvlakken bepaalt welk van deze twee mechanismen dominant is. Deze twee mechanismen zijn dus in competitie om de totale plasticiteit van het lat-martensiet te bewerkstelligen. Micro-trekproeven op twee-fase staal laten ook het glijden van grenzen zien. Dit verklaart de aanwezigheid van rapportages in de literatuur van grote plastische vervorming van martensiet. Daarom kan worden geconcludeerd dat het glijden van grenzen een belangrijk mechanisme van plasticiteit is in volledig martensitisch staal, twee-fase staal en in het algemeen in geavanceerd hoge sterkte staal.

Publication list

Journal publications

1. T.W.J. de Geus, C. Du, J.P.M. Hoefnagels, M.G.D. Geers, Systematic and objective identification of the microstructure around damage directly from images, Scripta Materialia, 113 (2016) 101-105.

2. C. Du, J.P.M. Hoefnagels, R. Vaes, M.G.D. Geers, Block and sub-block boundary strengthening in lath martensite, Scripta Materialia, 116 (2016) 117-121.

3. C. Du, J.P.M. Hoefnagels, R. Vaes, M.G.D. Geers, Plasticity of lath martensite by sliding of substructure boundaries, Scripta Materialia, 120 (2016) 37-40.

4. M. Bertin, C. Du, J.P.M. Hoefnagels, F. Hild, Crystal plasticity parameter identification with 3D measurements and Integrated Digital Image Correlation, Acta Materialia, 116 (2016) 321-331.

5. C. Du, J.P.M. Hoefnagels, L.I.J.C. Bergers, M.G.D. Geers, Uni-axial nano-force tensile test of individual constituents from bulk material, submitted (2016).

6. C. Du, J.P.M. Hoefnagels, S. Koelling, M.G.D. Geers, R. Petrov, V. Bliznuk, A. Behnam, J. Sietsma, P. Koenraad, Martensite crystallography and chemistry in dual phase and fully martensitic steel, submitted (2016).

7. C. Du, F. Maresca, J.P.M. Hoefnagels, M.G.D. Geers, Experimental characterization of micro-plasticity of ferrite by micro-tensile testing, in preparation.

8. C. Du, J.P.M. Hoefnagels, R. Petrov, M.G.D. Geers, Lath martensite plasticity enabled by sliding of sub-structure boundaries, submitted (2016).

Conference proceedings

1. J.P.M. Hoefnagels, C. Du, T.W.J. de Geus, R.H.J. Peerings, M.G.D. Geers, A statistical/ computational/ experimental approach to study the microstructural morphology of damage, Chapter 8 in Fracture, Failure and Damage Evolution, Volume 8: Proceedings of the 2014 Annual Conference on Experimental and Applied Mechanics, Eds: A. M. Beese et al., 61-65, 2015.

2. J.P.M. Hoefnagels, C. Du, M.G.D. Geers Boundary mechanics in lath martensite, studied by uni-axial micro-tensile tests, Chapter 4 in Micro and Nanomechanics, Volume 5: Proceedings of the Society for Experimental Mechanics Series, 21-25, 2016.

Acknowledgements

With this thesis, my PhD project is coming to an end. I have enjoyed it a lot, learned a lot and grown a lot, academically and personally. It is time to express my gratitude with some words.

I would like to thank my supervisors Prof. Marc Geers and Dr. Johan Hoefnagels for giving me this opportunity to pursue this project and for their constant support from the very beginning until the end. Marc, I still remember clearly what you said at the surprising birthday party of you to all the students: 'the happiest thing for me is to see your growth.' I also remember your effort to help me get a registration after I have told you that I wanted to take the TEM course in Antwerp for my interest. This is only one example of your support. In addition, I have learned a lot from you: being structured, efficient and critical...This has helped a lot to increase my productivity. Thank you, Marc.

Johan, you are always passionate, creative, patient and encouraging. Whenever I need advice and discussion, you are there. We had plenty of talks, about academics and others, which I really enjoyed a lot. It was lots of fun to have a conference trip with you too (Warsaw, Cambridge...). In the final stage of my thesis, we had a lot of writing together, during which I learned much about organizing the storyline of a paper and became a better writer. I will not forget that we've worked until midnight at your house for my deadline. I am very lucky to have had the best supervision ever and I am now an independent researcher. Thank you for all your help.

I would like to thank Marc van Maris. A huge amount of my time was spent in the multi-scale lab. Marc, master of the multi-scale lab, I met you more often than any other colleagues in the group. I enjoyed work with you very much. Thanks for your help whenever I need it and for your trust in me for supervising the lab when you were away.

Part of my experiments were conducted at other places than Eindhoven. Thanks goes to Prof. Roumen Petrov for the help and supervision. Roumen, I still remember the training of metallographic preparation, EBSD/TKD from you in the lab of Gent University. You also helped a lot with the TEM work. Thanks for all, Roumen. I would like to direct my acknowledgements to Prof. Jilt Sietsma for the discussions and the experiments in TU Delft. Jilt, your insight on quantification of analysis is really inspiring. Thank you.

I am grateful to Prof. Paul Koenraad, Prof. Roumen Perov, Dr. Christophe Pinna, Dr. Stefan Zaefferer and Dr. Carel ten Horn for taking their time and effort to read my thesis, and for their positive comments and suggestions to improve the thesis quality.

I also thank Tom de Geus and Francesco Maresca, who I shared most of my time with. Tom and Francesco, we had a lot of cooperation together and a lot of fun. I am lucky to have you two cum-laude guys in the same project, during which I have learned a lot, not only about academics. Tom, also thanks for the help of translating my summary into Dutch. Thanks for your help as well, Elleke.

I had plenty of meetings with other staff members too, Dr. Ron Peerlings and Dr. Varvara Kouznetsova, from whom I have also learned. Ron, you are encouraging. The talks with you are

always relaxing. Varvara, you are very organized and sharp on points. I thank you both.

The financial support from Materials innovation institute for this project is appreciated. Next to that, I would like to thank Dr. Carel ten Horn, Dr. Piet Kok, Dr. Jeroen van Beeck from Tata Steel for their inspiring discussions during the project meetings.

Other people, who have contributed to the experiments in this project are also appreciated. Behnam, Sebastian and Vitaliy, thanks. Morgan, thanks. It was great pleasure to work with you. Lucien, thanks for your help from the workshop too.

I would like to thank my students, who have contributed to this work directly or indirectly. Sophie, Tim, Uriel, Leo, René (special thanks), Lichao, thank you all.

Alice and Rachel have helped a lot with my questions on administrative matters. You two are always smiling and always give the right solutions. Thank you.

The help from Lambert is deeply appreciated. Lambert, thanks for the NTS and the related introductions. You helped me even when you were still very busy with your own work. Besides academics, I also enjoyed the discussions we had on other topics. Thank you.

These four years have been a very enjoyable journey which is beautiful to remember. This could not be true without my friends and colleagues. I had/have very nice office mates, who made/make my stay here much more pleasant and from whom I have also learnt. Benoit, Kun, Ye, Andre, Bart, Paul, Tom, Franz, Robin, Javier, thank you all. Benoit, thanks for the French cooking. Andre, I enjoy your ways of explaining complicated things in an easy and understandable way. I still remember your nice back-flip at the hotel in Cambridge. Franz, your attitude towards small details is really worth learning. My acknowledgements go to colleagues and friends, with whom I have spent joyful weekends in Eindhoven (although mostly I was in Aachen in weekends): Mary, Mirka, Danqing, Franceso, Jeroen, Jin, Salman, Maqsood and Kaipeng. Thanks for the nice time we've had together. Colleagues from the other offices, whose names are not listed here, thank you as well, for the talks and jokes we've had. It is my great honor to know you all and have shared this four-year journey with you.

I must thank my friends and their families in Aachen, with whom I have enjoyed plenty of happy weekends. Bo, Guixuan, Xiaohuan, Pengfei, thanks for the nice weekends and the help from you.

My thanks goes to Ying Lan and Bing Lan, for their constant help since we met. 谢谢你们。

Last but not least, I need to thank my father Zaiting Du and my mother Shunrong Zhang, who have not had high school education but have done their best to support mine. Mom and Dad, you are my source of warmth and encouragement. Without your support, I am not able to go this far. 爸妈，谢谢。My most sincere thanks goes to my beloved wife, Xi Luo, who has constantly supported me emotionally. Xi, my dear wife, my deepest thanks to you. Thank you for your company during my happy times, as well as the difficult times. We've walked along so far and like what we have done, we will walk together to our future.

Chaowei Du

Eindhoven, October 2016